

**The International Workshop on
Collectivity in Relativistic Heavy Ion Collisions
(IWoC 2014)**

PROCEEDINGS
of the Workshop held in Kolymbari, Crete, Greece,
September 14-20, 2014

Edited by:
L. Bravina, V.K. Magas, A. Feijoo

Barcelona, 2015

FOREWORD

IWoC 2014 took place on September 14-20, 2014 in Orthodox Academy of Crete (OAC), located in the exceptionally beautiful place nearby the Mediterranean Sea beach. The Workshop was devoted to Collective Dynamics in Relativistic Heavy Ion Collisions on occasion of 65th anniversary of Professor Laszlo Csernai (University of Bergen, Norway), who is working in the field for more than 40 years. It brought together 50 Laszlo's colleagues, many of whom were his former postdocs or students. Altogether, there were both theoreticians and experimentalists, prominent scientists and PhD students from Brazil, China, Czech Republic, France, Germany, Hungary, Italy, Netherlands, Norway, Poland, Romania, Russia, Serbia, Spain and USA.

Thirty-six talks, given during the Workshop, include seven overview talks of the CERN LHC experiments ALICE, ATLAS and CMS, and the RHIC BNL experiment STAR. Two talks presented the coming soon FAIR facility at GSI, and other talks were related to fascinating problems in low-energy Nuclear Physics, Physics of Relativistic Heavy Ion Collisions, Quantum Field Theory and Cosmology. The greatest advantages of the OAC as a conference cite is that the participants are the only guests of the Conference Center, thus providing the possibility to participants to continue fruitful discussions during the coffee-breaks, on the beaches and during the meals on the OAC terrace with amazing sea views.

A rich social program included two concerts of Classical Music, given by Moscow Trio: Ruben Muradian (piano), Svetlana Nohr (violin) and Vladimir Nohr (cello), conference excursions to famous Balos and Elafonissi beaches and conference dinner "Cretan Night" with folk dances and songs.

The conference was really successful, with extremely warm atmosphere, with music and songs on the opened terrace in the evenings, swimming with the moon under the stars. But the most important was that young PhD students and postdocs got possibility to discuss with famous professors the hottest topics in physics, as well as in other subjects. We hope they found many new ideas and topics to study.

The official Workshop website is <http://indico.cern.ch/event/284199/>.



 CONTENTS

- Author Index v

- J. Milosevic [CMS Collaboration],
*"Initial-state fluctuations and factorization breaking
 in Pb-Pb and p-Pb collisions at LHC energies"* 1

- A. Trzupek [ATLAS Collaboration],
*"Recent Results on Flow and Correlations
 in Heavy Ion Collisions from the ATLAS Experiment"* 10

- A. Mischke, *"Heavy-flavour results from the CERN-LHC"* 20

- L. Bravina and E. Zabrodin,
*"Directed Flow and Freeze-Out in Heavy-Ion Collisions
 in the Energy Range of Beam Energy Scan at RHIC"* 29

- G. Eyyubova, L.P. Csernai, V.K. Magas,
*"Identifying longitudinal rapidity fluctuations and
 directed flow measurements"* 41

- E. Zabrodin, L. Bravina, B.H. Buschbeck, Johansson,
 J. Crkovska, G. Eyyubova, V.L. Korotkikh, I.P. Lokhtin,
 L.V. Malinina, S.V. Petrushanko, A.M. Snigirev,
*"Higher Flow Harmonics and Cross-Talk of Elliptic
 and Triangular Flows"* 49

- B. Tomasik and M. Schulc,
"Anisotropic flow generated by hard partons in medium" 58

- L.P. Csernai, S. Velle and D.J. Wang,
*"Differential HBT and correlation functions for the
 exact hydro model"* 66

- D. J. Wang and L. P. Csernai,
"Flow Vorticity in Peripheral Heavy Ion Collisions" 75

-
-
- M. Bleicher, S. Endres, J. Steinheimer and H. van Hees,
"Recent results from the UrQMD hybrid model for heavy ion collisions" 83
 - T. Kodama and T. Koide, *"Variational Principle of Hydrodynamics and Quantization Process"* 90
 - R.D. de Souza, T. Kodama, T. Koide, J.H.G. Elsas, E.L. Bratkovskaya, W. Cassing,
"Evaluating the role of coarse graining in hydrodynamic modeling of heavy-ion collisions from microscopic dynamics" 101
 - V. Greco, F. Scardina, S.K. Das and S. Plumari,
"Heavy Quark Dynamics in QGP: Boltzmann vs Langevin" 111
 - C. Sasaki,
"Charmed Mesons near Chiral Symmetry Restoration" 119
 - D.-M. Zhou, Y.-L. Yan, X.-L. Li, X.-M. Li, B.-G. Dong, X. Cai and B.-H. Sa,
"PACIAE 2.2, extended to cover lepton-nuclear and lepton-nucleus deep-inelastic scattering" 124
 - B.-H. Sa, Y.-L. Yan, X.-L. Li, X.-M. Li, D.-M. Zhou, Y. Cheng, B.-G. Dong and X. Cai,
"The specific charged hadron multiplicity in $e^- + p$ and $e^- + D$ semi-inclusive deep-inelastic scattering" 136
 - M.E. Carrington, K. Deja and St. Mrowczynski,
"Collective modes in weakly anisotropic QGP" 149
 - A. Czajka and St. Mrowczynski,
"Universal Character of the Hard-Loop Action" 160
 - D.N. Poenaru and R.A. Gherghescu,
"Newest Developments in Cluster Radioactivity" 168
 - A. Mocsy, *"When the Worlds of Science and Art Collide"* 178
 - List of Participants 186

Author Index

- Bleicher, M. 83
- Bravina, L. 29, 49
- Bratkovskaya, E.L. 101
- Brusheim Johansson, B.H. 49
- Cai, X. 124, 136
- Carrington, M.E. 149
- Cassing, W. 101
- Crkovska, J. 49
- Csernai, L.P. 41, 66, 75
- Czajka, A. 160
- Das, S.K. 111
- Deja, K. 149
- Dong, B.-G. 124, 136
- Elsas, J.H.G. 101
- Endres, S. 83
- Eyyubova, G. 41, 49
- Gherghescu, R.A. 168
- Greco, V. 111
- van Hees, H. 83
- Kodama, T. 90, 101
- Koide, T. 90, 101

• Korotkikh, V.L.	49
• Li, X.-M.	124, 136
• Li, X.-L.	124, 136
• Lokhtin, I.P.	49
• Magas, V.	41
• Malinina, L.V.	49
• Milosevic, J. [CMS Collaboration]	1
• Mischke, A.	20
• Mocsy, A.	178
• Mrowczynski, St.	149, 160
• Petrushanko, S.V.	49
• Plumari, S.	111
• Poenaru, D.N.	168
• Sa, B.-H.	124, 136
• Sasaki, C.	119
• Scardina, F.	111
• Schulc, M.	58
• Snigirev, A.M.	49
• de Souza, R.D.	101
• Steinheimer, J.	83
• Tomasik, B.	58
• Trzupek, A. [ATLAS Collaboration]	10

- Velle, S. 66
- Wang, D.J. 66, 75
- Yan, Y.-L. 124, 136
- Zabrodin, E. 29, 49
- Zhou, D.-M. 124, 136

Initial-state fluctuations and factorization breaking in Pb-Pb and p-Pb collisions at LHC energies

Jovan Milošević¹ for the CMS Collaboration

¹ *University of Belgrade and Vinča Institute of Nuclear Sciences,
Belgrade, Serbia
e-mail: Jovan.Milosevic@cern.ch*

Abstract

The single-particle anisotropy coefficients measured in PbPb collisions at $\sqrt{s_{NN}}=2.76$ TeV and high-multiplicity pPb collisions at $\sqrt{s_{NN}}=5.02$ TeV by the CMS collaboration are presented. These coefficients are obtained from two-particle $\Delta\phi$ - $\Delta\eta$ correlations. The observed correlations in ultra-central PbPb events are expected to be particularly sensitive to initial-state fluctuations. The breakdown of factorization of two-particle correlations into single-particle azimuthal anisotropies is observed in both colliding systems. This effect, recently predicted by hydrodynamics, is induced due to initial-state fluctuations which could produce a transverse momentum dependence of event-plane angle even if hydrodynamic flow is the only source of correlations.

1. Introduction

Due to the difference in pressure gradient, the initial spatial anisotropy formed in relativistic heavy-ion collisions converts into a momentum anisotropy. Particles are then preferentially emitted in the plane with the biggest pressure gradient. Such a plane is the event plane (EP), characterized via a global azimuthal angle Ψ_n . The azimuthal angle particle

distribution can be Fourier decomposed as

$$\frac{dN}{d\phi} \propto 1 + 2 \sum_{n=1}^{\infty} v_n \cos[n(\phi - \Psi_n)] \quad (1)$$

where the elliptic flow (v_2) gives the biggest contribution in this expansion. The initial-state fluctuations makes the overlap region not perfectly lenticular, and thus higher orders Fourier coefficients appear. The triangular flow (v_3) appears to be a significant source of the overall signal, especially in the central collisions.

If particles are correlated with the EP, then they are also mutually correlated. This enables the use of the two-particle correlations to study collective phenomena in heavy-ion collisions. Two dimensional (2D) particle correlations in $\Delta\phi$ and $\Delta\eta$ could be formed. Here, $\Delta\phi$ and $\Delta\eta$ are differences in azimuthal angle ϕ and in pseudorapidity η between pairs of particles. In order to avoid short-range correlations arising from jet fragmentation, a wide $|\Delta\eta| > 2.0$ selection has been applied. A projection of the constructed 2D particle correlations onto the $\Delta\phi$ axis could also be characterized by a Fourier decomposition

$$\frac{dN}{d\Delta\phi} \propto 1 + 2 \sum_{n=1}^{\infty} V_{n\Delta} \cos(n\Delta\phi) \quad (2)$$

Fourier coefficients $V_{n\Delta}$ could be also obtained directly as

$$V_{n\Delta} = \langle\langle \cos(n\Delta\phi) \rangle\rangle_S - \langle\langle \cos(n\Delta\phi) \rangle\rangle_B \quad (3)$$

Here $\langle\langle \dots \rangle\rangle$ means averaging over many pairs and over many events of interest, while the indices S and B stand for *signal* and *background*. The background is calculated in the same way as the signal but particles which form a pair are taken from different events with similar multiplicities and vertex positions. The subtraction of the background takes into account the effects of detector non-uniformity.

Up to now, within the hydrodynamics, which could be used to explain seen phenomena, the usual assumption is that EP angle Ψ_n does not depend on p_T . This leads to factorization

$$\begin{aligned} V_{n\Delta}(p_{T1}, p_{T2}) &= \sqrt{V_{n\Delta}(p_{T1}, p_{T1})} \times \sqrt{V_{n\Delta}(p_{T2}, p_{T2})} \\ &= v_n(p_{T1}) \times v_n(p_{T1}) \end{aligned} \quad (4)$$

of the two-particle Fourier coefficients, $V_{n\Delta}$, from Eq.(2) in a product of single-particle Fourier coefficients from Eq.(1). Recently, it was shown in [1] and [2] that due to the initial-state fluctuations, even if the only source of the correlations is hydrodynamic motion, the EP angle Ψ_n could depend on p_T . Thus, the Ψ_n is not any more a global plane and Eq.(4) becomes inequality

$$V_{n\Delta}(p_{T1}, p_{T2}) = \langle v_n(p_{T1})v_n(p_{T2}) \cos[n(\Psi_n(p_{T1}) - \Psi_n(p_{T2}))] \rangle \neq \sqrt{V_{n\Delta}(p_{T1}, p_{T1})} \times \sqrt{V_{n\Delta}(p_{T2}, p_{T2})} \quad (5)$$

and factorization is broken. A new observable is introduced:

$$r_n = \frac{V_{n\Delta}(p_{T1}, p_{T2})}{\sqrt{V_{n\Delta}(p_{T1}, p_{T1})} \sqrt{V_{n\Delta}(p_{T2}, p_{T2})}} = \frac{\langle v_n(p_{T1})v_n(p_{T2}) \cos[n(\Psi_n(p_{T1}) - \Psi_n(p_{T2}))] \rangle}{\sqrt{v_n^2(p_{T1})v_n^2(p_{T2})}} \quad (6)$$

In Eq.(6), single-particle anisotropy coefficients are mainly canceled. Then, the r_n is approximately equal to $\cos[n(\Psi_n(p_{T1}) - \Psi_n(p_{T2}))]$ and can measure the magnitude of the factorization breaking effect. The r_n achieves value smaller (equal) than one when factorization breaks (holds). The r_n value greater than one means existence of the non-flow effects.

2. Experiment

The CMS tracker works within 3.8 T magnetic field produced by a superconducting solenoid. This enables precise measurements of particle momenta. A detailed description of the CMS experiment can be found in [3]. To perform the analysis presented in this paper, data collected by CMS experiment at energies of $\sqrt{s_{NN}} = 2.76$ TeV and 5.02 TeV in PbPb and pPb with integrated luminosities of $160 \mu b^{-1}$ and $35 nb^{-1}$, respectively, have been used.

The data are obtained from the silicon tracker which measures charged particles with pseudorapidities from the range $|\eta| < 2.5$ and transverse momenta above 0.3 GeV/c. The detailed information on selections used

in this analysis can be found in [4] and [5]. The multiplicity classes are determined using track multiplicity, $N_{trk}^{offline}$, where only primary tracks with $|\eta| < 2.4$ and $p_T > 0.4$ GeV/c are counted. More details on multiplicity classification can be found in [6].

3. Results and discussion

The factorization breaking has been measured in PbPb collisions at $\sqrt{s_{NN}}=2.76$ TeV in [8]. The current analysis, with respect to the one presented in [8], is expanded to a much wider centrality range. Additionally, the study is performed for high multiplicity pPb collisions at $\sqrt{s_{NN}}=5.02$ TeV too. Using two hydrodynamic models [2, 7], a systematic comparison with the experimental data is also included. To quantify the effect of the factorization breaking, r_n is plotted as a function of the difference between transverse momenta of particles which form pairs of interest, $p_T^{trig} - p_T^{assoc}$, with $p_T^{trig} \geq p_T^{assoc}$. By construction, $r_n = 1$ when trigger and associated particle belongs to the same p_T interval.

Due to the limited space, the p_T -dependent results on the ratio r_2 and r_3 in PbPb collisions are not shown in this contribution and corresponding figures can be found in [5]. The magnitude of the r_2 increases with an increase of $p_T^{trig} - p_T^{assoc}$, with p_T^{trig} and going from peripheral to central collisions. The maximal effect of $\approx 20\%$ is achieved in ultra-central 0 – 0.2% collisions. For centralities below 5%, the magnitude of the effect is at the level of few percent. The measured values of the r_3 show that the factorization holds better then in the case of the r_2 , with a very weak centrality dependence.

The long-range azimuthal correlations, observed in high-multiplicity pPb collisions, are also analyzed in terms of the r_2 and the r_3 observables. The r_2 results, as a function of $p_T^{trig} - p_T^{assoc}$, are shown in Fig. 1. The analysis is performed for four multiplicity intervals, and four different trigger's p_T . The factorization breaking effect has the similar size in all four multiplicity intervals. As in the case of PbPb collisions, the size of the effect increases with an increase of $p_T^{trig} - p_T^{assoc}$ and with p_T^{trig} . Maximally, the size of the effect reaches only a few percent and it is much smaller than the one seen in ultra-central PbPb collisions, but it

is comparable with the r_2 values found in those PbPb collisions which have multiplicities similar to high-multiplicity pPb events.

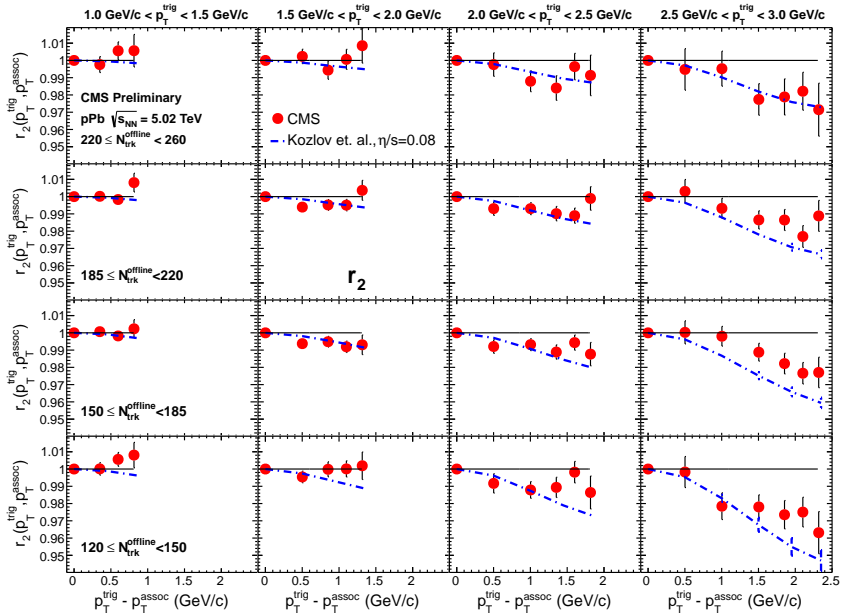


Fig. 1: The r_2 as a function $p_T^{trig} - p_T^{assoc}$ for different p_T^{trig} and $N_{trk}^{offline}$ values in 5.02 TeV pPb collisions. The hydrodynamic predictions for pPb collisions [7] are shown with blue dot-dashed lines. As the systematic uncertainties are negligible, the error bars correspond to statistical uncertainties only.

Fig. 2 shows the r_3 results. There is no significant factorization breaking in very high multiplicity pPb events ($185 < N_{trk}^{offline} < 260$). For pPb events with lower multiplicities, particularly for $120 < N_{trk}^{offline} < 150$, the r_3 value exceeds one. Hydrodynamic models with a p_T -dependent event plane angle fluctuations, according to Eq. 6, give the r_3 which is equal or less than one. Thus, this is a direct indication that there is a significant contributions of back-to-back jet correlations in the signal distributions used to extract the $V_{n\Delta}$ coefficients from these events.

Together with the experimental data, in Fig. 1 and 2 are shown predictions from Kozlov *et al.* hydrodynamic model [7]. This model semi-

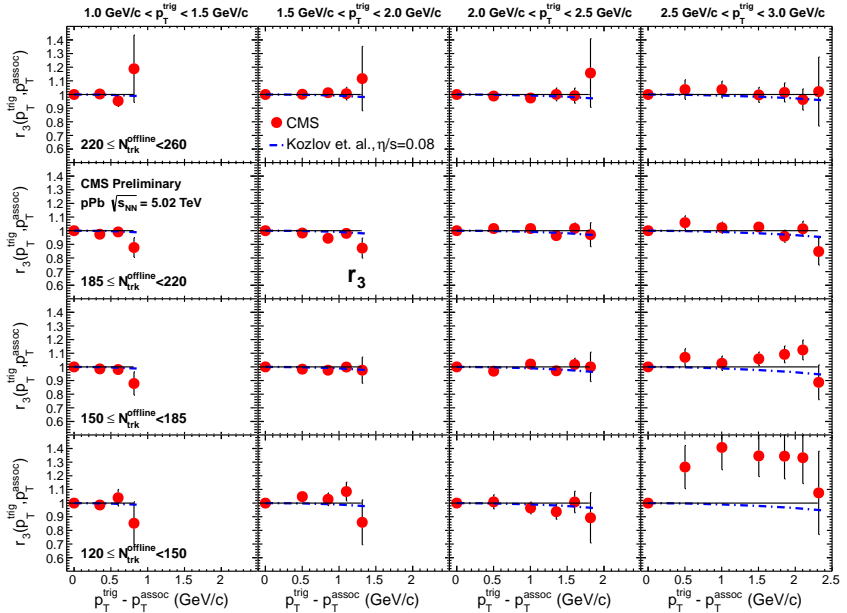


Fig. 2: The r_3 as a function of $p_T^{trig} - p_T^{assoc}$ for different p_T^{trig} and $N_{trk}^{offline}$ values in 5.02 TeV pPb collisions. The hydrodynamic predictions for pPb collisions [7] are shown with blue dot-dashed lines. As the systematic uncertainties are negligible, the error bars correspond to statistical uncertainties only.

quantitatively describes found results. In the model of Kozlov *et al.*, a modified MC-Glauber initial-state condition is used. The corresponding entropy density in the transverse plane has a 2D Gaussian shape whose width can vary and in such a way to simulate the transverse granularity of fluctuations. The experimentally found r_n ratios are found to be most sensitive just to that width. The r_2 data values are better described with a width parameter of 0.4 fm, while the width of 0.8 fm gives a r_n ratio practically equal to unity and thus underestimates the effect observed in the data. For both cases, the calculations are found to be nearly insensitive to different η/s values. This finding is consistent with the hydrodynamic calculations [2] used for more central PbPb collisions (see below). The results for the r_n in pPb collisions can provide new insight

into the hydrodynamic nature of long-range correlations and the role of initial-state fluctuations in such a small system.

In order to understand better the influence of the initial-state condition and η/s value on the factorization breaking effect and p_T -dependent event plane fluctuations in hydrodynamic models, a detailed comparison of r_2 ratios in 0 – 0.2% centrality PbPb collisions to hydrodynamic calculations is shown in Fig. 3. The results of the MC-Glauber [9, 10] and MC-KLN [11] initial conditions are compared, each of which is calculated with three different η/s values. For each initial state model, the r_2 ratios are found to be nearly insensitive to different values of η/s . This is due to the definition of the $r_n(p_T^a, p_T^b)$ ratio, where the magnitudes of anisotropy harmonics, which have a stronger sensitivity to η/s , are mostly canceled. Fluctuations of event plane angle in p_T are mainly driven by the lumpy fluctuations in the initial state. So, the r_n data can provide constraints on the detailed modeling of initial-state condition and its fluctuations of the medium created in heavy-ion collisions.

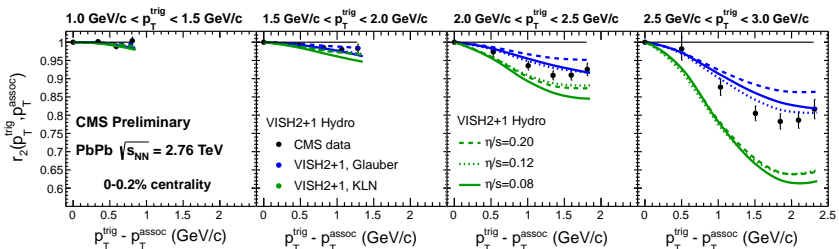


Fig. 3: The r_2 dependence of $p_T^{trig} - p_T^{assoc}$ in bins of p_T^{trig} for 0 – 0.2% PbPb collisions at $\sqrt{s_{NN}}=2.76$ TeV compared to viscous hydrodynamic calculations [2] using MC-Glauber and MC-KLN initial condition models, and three different values of η/s . As the systematic uncertainties are negligible, the error bars correspond to statistical uncertainties only.

In order to see how the factorization breaking effect depends on multiplicity in PbPb and pPb collisions, the r_2 and r_3 ratios are evaluated where the effect reaches its maximum ($2.5 < p_T^{trig} < 3.0$ GeV/c and

$0.3 < p_T^{assoc} < 0.5$ GeV/c) i.e. for $p_T^{trig} - p_T^{assoc} \approx 2$ GeV/c. The results are shown in Fig. 4. The centrality axis, applicable only for PbPb collisions, is also shown at the top of the figure. The size of the r_2 effect in PbPb events increases dramatically as the collisions become more central than 0 – 5%. Going from central to peripheral PbPb collisions, the size of the r_2 effect quickly decreases to only few percent. The effect in r_3 remains at 2 – 3% level and it is nearly independent of centrality. The hydrodynamic model predictions for PbPb collisions [2] with MC Glauber and MC-KLN initial conditions and $\eta/s = 0.12$ are also shown in dashed lines as a function of centrality. Neither of the two used initial-state conditions can describe the data quantitatively over the entire centrality range, although both of them reproduce the shape of the distribution. Kozlov *et al.* model overestimates the size of the effect. In the case of pPb collisions, the r_2 ratios show little multiplicity dependence and they are consistent with predictions of Kozlov *et al.* hydrodynamic model [7]. The r_3 ratios in pPb go significantly above 1 at lower multiplicities, due to the onset of non-flow correlations.

4. Summary

The CMS data have been used to study the factorization breaking effect as a function of transverse momentum and multiplicity in PbPb collisions at $\sqrt{s_{NN}}=2.76$ TeV and pPb collisions at $\sqrt{s_{NN}}=5.02$ TeV. The strongest effect of about 20% appears in the case of ultra-central PbPb collisions. In peripheral PbPb collisions, as well as in high-multiplicity pPb collisions, the effect has a moderate size and is on the level of few percent. The results are in a semi-quantitative agreement with hydrodynamic models which incorporate p_T -dependent event plane angle fluctuations induced by initial-state fluctuations. So, these results can be used to constrain the initial-state fluctuations.

1. F. G. Gardim, F. Grassi, M. Luzum and J. -Y. Ollitrault, Phys. Rev. **C87** 031901 (2013).
2. U. Heinz, Z. Qiu and C. Shen, Phys. Rev. **C87** 034913 (2013).
3. S. Chatrchyan *et al.* (CMS Collaboration), JINST **3** S08004 (2008).

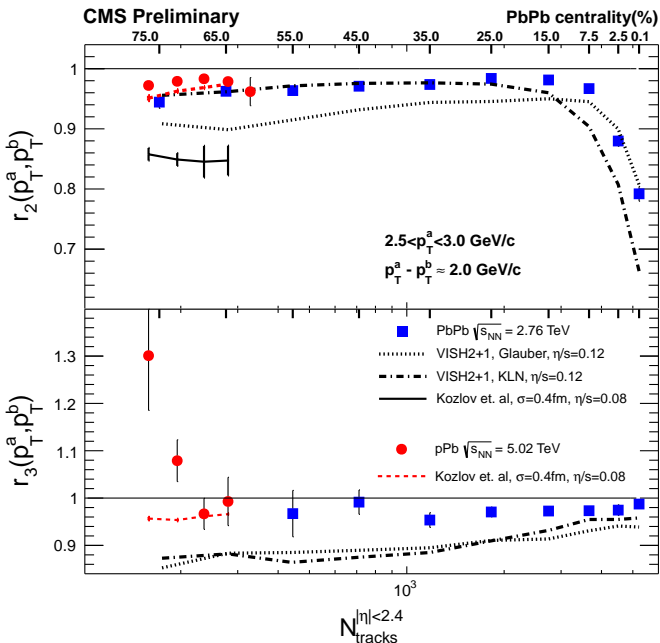


Fig. 4: The r_2 (top) and r_3 (bottom) multiplicity dependence in pPb and PbPb collisions. The lines show the calculations for PbPb collisions from viscous hydrodynamics in Ref. [2] with MC-Glauber and MC-KLN initial condition models and $\eta/s = 0.12$, and also hydrodynamics predictions for pPb collisions with $\eta/s = 0.08$ [7].

4. CMS Collaboration, CMS-PAS-HIN-14-006 (2014).
5. CMS Collaboration, CMS-PAS-HIN-14-012 (2014).
6. S. Chatrchyan *et al.* (CMS Collaboration), Phys. Lett. **B724** 213 (2013).
7. I. Kozlov, M. Luzum, G. Denicol, S. Jeon and C. Gale, arXiv:1405.3976 [nucl-th] (2014).
8. S. Chatrchyan *et al.* (CMS Collaboration), JHEP **1402** 088 (2014).
9. M. L. Miller, K. Reygers, M. Luzum, S. J. Sanders and P. Steinberg, Ann. Rev. Nucl. Part. Sci. **C57** 205 (2007).
10. B. Alver, M. Baker, C. Loizides, and P. Steinberg, arXiv:0805.4411 [nucl-ex] (2008).
11. H. -J. Drescher, A. Dumitru, A. Hayashigaki and Y. Nara, Phys. Rev. **C74** 044905 (2006).

Recent Results on Flow and Correlations in Heavy Ion Collisions from the ATLAS Experiment

Adam Trzupek¹ on behalf of the ATLAS Collaboration

21 December 2014

¹ *Institute of Nuclear Physics Polish Academy of Sciences,
ul. Radzikowskiego 152, 31-342 Kraków, Poland
e-mail: Adam.Trzupek@ifj.edu.pl*

Abstract

Measurements of soft particle production have provided valuable insight on properties of the Quark Gluon Plasma created in Pb+Pb collisions at the LHC. In particular, measurements of flow harmonics based on the azimuthal angle distributions of low- p_T particles probe the strongly coupled dense medium and test hydrodynamic model descriptions. Recently, the ATLAS experiment obtained results on flow harmonics and on the correlations between harmonics of different order using charged particles produced in p +Pb and Pb+Pb collisions. Results were obtained with the two-particle correlation method and the multi-particle cumulants, both well suited to probe the collective dynamics of the system. Comparison of measurements in p +Pb and Pb+Pb collisions suggests the presence of collective flow in small systems such as p +Pb collisions.

1. Introduction

One of the present-day approaches to probe properties of the Quark Gluon Plasma (QGP) is the study of Fourier harmonics of azimuthal angle distributions of particles produced in relativistic heavy ion collisions [1]. The Fourier harmonics quantify the large anisotropy observed

in particle distributions, which is attributed to the asymmetric shape of the initial interaction region of colliding nuclei. In particular, it is expected that the second Fourier harmonic (elliptic flow, v_2) is sensitive to the elliptical shape of the interaction region while higher order harmonics (v_3, v_4, \dots) are sensitive to the initial geometry fluctuations.

The measurements of flow harmonics performed by ATLAS and presented in this report, use data samples with integrated luminosity of $7 \mu\text{b}^{-1}$ for 2.76 TeV Pb+Pb and 28nb^{-1} for 5.02 TeV p +Pb collisions. The v_n harmonics are measured with charged particles tracks reconstructed in the ATLAS inner detector [2] (ID) using both the Pixel and SemiConductor Tracker. The ID tracks are reconstructed over the full azimuth and in a wide pseudorapidity range, $|\eta| < 2.5$. For the centrality determination in Pb+Pb collisions, the distribution of the total transverse energy measured in both arms of the forward calorimeter (FCal) is used. The two FCal arms are located along the beam axis, symmetrically relative to the interaction point [3]. The detector covers pseudorapidity range of $3.1 < |\eta| < 4.9$, and has a full acceptance in the azimuth. For p +Pb collisions the centrality (also called the event activity) is determined using the distribution of the total transverse energy, E_{T}^{Pb} , measured in one FCal arm, located at the Pb-going side [4]. Additionally, for p +Pb collisions the number of reconstructed ID tracks, $N_{\text{ch}}^{\text{rec}}$, is used as an alternative measure of the event activity.

2. Multi-particle cumulant method for Pb+Pb collisions

The ATLAS results on v_n measurements obtained using multi-particle correlations are from Ref. [5]. The method exploits a direct relation between azimuthal angle correlations of $2k$ particles and the $2k$ -th moments of v_n distributions, which is valid when the non-flow correlations (e.g. from resonance decays, or jets) are small. Moreover, it was observed [6] that using higher order cumulants of the multi-particle correlations suppresses the contributions of non-flow effects which are typically of lower order. In the analysis, cumulants were obtained with the Generating Function Cumulant method [6]. Figure 1 shows the elliptic flow, $v_2\{2k\}$, from the two-, four-, six-, and eight-particle cumulants and from the event plane method, $v_2\{\text{EP}\}$, calculated as a function of transverse mo-

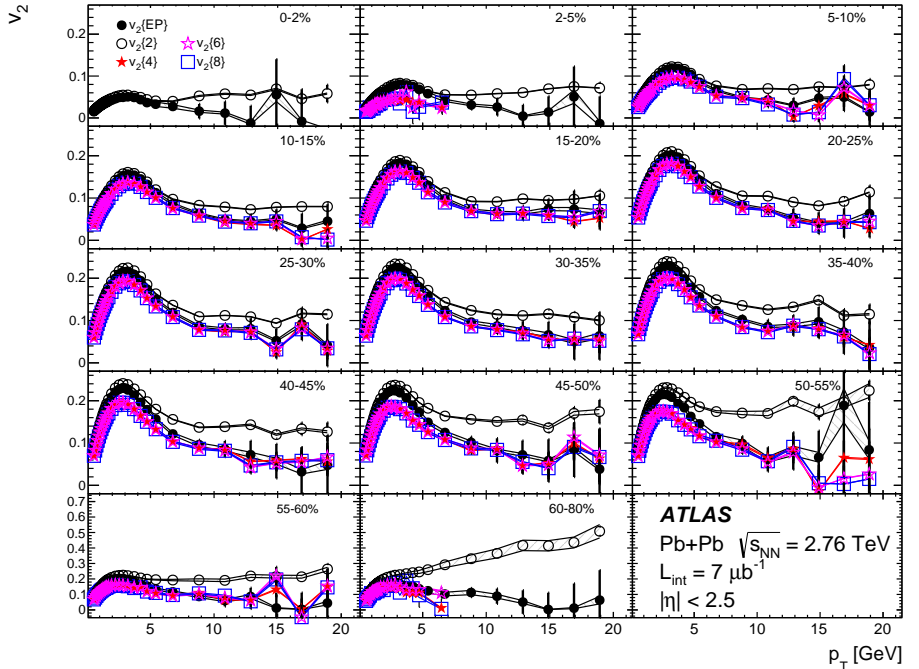


Fig. 1: The p_T -dependence of v_2 calculated with the two-, four-, six-, and eight-particle cumulants and with the event-plane method in different centrality bins [5].

mentum over pseudorapidity range of $|\eta| < 2.5$ in 14 centrality intervals. The event-plane $v_2\{\text{EP}\}$ is systematically smaller than $v_2\{2\}$ since it is less affected by short-range two-particle non-flow correlations. On the other hand, $v_2\{\text{EP}\}$ is larger than $v_2\{4\}$ mainly due to flow fluctuations. The remaining harmonics $v_2\{2k\}$ with $k > 1$ are similar within the uncertainties, for all centrality intervals, indicating that already in the four-particle cumulants, non-flow correlations are significantly suppressed. As a function of transverse momentum, the elliptic flow first increases with p_T up to $p_T \approx 2-3$ GeV, then decreases for p_T values up to about 6 GeV. Beyond p_T of about 10 GeV, a much weaker p_T -dependence is observed which may reflect the variations of the parton energy loss in the dense, strongly interacting medium due to the anisotropy of the initial geometry.

The transverse momentum dependence of v_3 and v_4 from cumulants

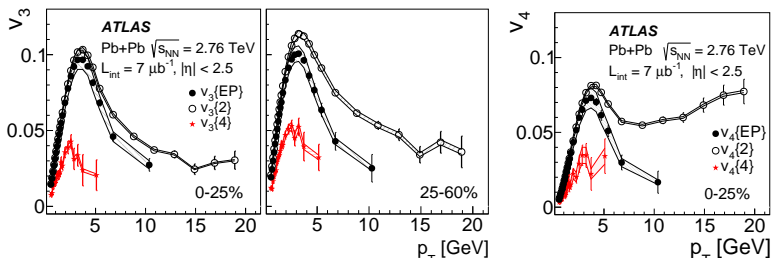


Fig. 2: The p_T -dependence of v_3 calculated with two- and four-particle cumulants and with the event-plane method for the centrality bin 0–25% (left plot) and 25–60% (middle plot). The right plot shows results for v_4 for the centrality bin 0–25% [5].

and the event plane method is shown in Fig. 2 in the broad centrality intervals as indicated in the plots. Similarly to v_2 , contributions from non-flow short-range correlations are smaller in $v_{3,4}\{EP\}$ than in $v_{3,4}\{2\}$. Non-zero values of the third and fourth flow harmonics calculated with four-particle cumulants are observed and their p_T -dependence is similar to the p_T -dependence of v_2 . The $v_{3,4}\{4\}$ harmonics are by a factor of 2 smaller than $v_{3,4}\{2\}$. The small values of $v_{3,4}\{4\}$ are consistent with the suppression of non-flow effects for higher order cumulants and strong event by event fluctuations of v_3 and v_4 harmonics.

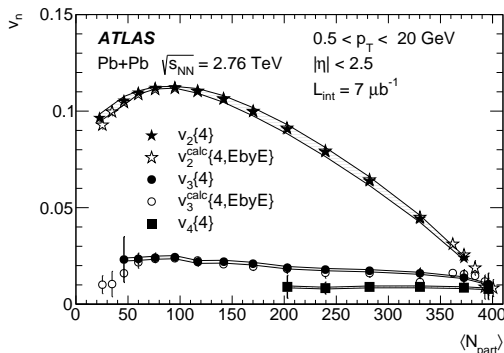


Fig. 3: The $v_2\{4\}$, $v_3\{4\}$ and $v_4\{4\}$ harmonics as a function of $\langle N_{part} \rangle$. Filled symbols show the results from the cumulant method [5] while open symbols show $v_{2,3}^{calc}\{4, EbyE\}$ calculated from the $p(v_2)$ and $p(v_3)$ distributions [7].

The differential flow harmonics were used to obtain harmonics integrated over the full measured range in η and p_T . Figure 3 shows the integrated $v_{2,3,4}\{4\}$ as a function of the collision centrality, characterized by the average number of participating nucleons, $\langle N_{part} \rangle$. One can observe a strong centrality dependence of the elliptic flow with a maximum at $\langle N_{part} \rangle \approx 100$, while $v_3\{4\}$ and $v_4\{4\}$ are much smaller than

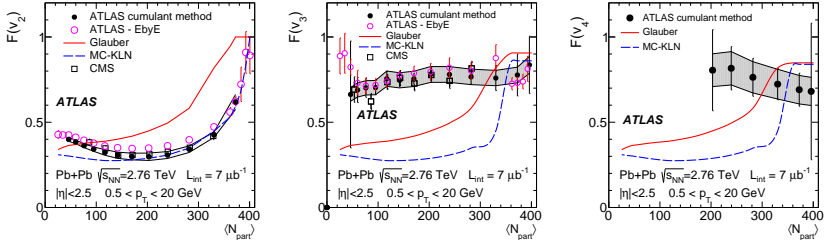


Fig. 4: The relative fluctuations, $F(v_n)$ for $n = 2, 3, 4$ as a function of $\langle N_{\text{part}} \rangle$, from the cumulant method [5] (filled circles) and from the measured EbyE $v_{2,3}$ distributions [7] (open circles). The left and middle plots also show $F(v_{2,3})$ as measured by CMS [8] (open squares). F obtained from the eccentricity distributions of the Glauber [9] and MC-KLN [10] models are shown by curves.

$v_{2,3}^{\text{calc}}\{4, \text{EbyE}\}$ harmonics calculated from the moments of event-by-event (EbyE) flow harmonics distributions, $p(v_n)$ [7]. A good agreement between the two independent measurements is observed.

The cumulant method also allows to measure flow harmonics fluctuations using the formula $F(v_n) = \sqrt{(v_n\{2\}^2 - v_n\{4\}^2) / (v_n\{2\}^2 + v_n\{4\}^2)}$, which provides a good estimate of the ratio of the standard deviation, σ_{v_n} , to the mean, $\langle v_n \rangle$ of the $p(v_n)$ distribution. When non-flow correlations are small and $\sigma_{v_n} \ll \langle v_n \rangle$ one can expect $F \approx \sigma_{v_n} / \langle v_n \rangle$. The non-flow correlations have the largest effect on $v_n\{2\}$. Therefore, replacing in F , $v_n\{2\}$ by $v_n\{\text{EP}\}$ reduces their impact on the estimate of the flow harmonics fluctuations. Figure 4 shows centrality dependence of F for v_2 , v_3 and v_4 . Large fluctuations are observed for v_2 in the central Pb+Pb collisions and for v_3 and v_4 in the full accessible centrality range. For the elliptic flow, strong centrality dependence of F is observed with smallest fluctuations in mid-central collisions. A good agreement between ATLAS and CMS results is observed for v_2 and v_3 fluctuations as well as between fluctuations measured with cumulants and with the EbyE method. The eccentricity fluctuations obtained from Glauber [9] and MC KLN [10] models do not reproduce the data, as shown in Fig. 4. Figure 5 shows p_T -dependence of v_2 fluctuations for Pb+Pb collisions in different centrality intervals. One can see that $F(v_2)$ weakly depends on p_T , except for the 2–5% centrality bin where a significant increase of F with increasing p_T is observed.

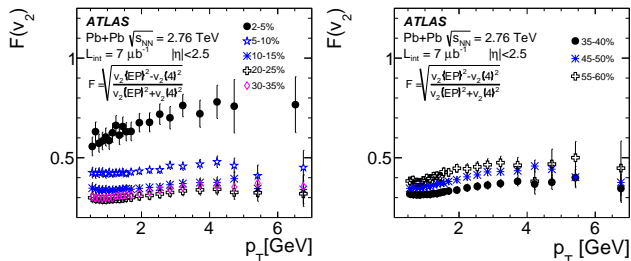


Fig. 5: The p_T -dependence of elliptic flow fluctuations, $F(v_2)$, for central (left panel) and peripheral collisions (right panel) [5].

3. Event shape studies in Pb+Pb collisions

To study flow harmonics correlations in more details the Pb+Pb data sample was sub-divided into different “ellipticity” classes [11]. To this end, for each Pb+Pb event an elliptic flow vector \mathbf{q}_2 is defined using the FCal tower transverse energies, E_T^i , (each tower i covers $\Delta\eta \times \Delta\phi = 0.1 \times 0.1$): $\mathbf{q}_2 = (\sum E_T^i \cos \phi_i, \sum E_T^i \sin \phi_i) / \sum E_T^i - \langle \mathbf{q}_2 \rangle_{ev}$, where ϕ_i is the tower azimuthal angle and $\langle \mathbf{q}_2 \rangle_{ev}$ removes biases due to detector effects. For a given centrality class (“event size”), the distribution of the module of the flow vector is used to divide the event sample into classes of different ellipticity (or “event shape”). The study of correlations between harmonics of different orders or correlations of v_2 measured in two different p_T ranges as a function of the event shape, as quantified by q_2 , provides insight into fluctuations in the initial collision geometry, as well as into non-linear dynamics in the collective expansion.

Centrality dependence of the correlation between $v_2(0.5 < p_T < 2 \text{ GeV})$ and $v_2(3 < p_T < 4 \text{ GeV})$ is shown by the “boomerang” gray band in Fig. 6 (left panel). The boomerang-like dependence is characteristic for the viscous dumping effects expected in the QGP. Figure 6 (left panel) also shows the same correlation, but in different q_2 bins. For each centrality interval, an approximately linear correlation is observed between v_2 measured in low- and high- p_T ranges when q_2 is varied. The linear correlations indicate that the viscous effects change very little with the variation of the event shape, suggesting that viscous effects are controlled rather by the system size than by the system shape. The $v_2 - v_3$ correlations in the same p_T -range of 0.5–2 GeV are shown in Fig. 6 (middle panel). Without q_2 selection, a clear boomerang-like dependence

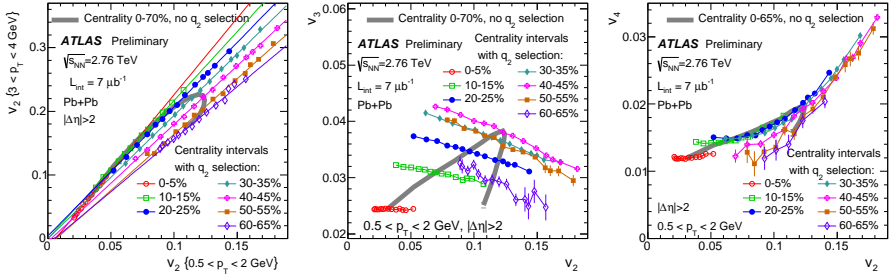


Fig. 6: Left plot: The correlation of v_2 calculated in 0.5–2 GeV and in 3–4 GeV p_T -ranges in various centrality intervals but without q_2 selection (gray band). The data points show q_2 -dependence of the correlation in each of the quoted centrality intervals. Middle and right plots represent the correlations $v_2 - v_3$ and $v_2 - v_4$ measured in 0.5–2 GeV p_T -ranges [11].

(gray band) is also visible for this correlation as a function of centrality. However, for each centrality bin, an anti-correlation between v_2 and v_3 is observed in various q_2 intervals. Such dependence is expected from e.g. the multi-phase transport model predicting anti-correlations of eccentricities $\epsilon_2 - \epsilon_3$ and harmonics $v_2 - v_3$ [11]. The right panel of Fig. 6 shows corresponding $v_2 - v_4$ correlations measured in the p_T -range of 0.5–2 GeV. The gray band shows the boomerang-like correlations without q_2 selection while solid points connected by lines represent q_2 -dependence for a given centrality bin. A clear non-linear q_2 -dependence of $v_2 - v_4$ correlations for a given centrality bin is observed, which was found to disagree with $\epsilon_2 - \epsilon_4$ correlations predicted by models of the collision geometry [11].

4. Collective flow in p +Pb collisions

Collective flow in p +Pb collisions was studied in ATLAS using the multi-particle cumulants for low statistics 2012 data [12] and with the two-particle correlation (2PC) method applied to the full, high-statistics 2013 dataset [4]. In the 2PC method the “per-trigger yield” (PTY) is calculated, which measures the average number of particles correlated with each trigger particle. For collisions of higher multiplicity, PTY is corrected for the non-flow effects estimated from PTY in low-activity events selected by requiring the total number of reconstructed tracks $N_{\text{ch}}^{\text{rec}} < 20$

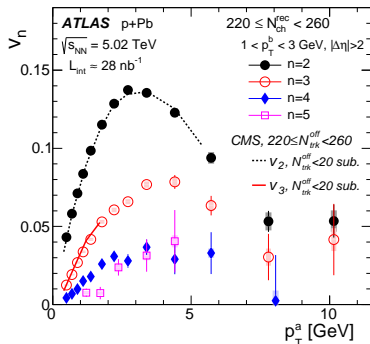


Fig. 7: The $v_n(p_T^a)$ for $n = 2, \dots, 5$ in $220 \leq N_{ch}^{rec} < 260$ event-activity class obtained for $|\Delta\eta| > 2$ and the reference p_T^b range of 1–3 GeV. ATLAS results [4] are compared to the CMS data [13] obtained by subtracting the peripheral events (the number of offline tracks $N_{trk}^{off} < 20$), shown by the solid and dashed lines.

or the transverse energy $E_T^{Pb} < 10$ GeV. Assuming factorization of the corrected PTY into product of flow harmonics, $v_n \times v_n$, the flow harmonics v_2, \dots, v_5 were calculated as a function of transverse momentum in different bins of the event activity. Figure 7 shows the p_T -dependence of v_2, \dots, v_5 in $p+Pb$ collisions of high multiplicity $220 \leq N_{ch}^{rec} < 260$. All flow harmonics follow similar trends, i.e. they increase with p_T up to 3–5 GeV and then decrease, but remain positive at higher p_T . It can be also seen that ATLAS and CMS elliptic and triangular flow harmonics are in a good agreement. In Figure 8 the p_T -dependence of v_2, v_3 and v_4 is compared between $p+Pb$ collisions of $220 \leq N_{ch}^{rec} < 260$ and $Pb+Pb$ collisions of similar N_{ch}^{rec} corresponding to the 55–60% centrality bin. One can see that v_2, v_3 and v_4 are higher in $Pb+Pb$ than in $p+Pb$ collisions. In order to take into account the differences in the mean p_T for $p+Pb$ and $Pb+Pb$ collisions at different energies, the p_T values of $Pb+Pb$ data points were rescaled by a factor 1.25 [4]. Additionally, to compare the shape of the resulting p_T -dependence of flow harmonics, the $Pb+Pb$ v_2 and v_4 were scaled down to match $p+Pb$ values. A good agreement between the shapes of $v_n(p_T)$ in $p+Pb$ and $Pb+Pb$ collisions is observed after rescaling.

5. Summary

The ATLAS experiment presented results on v_2, v_3 and v_4 obtained from multi-particle cumulants in a wide range of transverse momentum 0.5–20 GeV and pseudorapidity $|\eta| < 2.5$ for $Pb+Pb$ collisions at $\sqrt{s_{NN}} = 2.76$ TeV. The results provide a valuable insight into the fluctuations in the geometry of the initial interaction region as well as into non-flow

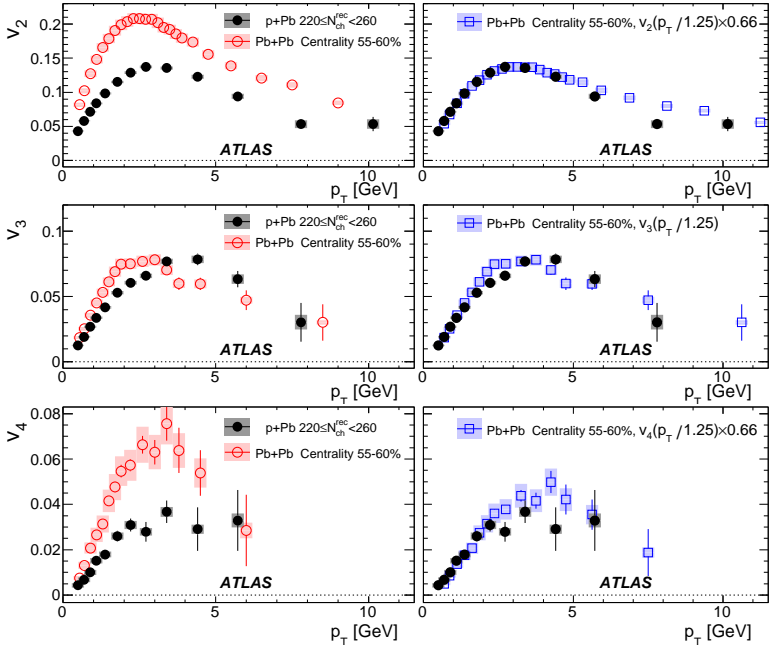


Fig. 8: The p_T -dependence of v_2 , v_3 and v_4 compared between p +Pb collisions of $220 \leq N_{ch}^{rec} < 260$ and Pb+Pb collisions in 55–60% centrality bin. In the right column, the Pb+Pb data are rescaled horizontally by a factor of 1.25, and v_2 and v_4 are also down-scaled by an empirical factor of 0.66 to match the p +Pb data [4].

effects distorting flow harmonics measurements. For Pb+Pb collisions, ATLAS also obtained correlations of v_2 (at low- p_T) vs. v_2 (at high- p_T) and v_2 - v_n for $n = 3, 4, 5$ in different centrality and q_2 bins using the 2PC method. Particularly interesting are the v_2 - v_2 correlations which suggest that viscous effects in QGP are controlled rather by the system size than by the system shape. The 2PC method was also recently used to study the collective flow phenomena in high statistics 5.02 TeV p +Pb collisions. The results on p_T -dependence of v_n for $n = 2, 3, 4$ suggest that the collective flow in p +Pb collisions is similar to that observed in the Pb+Pb system.

This work was supported in part by the National Science Center grants DEC - 2011/03/B/ST/02631 and DEC-2013/08/M/ST2/00320, and by PL-Grid Infrastructure.

References

1. S. A. Voloshin, A. M. Poskanzer, and R. Snellings, *Elementary Particles, Nuclei and Atoms* (Springer-Verlag) **23** (2010) 293, [arXiv:0809.2949 \[nucl-ex\]](#).
2. ATLAS Collaboration, *JINST* **3** (2008) S08003.
3. ATLAS Collaboration, *Phys. Lett. B* **707** (2012) 330, [arXiv:1108.6018 \[hep-ex\]](#).
4. ATLAS Collaboration, *Phys. Rev. C* **90** (2014) 044906, [arXiv:1409.1792 \[nucl-ex\]](#).
5. ATLAS Collaboration, [arXiv:1408.4342 \[hep-ex\]](#).
6. N. Borghini, P. M. Dinh, and J. Y. Ollitrault, *Phys. Rev. C* **63** (2001) 054906, [arXiv:nucl-th/0007063](#).
7. ATLAS Collaboration, *JHEP* **11** (2013) 183, [arXiv:1305.2942 \[hep-ex\]](#).
8. CMS Collaboration, *Phys. Rev. C* **89** (2014) 044906, [arXiv:1310.8651 \[nucl-ex\]](#).
9. M. L. Miller, K. Reygers, S. J. Sanders, and P. Steinberg, *Ann. Rev. Nucl. Part. Sci.* **57** (2007) 205, [arXiv:nucl-ex/0701025](#).
10. A. Adil, H. J. Drescher, A. Dumitru, A. Hayashigaki, and Y. Nara, *Phys. Rev. C* **74** (2006) 044905, [arXiv:nucl-th/0605012](#).
11. ATLAS Collaboration, ATLAS-CONF-2014-022 (2014). <http://cds.cern.ch/record/1702980>.
12. ATLAS Collaboration, *Phys. Lett. B* **725** (2013) 60, [arXiv:1303.2084 \[hep-ex\]](#).
13. CMS Collaboration, *Phys. Lett. B* **724** (2013) 213, [arXiv:1305.0609 \[nucl-ex\]](#).



Heavy-flavour results from the CERN-LHC

André Mischke ¹

¹ *Institute for Subatomic Physics, Department of Physics and Astronomy and EMMEφ, Faculty of Science, Utrecht University, Princetonplein 5, 3584 CS Utrecht, the Netherlands*
E-mail: a.mischke@uu.nl

Abstract

Heavy quarks (charm and beauty) are sensitive and penetrating probes to study the dynamical properties of the Quark-Gluon Plasma (QGP). This state of matter can be recreated, at sufficiently high temperatures or energy densities, and carefully studied in high-energy heavy-ion collisions. Due to their large mass, heavy quarks are produced predominantly in the (hottest) initial phase of the collision via gluon fusion processes and therefore allow to explore the complete space-time evolution of the QGP matter. Theoretical models based on perturbative QCD predict that heavy quarks should experience smaller energy loss than light quarks, when propagating through the QGP matter, due to the mass-dependent suppression of gluon radiation at small angles (the so-called dead-cone effect). Of particular interest is the quantitative understanding of fundamental quantities such as the transport coefficients.

In this talk, selected highlights on open heavy-flavour production in lead-lead collisions at CERN's Large Hadron Collider will be presented and discussed.

1. Heavy-quark production and parton-medium interaction

A hot and dense medium, consisting of deconfined quarks and gluons, is called the Quark-Gluon Plasma (QGP). The QGP can be created and carefully studied in particle accelerators at ultra-relativistic collision

energies. The so-called hot nuclear matter effects can be investigated by comparing heavy-flavour production in Pb–Pb collisions with pp and p–Pb reactions. Proton–proton collisions are used as a reference, while p–Pb collisions provide a way to detect cold nuclear matter effects.

Heavy quarks (charm and beauty) are good probes to investigate the QGP properties and its evolution, since they are predominantly produced in hard scattering processes (flavour creation and gluon splitting) during the early stage of the collision and are expected to be sensitive to its energy density, through the mechanism of parton energy loss. The QCD energy loss is expected to occur via both inelastic (medium-induced gluon radiation or radiative energy loss) [1–4] and elastic (collisional energy loss) [5,6] processes. Quarks have a smaller colour coupling factor with respect to gluons and the "dead-cone effect" [7–10] should reduce small-angle gluon radiation for heavy quarks with moderate energy-over-mass values so that the energy loss for quarks is expected to be smaller than for gluons. Other mechanisms, such as in-medium hadron formation and dissociation [11,12], play also a role for the production of heavy-flavour hadrons.

The energy loss and transport or drag coefficient of the QGP can be quantified via the nuclear modification factor R_{AA} , which is the ratio of the yield measured in Pb–Pb to that observed in pp scaled with the number of binary nucleon-nucleon collisions.

In nuclear collisions, anisotropic patterns originate from the initial anisotropy in the spatial distribution of the nucleons participating in the collision. The anisotropy is described by the coefficient $v_n = \langle \cos[n(\phi - \Psi_n)] \rangle$ of the Fourier expansion describing the azimuthal angle ϕ of particles with respect to the initial state symmetry plane for the considered harmonic Ψ_n . For non-central collisions, the overlap region of the colliding nuclei has an almond-like shape and the anisotropy is dominated by the second coefficient v_2 or elliptic flow. At low p_T , charmed hadron v_2 provides a unique opportunity to test whether also quarks with large mass ($m_c = 1.3 \text{ GeV}/c^2$) participate in the collective expansion dynamics and possibly thermalise in the medium [13]. At low and intermediate p_T , the elliptic flow of heavy-flavour particles is expected to be sensitive to the heavy-quark hadronisation mechanism (e.g., recombination). At

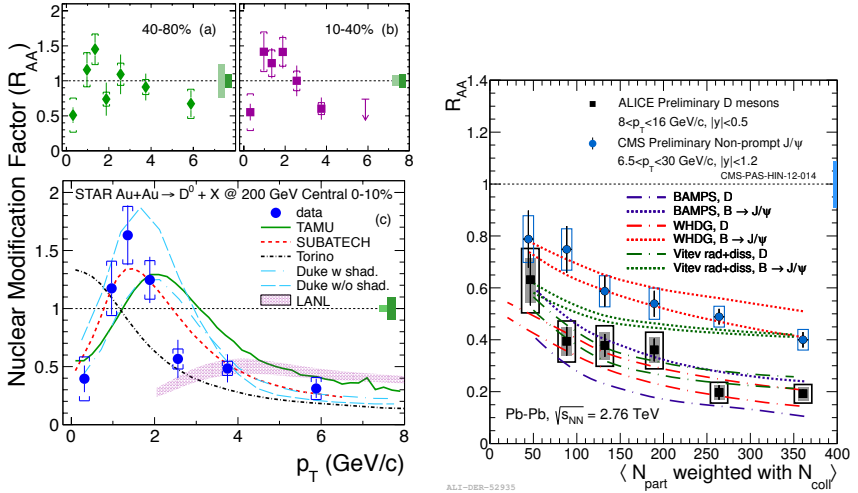


Fig. 1: Left panel: Transverse momentum dependence of the average R_{AA} of D^0 mesons in Au+Au collisions at $\sqrt{s_{NN}} = 200$ GeV [14]. The data are compared to different energy loss model calculations. Right panel: R_{AA} of prompt D mesons and non-prompt J/ψ versus the number of participants [15].

high p_T , it constrains the path-length dependence of the parton energy loss, complementing the measurement of the nuclear modification factor R_{AA} .

2. Heavy-quark energy loss

Nuclear effects are typically quantified using the nuclear modification factor R_{AA} where the particle yield in nucleus-nucleus collisions is divided by the yield in pp reactions scaled by the number of binary collisions. $R_{AA} = 1$ would indicate that no nuclear effects, such as Cronin effect, shadowing or gluon saturation, are present and that nucleus-nucleus collisions can be considered as an incoherent superposition of nucleon-nucleon interactions.

The left panel of Fig. 1 shows the transverse momentum dependence of the nuclear modification factor R_{AA} for D^0 mesons in the Au+Au collisions at $\sqrt{s_{NN}} = 200$ GeV from the STAR experiment at the Relativistic Heavy Ion Collider [14]. The R_{AA} is enhanced at around 1.7

GeV/ c and shows a strong suppression at $p_T > 3$ GeV/ c .

The ALICE experiment has measured the transverse momentum dependence of the nuclear modification factor R_{AA} for prompt D^0 , D^+ , D^{*+} and D_s^+ mesons at mid-rapidity in the 7% most central lead-lead collisions at $\sqrt{s_{NN}} = 2.76$ TeV [15]. All D mesons show a strong suppression of their yield (factor of 4-5 at around 10 GeV/ c) and follow a similar trend at low p_T , except the D_s^+ mesons, which are less suppressed. The D_s^+ is of particular interest since it contains a charm and anti-strange quark. A higher production yield for D_s^+ mesons at intermediate p_T is expected due to the enhancement of strangeness production and if it hadronises via recombination in the medium.

The centrality dependence of high- p_T prompt D mesons measured by ALICE [15] and J/Ψ mesons from B decays measured by CMS [16] are shown in Fig. 1 (right panel). The D and B mesons were selected in a compatible p_T range, namely $\langle p_T^B \rangle \approx 11$ GeV/ c and $\langle p_T^D \rangle \approx 10$ GeV/ c . The data indicate a larger suppression of D mesons in particular for the most central collisions. This is the first clear indication that in-medium parton energy loss decrease with increasing quark mass. However, further theoretical developments are needed to directly link these measurements to the drag diffusion coefficient of heavy quarks. This quantity was recently calculated in Lattice QCD [17].

To quantitatively understand the heavy ion data in terms of energy loss, it is important to disentangle hot nuclear matter effects from initial-state effects due to cold nuclear matter, such as the modification of the parton distribution functions in the nucleus [18] and saturation effects in the heavy flavour sector [19].

3. Cold nuclear matter effects

Initial-state effects can be investigated by measuring D production in p-Pb collisions. The nuclear modification factor of the averaged prompt D^0 , D^+ and D^{*+} mesons in minimum bias p-Pb at $\sqrt{s_{NN}} = 5.02$ TeV from ALICE is depicted in Fig. 2 (left panel). The R_{AA} is compatible with unity within systematic uncertainties over the full p_T range. The data are compared with pQCD calculations based on the HVQMNR

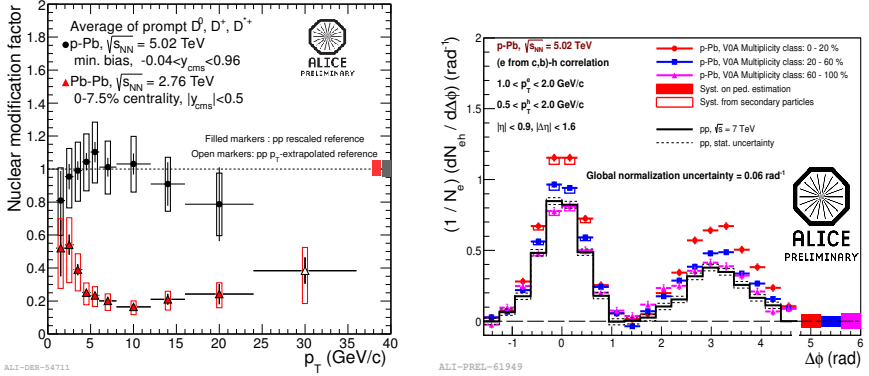


Fig. 2: Left panel: R_{AA} of prompt D mesons (averaged) versus p_T for the 7.5% most central Pb-Pb collisions (red triangle) at $\sqrt{s_{NN}} = 2.76$ TeV [15] and minimum bias p-Pb collisions at $\sqrt{s_{NN}} = 5.02$ TeV (black squares) [21]. Right panel: Azimuthal angular distribution between heavy flavour decay electrons and charged hadrons for three different multiplicity classes in p-Pb collisions at $\sqrt{s_{NN}} = 5.02$ TeV [22].

model calculations [20] combined with the EPS09 modifications of the parton distribution functions [18] and with a Color Glass Condensate-based calculation [19]. Both theoretical models describe the data within experimental uncertainties. Thus, the strong suppression of the heavy flavour hadron yield observed in central Pb-Pb collisions is indeed a final-state effect and arising from the hot QCD matter.

The right panel of Fig. 2 depicts the azimuthal angular distribution between heavy flavour decay electrons and charged hadrons for three different multiplicity classes in p-Pb collisions at $\sqrt{s_{NN}} = 5.02$ TeV [22], measured by the ALICE experiment. It was shown that the correlation yield for low- p_T electrons (1-2 GeV/c) exhibits a long-range correlation in η direction for the highest multiplicity class (0-20%) compared to the low multiplicity class (60-100%) and elementary pp interactions. This "double ridge-like structure" can be interpreted in terms of hydrodynamic expansion of the systems or with the Colour Glass Model [19].

4. Azimuthal anisotropy of heavy-flavour particles

Measurements of the momentum distribution of emitted particles and comparison with hydro-dynamic model calculations have shown that the outward streaming particles move collectively, with the patterns arising from variations of pressure gradients early after the collision. This phenomenon is called azimuthal anisotropy or elliptic flow and is analogous to the properties of fluid motion. The study of the azimuthal anisotropy of heavy-quark particles is particularly interesting as it provides information on the degree of thermalisation of heavy quarks in the medium. Sensitive measurements of the azimuthal anisotropy of electrons from heavy-flavour decays and prompt open charmed mesons in peripheral heavy-ion collisions indicate a sizeable flow of heavy quarks.

The transverse momentum dependence of the elliptic flow coefficient v_2 of D mesons [23] is depicted in Fig. 3 (left panel) together with that of inclusive charged hadrons for the centrality interval 30-50%. Despite the large uncertainties, the v_2 measurement of charmed mesons shows a sizeable anisotropy ($3-5\sigma$), suggesting that charm quarks may take part in the collective motion generated at the quark level in the deconfined stage. The v_2 results are confronted with theoretical model calculations in Fig. 3 (right panel). The models describe the features of the data reasonably well, but a quantitative description of both energy loss and elliptic flow remains challenging for them.

The semi-leptonic decay of D and B mesons, with a branching ratio of about 10%, also provides an access to study open charm and beauty production. The transverse momentum dependence of the heavy flavour decay electron R_{AA} and v_2 at midrapidity in lead-lead collisions at $\sqrt{s_{NN}} = 2.76$ TeV in the centrality range 0-10% and 20-40%, respectively, by ALICE are shown in Fig. 4. Muons from heavy-flavour hadron decays at forward rapidity ($-4 < \eta < -2.5$) have, within uncertainties, a similar R_{AA} as single electrons in the p_T range 4-10 GeV/ c (not shown in Fig. 4). Both single electrons and muons are suppressed to the same level as observed for prompt D mesons for $3 < p_T < 7$ GeV/ c , giving a clear indication for substantial energy loss of heavy quarks in the medium. The single electron R_{AA} is higher than the prompt charmed meson R_{AA}

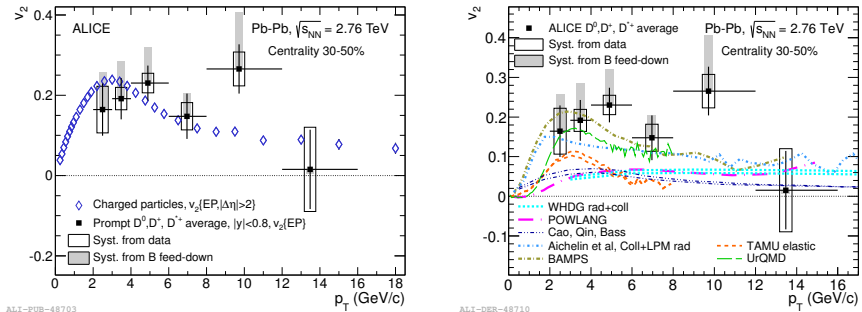


Fig. 3: Transverse momentum dependence of the elliptic flow coefficient v_2 of D mesons for the centrality class 30-50% (full black squares) [23], compared to (left panel) data for charged hadrons (blue open triangles) and to various theoretical model calculations (left panel).

for $p_T > 7$ GeV/ c due to the beauty contribution. ATLAS measured the centrality dependence of the R_{CP} of single muons at midrapidity. The R_{CP} decreases continuously from low to high centralities and reaches 0.4-0.5 at $\langle N_{part} \rangle = 350$ [24].

The non-zero v_2 observed in the 20-40% central lead-lead events suggests that heavy quarks experience strong re-interactions within the medium, as for prompt D mesons, and that they may take part in the collective motion built up at the quark level in the deconfined stage. For the first time the LHC allows more differential, precision measurements of heavy quark production (R_{AA} , v_2 , its centrality dependence and heavy flavour particle correlations) in heavy ion collisions. As illustrated in Fig. 4, a simultaneous description of the nuclear modification factor and elliptic flow coefficient for heavy-flavour particles is challenging for current theoretical model calculations.

5. Summary and outlook

Heavy quarks (charm and beauty) are particularly good probes to study the dynamical properties of the Quark-Gluon Plasma, created in high-energy heavy-ion collisions. LHC measurements in central lead-lead collisions at $\sqrt{s_{NN}} = 2.76$ TeV have shown that the yield of prompt D

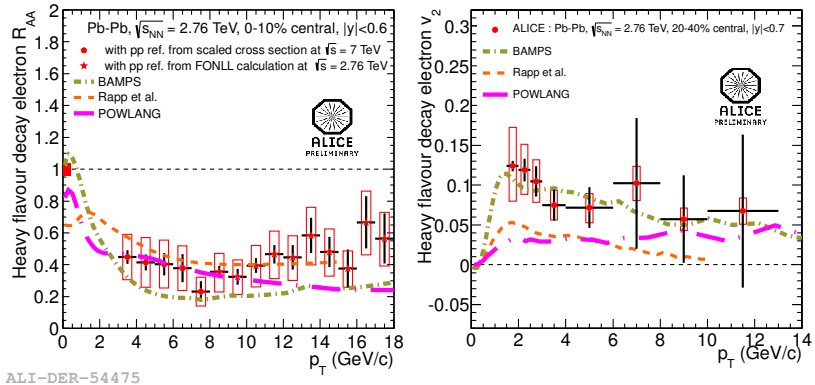


Fig. 4: Transverse momentum dependence of the heavy flavour decay electron R_{AA} (left panel) and v_2 (right panel) at midrapidity in lead-lead collisions at $\sqrt{s_{NN}} = 2.76$ TeV in the centrality range 0-10% and 20-40%, respectively. The data are compared with different theoretical model calculations.

mesons, with respect to pp interactions, are suppressed to the same level as observed for light-quark hadrons, leading to the conclusion that these quark flavours have similar interactions with the medium constituents. First indications have been found that beauty experiences less energy loss in the hot QCD medium. More data are needed for the quantitative understanding of fundamental quantities of the QGP such as the transport coefficient. The increase of the interaction rate expected for the LHC Run-3, after the second long shutdown (2018–19), requires a significant upgrade of the experimental apparatuses, that will allow a substantial improvement of the current performances for what concerns the heavy-flavour reconstruction capabilities, especially at low momenta.

Acknowledgments

I thank the organisers for the invitation and the inspiring atmosphere at the conference. Sincerest thanks to the ALICE, ATLAS and CMS Collaboration for providing the data and the LHC accelerator team.

This work was also supported by a Vidi grant from the Netherlands Organisation for Scientific Research (project number 680-47-232) and

Projectruimte grants from the Dutch Foundation for Fundamental Research (project numbers: 10PR2884 and 12PR3083).

1. M. Gyulassy and M. Plümer, *Phys. Lett. B* 243, 432 (1990).
2. X.-N. Wang and M. Gyulassy, *Phys. Rev. Lett.* 68, 1480 (1992).
3. R. Baier, Yu. L. Dokshitzer, A. H. Mueller, S. Peigné and D. Schiff, *Nucl. Phys. B* 483, 291 (1997).
4. R. Baier, Yu. L. Dokshitzer, A. H. Mueller, S. Peigné and D. Schiff, *Nucl. Phys. B* 484, 265 (1997).
5. M. H. Thoma and M. Gyulassy, *Nucl. Phys. B* 351 (1991) 491.
6. E. Braaten and M. H. Thoma, *Phys. Rev. D* 44 (1991) 1298 and *Phys. Rev. D* 44 (1991) 2625.
7. S. Wicks, W. Horowitz, M. Djordjevic, M. Gyulassy, *Nucl. Phys. A* 784, 426 (2007).
8. M. Djordjevic, M. Gyulassy and S. Wicks, *Phys. Rev. Lett.* 94, 112301 (2005).
9. N. Armesto, C. A. Salgado, and U. A. Wiedemann, *Phys. Rev. D* 69, 114003 (2004).
10. Yu. L. Dokshitzer, D. Kharzeev, *Phys. Lett. B* 519, 199 (2001).
11. A. Adil and I. Vitev, *Phys. Lett. B* 649, 139 (2007).
12. R. Sharma, I. Vitev and B.-W. Zhang, *Phys. Rev. C* 80, 054902 (2009).
13. V. Greco, C. M. Ko and R. Rapp, *Phys. Lett. B* 595, 202 (2004).
14. L. Adamczyk et al. (STAR Collaboration), *Phys. Rev. Lett.* 113, 142301 (2014).
15. B. Abelev for the ALICE Collaboration, *J. High Energy Phys.* 9, 112 (2012).
16. CMS Collaboration, CMSPASHIN12014.
17. D. Banerjee, S. Datta, R. Gavai and P. Majumdar, *Phys. Rev. D* 85, 014510 (2012).
18. K. J. Eskola H. Paukkunen and C. A. Salgado, *JHEP* 0904, 065 (2009).
19. H. Fujii and K. Watanabe, *Nucl Phys. A* 920, 78 (2013).
20. M. Mangano, P. Nason and G. Ridolfi, *Nucl. Phys. B* 373, 295 (1992).
21. B. Abelev for the ALICE Collaboration, submitted to *Phys. Rev. Lett.* (arXiv:1405.3452), May 2014.
22. E. Pereira de Oliveira Filho for the ALICE Collaboration, arXiv:1404.3983.
23. B. Abelev et al. (ALICE Collaboration), *Phys. Rev. Lett.* 111, 102301 (2013).
24. ATLAS Collaboration, ATLAS-CONF-2012-050, 26 May 2012.

Directed Flow and Freeze-Out in Heavy-Ion Collisions in the Energy Range of Beam Energy Scan at RHIC

L. Bravina¹, E. Zabrodin^{1,2}

¹ *Department of Physics, University of Oslo, Oslo, Norway*

² *Skobeltsyn Institute of Nuclear Physics, Moscow State University, Moscow, Russia*

Preface

We began to work with Laszlo Csernai more than 20 years ago. Among other interesting problems, he brought to our attention the issue of collective flow (at that time it was decomposed into in-plane bounce-off and out-of-plane squeeze-out flows) and freeze-out in relativistic heavy-ion collisions. Since then the interests of heavy-ion community to the reaction energies made almost a loop from few GeV at SIS and AGS to the TeV-range at LHC and back to several GeV at beam energy scan (BES) at RHIC and at coming soon FAIR and NICA facilities. Recent discoveries of STAR collaboration of the peculiarities in behavior of proton directed flow at $7.7\text{GeV} \leq \sqrt{s} \leq 39\text{GeV}$ simply confirm our old results and predictions. Here we would like to remind some basic trends in the development of hadronic directed flow in A+A collisions at energies between AGS and SPS.

1. INTRODUCTION

The study of properties of extremely hot and dense nuclear matter, and the search for anticipated transition to a deconfined phase of quarks and gluons, the so-called Quark-Gluon Plasma (QGP), is one of the main objectives of heavy ion experiments at ultrarelativistic energies. Both theorists and experimentalists are looking for genuine QGP fingerprints, that cannot be masked or washed out by processes on a hadronic level.

At present, the expansion of highly compressed nuclear matter in the direction perpendicular to the beam axis of the colliding heavy ions, known as collective flow, is believed to be one of the most promising signals to detect the creation of the QGP [1]. Since the development of flow is closely related to the equation of state (EOS) of nuclear matter, the investigation of the flow can shed light on the transition to the QGP phase accompanied by its subsequent hadronization [2–8]. If the transition from the QGP to hadronic phase is of first order, the vanishing of the pressure gradients in the mixed phase leads to the so-called softening of the EOS [3,4]. The latter should be distinctly seen in the behavior of the excitation function of the collective flow. This circumstance explains the great interest in the transverse flow phenomenon.

The Fourier expansion technique is usually employed to study collective flow phenomena since [9]. The invariant distribution $E d^3N/d^3p$ is presented as

$$E \frac{d^3N}{d^3p} = \frac{1}{2\pi} \frac{d^2N}{p_t dp_t dy} \left[1 + 2 \sum_{n=1}^{\infty} v_n \cos(n\phi) \right], \quad (1)$$

where p_t and y are the transverse momentum and the rapidity, and ϕ is the azimuthal angle between the momentum of the particle and the reaction plane. The first Fourier coefficients in Eq. (1) are dubbed directed flow v_1 , elliptic flow v_2 , triangular flow v_3 and so forth. Since all harmonics of the anisotropic flow depend on rapidity y , transverse momentum p_t , and the impact parameter of an event b (i.e., $v_n \equiv v_n(x_j)$, where $\{x_{j=1,2,3}\} \equiv \{y, p_t, b\}$), the following differential distributions are usually applied

$$v_n(x_i, \Delta x_{j \neq i}) = \int_{x_j^{(1)}}^{x_j^{(2)}} \cos(n\phi) \frac{d^3N}{d^3x_j} d^2x_{j \neq i} \bigg/ \int_{x_j^{(1)}}^{x_j^{(2)}} \frac{d^3N}{d^3x_j} d^2x_{j \neq i} . \quad (2)$$

Model calculations suggest that elliptic flow is built up at the early phase of nuclear collisions, whereas directed flow develops until the late stage of the reaction. But it is well known that the particles with high transverse momentum are emitted at the onset of the collective expansion, i.e., their directed flow can carry information about the EOS of

the dense nuclear phase. The study of the collective flow development is, therefore, closely connected to the freeze-out picture. The microscopic quark-gluon string model (QGSM) [10,11] was employed to investigate some aspects of the anisotropic flow formation and evolution in heavy-ion collisions at energies from AGS ($E_{lab} = 10.7$ AGeV) to SPS ($E_{lab} = 40$ and 160 AGeV) corresponding to change of the center-of-mass energy from $\sqrt{s} = 4.7$ AGeV to $\sqrt{s} = 17.4$ AGeV.

2. QUARK-GLUON STRING MODEL

The model is based on the $1/N_c$ (where N_c is the number of quark colors or flavors) topological expansion of the amplitude for processes in quantum chromodynamics and string phenomenology of particle production in inelastic binary collisions of hadrons. The diagrams of various topology, which arose due to the $1/N_c$ expansion, correspond at high energies to processes with exchange of Regge singularities in the t -channel. For instance, planar and cylindrical diagrams corresponds to the Reggeon and Pomeron exchange, respectively. The QGSM treats the elementary hadronic interactions on the basis of the Gribov-Regge theory (GRT), similar to the dual parton model [12] and the NEXUS model [13]. This implies the consideration of subprocesses with quark annihilation and quark exchange, corresponding to Reggeon exchanges in two-particle amplitudes in the GRT, and with color exchange, corresponding to the one and more Pomeron exchanges in elastic amplitudes. The hh collision term includes also single and double diffraction subprocesses, antibaryon-baryon annihilation and elastic scattering, as well as the hard gluon-gluon scattering with large $Q^2 > 1$ (GeV/c)² momentum transfer [14].

Using the Abramovskii-Gribov-Kancheli (AGK) cutting rules [15] one can determine the number of cut soft and hard Pomerons, i.e., the number of strings and hard jets, in inelastic hh interactions. The single Pomeron exchange leads to the formation of two quark-diquark or quark-antiquark strings. With rising energy the processes with multi-Pomeron exchanges become more and more important. The contribution of the cylinder diagrams to the scattering amplitude increases like $s^{\alpha_P(0)-1}$,

while that of the so-called chain diagrams corresponding to n -Pomeron exchanges ($n \geq 2$) rises like $s^{n[\alpha_P(0)-1]}$ with $\alpha_P(0) > 1$ being the intercept of a Pomeron pole. Strings, which are formed in the course of a hh or A+A collision, decay later into secondary hadrons. Similar to hadronic collisions, string fragmentation into hadrons proceeds independently in A+A collision also. However, in the latter case these hadrons are allowed to interact with other hadrons after a certain formation time, while the valence quarks and diquarks can interact promptly with the reduced cross sections.

The transverse motion of hadrons in the QGSM arises from different sources: (i) primordial transverse momentum of the constituent quarks, (ii) transverse momentum of (di)quark-anti(di)quark pairs acquired at string breakup, (iii) the transverse Fermi motion of nucleons in colliding nuclei, and (iv) rescattering of secondaries. Parameters of the first two sources are fixed by comparison with hadronic data. The Fermi motion changes the effective transverse distribution of strings formed by the valence quarks and diquarks of the target and projectile nucleons. Thus, the original strings are not completely parallel to the beam axis. Further details of the QGSM can be found elsewhere [10,11]. Below we start from the study of energy and centrality dependence of the directed flow.

3. DIRECTED FLOW

The directed flow of nucleons at BEVALAC/SIS energies ($E_{lab} = 0.1$ AGeV - 1 AGeV) and at AGS energy ($E_{lab} = 10.7$ AGeV) has a characteristic S -shape attributed to the standard $\langle p_x/A \rangle$ distribution. It grows linearly with rising rapidity between the target and projectile fragmentation regions. Conventionally, we will call this type of flow, for which the slope dv_1/dy_{cm} is positive, *normal* flow, in contrast to the *antiflow* for which $dv_1/dy_{cm} < 0$ in the midrapidity region.

The one-fluid hydrodynamic models indicate that deviations from the straight line behavior of the nucleon flow can be caused solely by the softening of the EOS due to the QGP creation [5, 6], as shown in Fig. 1. In microscopic string model calculations such deviations were first observed in very peripheral Au+Au collisions at AGS energy [16],

see Fig. 2. It appeared, however, that the effect is shifted to more central topologies [17–19] as the collision energy increases.¹ The phenomenon leading to the formation of a characteristic *wiggle* structure [21] of the directed flow is caused by shadowing, which plays a decisive role in the competition between normal flow and antiflow in noncentral nuclear collisions at ultrarelativistic energies.

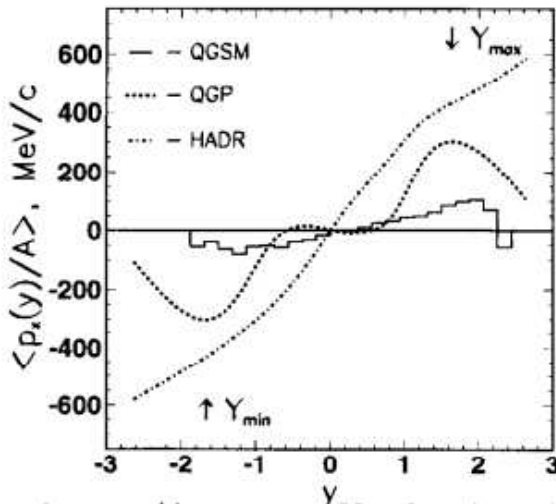


Fig. 1: $\langle p_x/A \rangle$ vs. c.m. rapidity for Au+Au collisions at 11.6 AGeV/c obtained in QGSM with $b = 3$ fm (histogram). Results of Fluid Dynamical Model with $b = 5$ fm with hadronic and with QGS EOS are shown by dashed and dash-dotted lines, respectively (from [5]).

Hadrons, emitted with small rapidities in the antiflow area, can propagate freely, whereas their counterparts will be absorbed by dense baryon-rich matter. Another interesting fact is that the antiflow of protons at midrapidity emerges in light-ion collisions in more central topologies, compared to heavy-ion ones. To understand this effect the space-time development picture of baryonic density and velocity of the cells, as displayed in Fig. 3, was considered [16, 22]. For light systems the early pre-equilibrium particle emission starts to develop around $t = 3 - 4$ fm/c.

¹The last two papers were somehow overlooked by the STAR collaboration [20].

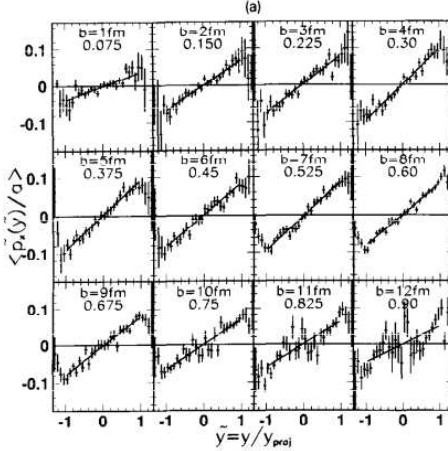


Fig. 2: Average transverse flow of protons vs. reduced rapidity calculated in QGSM for Au+Au collisions at AGS. Line shows the linear fit of the data (from [16]).

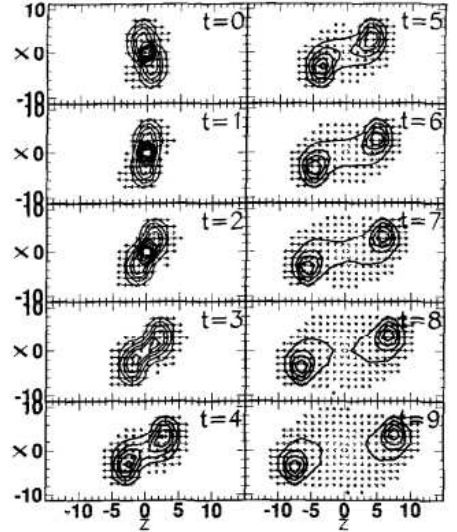


Fig. 3: Space-time evolution of the baryon density (contours) and collective velocity (arrows) of the cells with volume 3 fm³, calculated for peripheral S+S collisions at 11.6 AGeV/c (from [16]).

This is deflected to the opposite side of the reaction plane than the excited spectator matter which develops later around $t = 6 - 9$ fm/c, and which is also faster, being close to the target and projectile rapidities. This pre-equilibrium component gets relatively weaker in heavy systems. The two separated peaks in opposite x -directions are due to spectators, which propagate parallel to the beam and absorb particles from the hot emitting source.

Figure 4 depicts the directed flow of nucleons and pions in two p_t intervals, (a) $0.3 < p_t < 0.6$ GeV/c and (b) $0.6 < p_t < 0.9$ GeV/c, for Pb+Pb collisions with different centrality. The maximum impact parameter for a symmetric system is $b_{max} = 2R_A$. The value of the reduced impact parameter $\tilde{b} = b/b_{max}$ in the simulations varies from 0.15 (central collisions) up to 0.9 (most peripheral collisions). At $p_t < 0.6$ GeV/c the pionic flow exhibits the typical antiflow in both, semicentral and periph-

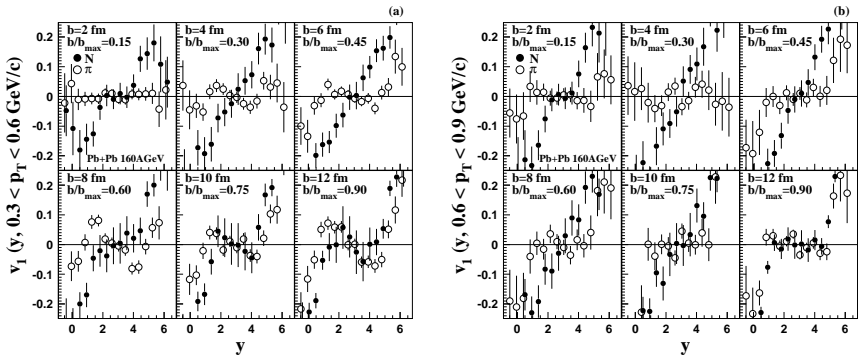


Fig. 4: (a) Centrality dependence of directed flow $v_1(y, \Delta p_t)$ of nucleons (solid circles) and pions (open circles) in the transverse momentum interval $0.3 < p_t < 0.6$ GeV/c in Pb+Pb collisions at 160A GeV. (b) The same as (a) but for $0.6 < p_t < 0.9$ GeV/c (from [19]).

eral, collisions. In the same p_t interval the nucleon flow increases as the reaction becomes more peripheral. But at $b \approx 8$ fm the flow becomes softer in the midrapidity range. In very peripheral collisions the directed flow of nucleons shows an antifold behavior which is similar to that of the pionic directed flow. It is well known that the presence of even a small amount of quark-gluon plasma leads to a softening of the equation of state, which results in a significant reduction of the directed flow. However, since the QGP is expected to be produced primarily in central heavy-ion collisions, the effect should be most pronounced in semicentral collisions, where the antifold reaches its maximum strength with the subsequent vanishing in peripheral ones [23]. In contrast, shadowing causes the disappearance of nucleon directed flow and the development of antifold in the midrapidity region especially in semiperipheral and peripheral collisions, as well as in light systems.

The behavior of directed flow changes drastically in the transverse momentum range $0.6 < p_t < 0.9$ GeV/c, presented in Fig. 4(b). Although the nucleon directed flow decreases in the midrapidity range at $b \geq 10$ fm, its normal component still dominates over the antifold coun-

terpart. Moreover, even high- p_t pions prefer the direction of normal flow, distinctly seen in semiperipheral events with $4 \leq b \leq 6$ fm. This reflects again that hadrons with high transverse momenta ($p_t \geq 0.6$ GeV/ c) are produced mainly at the early stage of nuclear collisions.

4. FREEZE-OUT OF HADRONS

Figure 5 depicts the distribution of the emitted nucleons and pions over longitudinal coordinate and time. Both for light (S+S) and for heavy (Pb+Pb) colliding systems the distribution of the final-state hadrons, $d^2N/dtdz$, over the (t, z) coordinates of their last interactions shows that the particles are emitted from the whole available space-time region. In this respect the freeze-out picture obtained in QGSM is different from that of the Landau or Bjorken model [24–26], based on sharp freeze-out. Nevertheless, the shape of the contours is concave and similar to the Bjorken proper-time surface. This is partially due to the fact that the transverse spacial coordinates (x, y) are integrated over.

For all cases the QGSM predicts a high narrow peak coming from the beginning of the reaction (early emitted particles). However, the integrated number of particles coming from the peak is not so high: there are about 200 pions and 40 nucleons for the heavy Pb+Pb system.

Later on the emissivity drops gradually with increasing t and z . The emission region spreads throughout the whole region inside the lightcone. The picture is very different for nucleons and pions in Pb+Pb collisions. In addition to the narrow high peak at small values (z, t) for nucleons, there appears a broad and flat maximum at $z = \pm 5$ and $t = 17-28$ fm/ c . This plateau corresponds to the “thermal” component of the nucleon distribution due to many elastic and inelastic collisions.

Figure 6 shows the contributions of the hadrons which go to the detector after their last inelastic and elastic collision or a resonance decay. In both S+S and Pb+Pb collisions the dN/dt distributions presented in Fig. 6 have a sharp peak corresponding to the first (which is also the last) inelastic collision. Subsequent elastic rescatterings or decays spread out the distribution to the later times. In Pb+Pb collisions the contribution of initial interactions is almost entirely washed out for nucleons,

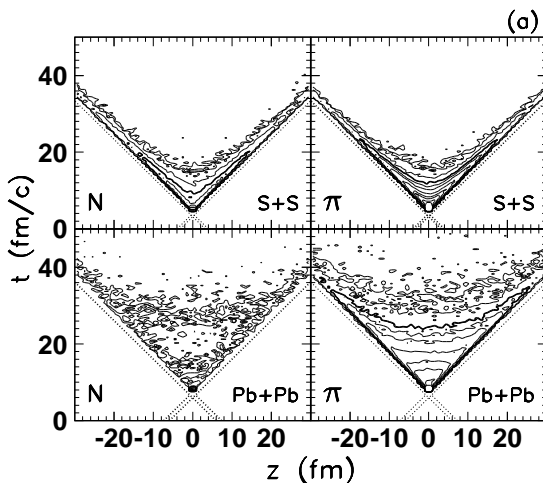


Fig. 5: $d^2N/dzdt$ distribution of the final-state hadrons over (t, z) coordinates of their last elastic and inelastic collision points. Distributions are presented separately for nucleons (left panels) and pions (right panels), produced in S+S (upper row) and Pb+Pb (lower row) central ($b = 0.2$ fm) collisions at 160 AGeV/c. The dotted lines show the trajectories of the nuclear edges (from [28]).

because of the large number of rescatterings. But even in this case the distributions are wide with maxima shifted to later times.

The contours of the $d^2N/m_T dm_T dt$ distributions of the final-state hadrons in the (m_T, t) plane are displayed in Fig. 7. Here $m_T = \sqrt{p_T^2 + m_0^2}$ is the transverse mass of a particle with rest mass, m_0 . One can see the difference between pion and nucleon emission in the case of heavy nuclei. The pions with large transverse momenta are emitted only at the initial stages of the S+S and Pb+Pb reactions. They are produced in inelastic primary NN collisions. In contrast to pions the nucleons with maximal transverse momenta in Pb+Pb collisions are coming from the intermediate times $(t - t_0) = 12 - 14$ fm/c. Soft hadrons are emitted during the whole evolution time. The maximum of the emission rate in S+S corresponds to the initial time of the reaction, while in Pb+Pb it is shifted to about $t - t_0 = 14 - 18$ fm/c because of many rescatterings. With growing time the m_T spectra become gradually softer, which can

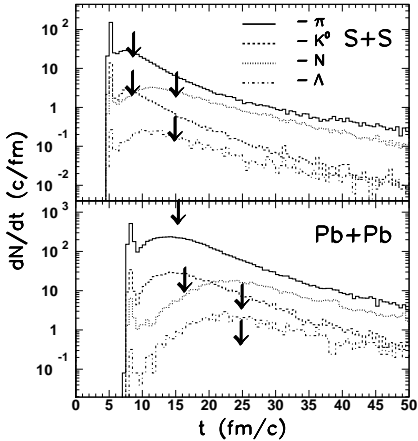


Fig. 6: dN/dt distribution of the particles over their last collision time t for kaons (dashed), pions (solid), nucleons (dotted) and lambdas (dash-dotted histograms) for S+S (upper row) and Pb+Pb (lower row) collisions. The vertical arrows correspond to the average emission times of the species (from [28]).

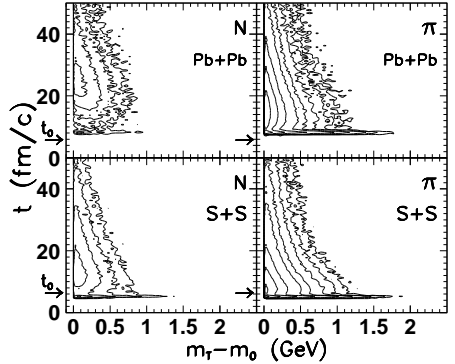


Fig. 7: $d^2N/m_T dm_T dt / A$ distribution of the final-state hadrons over transverse mass m_T and the emission time t for nucleons (left panels) and pions (right panels). The yields are divided by the mass number of the colliding nuclei, $A = 32$ for S+S (lower row) and $A = 208$ for Pb+Pb (upper row) (from [28]).

be interpreted as the cooling of the expanding hadronic matter.

In the case of nucleons in Pb+Pb collisions the contribution of the particles emitted after the first interaction is completely washed out. The transverse momenta are generated to a large extent by multiple rescatterings. It is very likely, therefore, that in Pb+Pb collisions we indeed are dealing with a more or less thermalized source. Further details can be found in [27,28].

5. CONCLUSIONS

In conclusion, directed flow of pions and nucleons is studied within the microscopic transport model QGSM for light- and heavy-ion collisions at energies from $E_{lab} = 10.7A\text{GeV}$ to $E_{lab} = 160A\text{GeV}$. The flow is shown to have a complex structure in the rapidity range $|y| \leq 1.5$, which is

strongly dependent on the centrality of the collision, as well as on the mass number of colliding nuclei. The total directed flow can be decomposed onto the normal component, which follows the outgoing residues of collided ions, and the antiflow component, which develops in the opposite direction, where the baryon matter is more dilute. Although these partial components are relatively large, their mutual cancellation leads to a rather modest signal of the total flow and even to antiflow behavior of nucleon flow in semiperipheral and peripheral collisions. The effect is caused by almost purely geometrical reasons. Hence, it is more distinct in the collisions of light ions. - In hydrodynamics the creation of a QGP is likely to occur in heavy Pb+Pb or Au+Au systems rather than in light-ion systems. The formation even of a small amount of plasma with the subsequent phase transition to the hadron phase can also produce the negative slope of the v_1 -distribution in the midrapidity region. The effect, therefore, should essentially be more pronounced in heavy-ion collisions compared to collisions of light ions with the same reduced impact parameter. - With the rise of incident energy the remnants of nuclei move faster thus giving space for the development of both normal and antiflow components. The resulting flow at midrapidity is closer to zero. Another finding is that high- p_T hadrons, including pions, demonstrate normal-flow behavior in semiperipheral collisions in contrast to low- p_T ones.

Many of these peculiarities are linked to different freeze-out pictures for baryons and mesons. For instance, the flows of particles emitted at the beginning of the collision and during the course of the reaction are quite different. Thus, collective flow and freeze-out of hadrons should not be treated independently. Change of the sign of proton slope of v_1 from positive to negative between $\sqrt{s} = 7.7\text{GeV}$ and $\sqrt{s} = 11.5\text{GeV}$, accompanied by smooth growth to almost zero with rising energy of the collision [20], may indeed indicate the softest point of the EOS and QGP–hadrons first-order phase transition. However, to avoid the ambiguities one has to check in addition to energy dependence the following: (i) centrality dependence of the proton slope of v_1 at midrapidity; (ii) compare heavy-ion colliding systems to lighter ones, such as S+S or Cu+Cu; (iii) study the flow development separately for high- p_T particles.

Further investigations of this exciting problem are in order.

1. Proc. of *Quark Matter'2014*, Nucl. Phys. **A930** 1-1266 (2014).
2. N. S. Amelin et al., Phys. Rev. Lett. **67** 1523 (1991).
3. C.M. Hung and E.V. Shuryak, Phys. Rev. Lett. **75** 4003 (1995).
4. D.H. Rischke and M. Gyulassy, Nucl. Phys. **A597** 701 (1996).
5. L.V. Bravina *et al.*, Nucl. Phys. **A566** 461c (1994).
6. L.P. Csernai and D. Röhrich, Phys. Lett. **B458** 454 (1999).
7. V.P. Konchakovski, W. Cassing, Y.B. Ivanov, V.D. Toneev, Phys. Rev. **C90** 014903 (2014).
8. Y.B. Ivanov and A.A. Soldatov, arXiv:1412.1669.
9. S. Voloshin and Y. Zhang, Z. Phys. **C70** 665 (1996).
10. A.B. Kaidalov and K.A. Ter-Martirosian, Phys. Lett. **B117** 247 (1982);
A.B. Kaidalov, Surveys in High Energy Phys. **13** 265 (1999).
11. N.S. Amelin and L.V. Bravina, Sov. J. Nucl. Phys. **51** 211 (1990); *ibid.* **51** 133 (1990).
12. A. Capella, U. Sukhatme, C.I. Tan, J. Tran Thanh Van, Phys. Rep. **236** 225 (1994).
13. H.J. Drescher *et al.*, Phys. Rep. **350** 93 (2001).
14. N.S. Amelin, E.F. Staubo, L.P. Csernai, Phys. Rev. **D46** 4873 (1992).
15. V. Abramovskii, V. Gribov, O. Kancheli, Sov. J. Nucl. Phys. **18** 308 (1974).
16. L.V. Bravina, Phys. Lett. **B344** 49 (1995).
17. L.V. Bravina, E.E. Zabrodin, Amand Faessler, C. Fuchs, Phys. Lett. **B470** 27 (1999).
18. L.V. Bravina, Amand Faessler, C. Fuchs, E.E. Zabrodin, Phys. Rev. **C61** 064902 (2000).
19. E.E. Zabrodin, C. Fuchs, L.V. Bravina, Amand Faessler, Phys. Rev. **C63** 034902 (2001).
20. L. Adamczyk *et al.* (STAR Collaboration), Phys. Rev. Lett. **112** 162301 (2014).
21. R.J.M. Snellings *et al.*, Phys. Rev. Lett. **84** 2803 (2000).
22. L.V. Bravina, L.P. Csernai, P. Lévai, D. Strottman, Phys. Rev. **C50** 2161 (1994).
23. V.K. Magas, L.P. Csernai, D. Strottman, Nucl. Phys. **A712** 167 (2002).
24. L.D. Landau, Izv. Akad. Nauk SSSR, Ser. Fiz. **17** 51 (1953).
25. F. Cooper and G. Frye, Phys. Rev. **D10** 186 (1974).
26. J.D. Bjorken, Phys. Rev. **D27** 140 (1983).
27. L.V. Bravina *et al.*, Phys. Lett. **B354** 196 (1995).
28. L.V. Bravina *et al.*, Phys. Rev. **C60** 044905 (1999).

Identifying longitudinal rapidity fluctuations and directed flow measurements

G. Eyyubova¹, L.P. Csernai², V.K. Magas³

¹ *Czech Technical University in Prague, Faculty of Nuclear Sciences and Physical Engineering, Prague 11519, Czech Republic and Skobeltsyn Institute of Nuclear Physics, Moscow State University, RU-119991 Moscow, Russia,*

² *Institute of Physics and Technology, University of Bergen, Allegaten 55, 5007 Bergen, Norway and Wigner Research Centre for Physics, 1525 Budapest, Hungary,*

³ *Departament d'Estructura i Constituents de la Matèria, Universitat de Barcelona, 08028 Barcelona, Spain*

Abstract

In heavy ion collisions, fluctuations of energy density in the initial state are essential both in transverse and in longitudinal direction. We present a method to estimate the Event-by-Event (EbE) center of mass rapidity fluctuations with the help of spectators (using ZDC detectors). This enables to separate fluctuating and the global symmetry components in the flow, which is important for the odd flow harmonics, especially for v_1 and v_3 .

Global Collective flow patterns, which follow the global symmetries of the reaction Event-by-Event provide valuable information of the overall pressure and transport properties of matter. Random fluctuations, especially in the initial state, can also lead to flow processes, these however, are not correlated with the global collision geometry and the correlation of the major axis of the asymmetry arising from the fluctuation may have no correlation with the reaction plane at all [1]. Just as the transverse plane fluctuations, the beam directed fluctuations also modify the

initial shape, the tilt of the longitudinal axis and similarly the center of mass (CM) position. The center of mass rapidity fluctuation may arise due to different number of participants in projectile and target. In the work [2] it is shown that the longitudinal center of mass (CM) rapidity fluctuations may essentially change the odd flow signal. Here we describe the method, which makes the measurements more sensitive to the flow patterns showing global collective symmetries, by identifying longitudinal center of mass rapidity fluctuations and then analyzing the collective flow harmonics in the event-by-event center of mass frame. This is particularly important for those harmonic components which are weak and difficult to identify.

1. Longitudinal fluctuations

Let us first introduce center of mass rapidity. The total 4-momentum of all measured particles of one event is given by $P = \sum_{i=1}^M p_i$, where M is the measured multiplicity of the event. The arising center of mass rapidity is

$$y^{CM} = \frac{1}{2} \ln \frac{E + P_z}{E - P_z}. \quad (1)$$

If we do not have a good mass resolution the determination of E_i , and therefore of E , may become problematic, so only the pseudo-rapidity of the CM can be determined:

$$\eta^{CM} = \frac{1}{2} \ln \frac{|\vec{P}| + P_z}{|\vec{P}| - P_z}. \quad (2)$$

If the acceptance covers a large fraction of the momentum space of emitted particles, the initial CM of the system and the measured CM are nearly identical. If the rapidity acceptance of the detector is limited (e.g. to $|\eta| < 0.9$ like ALICE Time Projection Chamber TPC), then the measured longitudinal single nucleon momentum is constrained while the transverse momentum is not constrained. Due to this the TPC is expected to underestimate the CM-rapidity fluctuations.

Center of mass rapidity from spectators can be obtained instead. Let us consider three subsystems: (A) projectile spectators, (B) participants,

and (C) target spectators. We can measure the energies of A and C subsystems in the respective Zero Degree Calorimeters (ZDCs). At the present LHC Pb-Pb reaction, the beam rapidity is $y_0 = 7.986$ and the energy and momentum conservation gives:

$$E_B = E_{Tot} - E_A - E_C ,$$

$$P_{zB} = -(P_{zA} + P_{zC}) \approx -(M_A \sinh(y_0) + M_C \sinh(-y_0)) \quad (3)$$

$$\approx -(E_A - E_C), \quad (4)$$

accounting for that the absolute value of the momentum of the spectators is the same as their energy with rather good approximation. $M_A = A_P m_N$ and $M_C = A_T m_N$ with projectile and target spectator numbers A_P and A_T and neutron mass m_N . E_A and E_C can in principle be measured. For Pb-Pb at the present LHC energy, the energy per nucleon is $\epsilon_N = 1.38$ TeV/nucleon and $E_{Tot} = (208 + 208) * \epsilon_N = 574$ TeV.

Thus for an event, we can determine the rapidity of subsystem B :

$$y_B^{CM} = \text{artanh} \left(\frac{-(E_A - E_C)}{E_{Tot} - E_A - E_C} \right). \quad (5)$$

In central collisions the spectators contain very few, mainly single nucleons, and thus ZDC energies tend to zero. At higher impact parameters, the spectators will become more massive and the energy deposited in the ZDCs is increasing. At peripheral collisions, two residue spectators are expected at opposite sides of the participant zone. These may contain single protons and neutrons as well as bound nuclear fragments. Of these only the single neutrons reach the neutron ZDCs, because all charged fragments are deflected away from the beam direction. The maximum of the total observed neutron energy would be less than $E_{Tot}^n = 2 \times 126 \epsilon_N = 348$ TeV, as one would anticipate from the energy of all initial neutrons in the system. With increasing impact parameter the number of bound nuclear fragments in the spectators increases. This feature was also discussed in [3] in an early simulation for ALICE ZDC, where incomplete spectator fragmentation is taken into account, and HIJING was used as event generator. The correlation between the energy in the ZDCs versus the number of single spectator neutrons, based on theoretical model estimates, raised monotonically up to about 100 neutrons

and then it dropped rapidly. This rapid change was clearly attributed to the fact that for higher impact parameters the measured neutron number did not include neutrons in bound fragments, and thus the ZDC energy peaks at a critical neutron multiplicity [3].

Now the above evaluation of y_{CM} should be reconsidered because the ZDCs measure single neutrons only and the number of single neutrons depends in a special way from the impact parameter due to the formation of nuclear fragments in the spectators or due to the incomplete dissociation of the bound spectator nuclear fragment into single nucleons. We can only do a quantitative estimate of y_{CM} , if we can conclude on the total spectator energy carried by all neutral and charged fragments together. In Eqs.(4, 5) the measured E_A, E_C should be modified, based on the neutron energies measured in the ZDCs.

We know the asymptotic values of the E_{Tot} going from zero to 574 TeV in Pb-Pb, as the impact parameter b increases. Let us first consider that the total collision energy, E_{Tot} , is related in the Pb-Pb collision to the total energy of all neutrons E_{Tot}^n as $E_{Tot} = (208/126)E_{Tot}^n$. The **simplest approximation** is that the total spectator energies, E_A and E_C are related the same way to the measured ZDC energies:

$$E_A = (208/126)E_A^n, \quad E_B = (208/126)E_B^n.$$

This approximation is satisfactory for central collisions and for small impact parameters, b , (i.e. $b < 0.3 \times b_{max}$ so, relatively large charged multiplicities).

We need a **better approximation** at intermediate or higher impact parameters. Based on the initial state model [4] we get the number of participant nucleons (protons and neutrons) for each impact parameter. 126/208 part of these are participant neutrons, shown by dashed blue line in Fig. 1. The remaining neutrons are in spectators, shown by the dotted green line. As in ref. [4], we assume that the N/Z ratio is homogeneous in the whole initial state system.

Since the impact parameter in experiment is not known, we make a correspondence between impact parameter and centrality based on fluid dynamical model calculation (see Fig. 3 of [2]). The impact parameters of the fluid dynamical model calculation can be matched well to the centrality percentages. The correspondence between impact parameter and

event centrality percentage is impressive for semi-peripheral reactions: $b/b_{max} = 0.2, 0.3, 0.4, 0.5, 0.6, 0.7$ correspond to 5, 13, 21, 29, 37, 45 % centrality percentage, respectively.

The number of single neutrons, measured by each of ZDCs, can be estimated as $N_n(\text{centrality}) = \frac{E^n}{\epsilon_N}$. We can know this experimental value per centrality as well as theoretical number of all spectators per impact parameter [4] (see Fig. 1). Given the correspondence between the centrality percentages and impact parameters and theoretical estimation of total number of spectators, the factor $R(b)$ is introduced, which accounts for the correction of measured number of spectators for the total number of spectators. We have to estimate, at a given centrality percentage, the

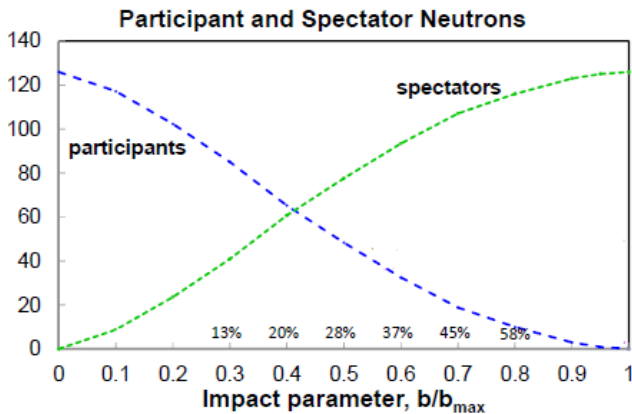


Fig. 1: The number of participant neutrons from the projectile or from the target (dashed blue line) and the corresponding number of spectator neutrons (dotted green line) in one of the spectators (forward or backward) obtained in the initial state calculation [4]. The neutron distribution is assumed to be homogeneous in the system (126/208). The correspondence between the impact parameter and centrality percentage, based on the FD estimates, are shown.

total energy of the spectator residues (including protons and charged fragments), E_A and E_C . Multiplying these numbers by the correction factor, $R(b)$, we get the spectator numbers, $A_{P,T} = N_{A,C}^{sn} R(b)$, and spectator energies, including the contributions of single protons and of all

nucleons bound in composite nuclear fragments:

$$\begin{aligned} E_A(b) &= (A/N)E_A^{sn}R(b) \\ E_C(b) &= (A/N)E_C^{sn}R(b), \end{aligned} \quad (6)$$

where $(A/N) = 208/126$ is the mass to charge ratio in Pb. The correction increases for increasing impact parameter, which leads to increased estimates for y_{CM} fluctuations, on the other hand, the possibilities of larger systematic errors also increase.

Before we start to study the correlations we have to remove the average CM rapidity shift from the data as this arises from asymmetries in detector acceptance. With the corrected E'_A and E'_C we can get the event by event CM rapidity as in eq. (5)

$$y_{CM}^B \approx y'^B_{CM} = \text{artanh} \left(\frac{-(E'_A - E'_C)}{E_{Tot} - E'_A - E'_C} \right) - y_0^{CM}(b), \quad (7)$$

where the last term is due to the fact that average CM rapidity might not be zero because of detector effects.

2. Collective flow measurements with y^{CM} .

The anisotropic particle distribution w.r.t. event plane angle, Ψ_{EP} , reads:

$$E \frac{d^3N}{d^3p} = \frac{1}{2\pi} \frac{d^2N}{p_T dp_T dy} (1 + 2 \sum v_n(y, p_t) \cos(n\varphi - n\Psi_{EP})), \quad (8)$$

$$v_n = \langle \cos[n(\varphi - \Psi_{EP})] \rangle, \quad (9)$$

where the angle brackets denote an average over all particles in all events. Let us now shift each given event to its own CM by the measured y_{CM}^B so that each particle rapidity y_i will be moved to

$$y'_i = y_i - y_{CM}^B. \quad (10)$$

The detector acceptance boundaries will change EbE by this shift. This transformation will not effect the azimuth angle of the emitted particles,

$p_{t,i}$, nor $m_{t,i}$, however, the longitudinal momentum and the energy and hence, a particle rapidity will change $y \rightarrow y'$. Here we use approximation that the pseudorapidity is shifted EbE by the CM rapidity:

$$\eta'_i = \eta_i - y_{CM}^B \quad (11)$$

The flow harmonics is determined by averaging over all particles and events with EbE shift of particles rapidities:

$$v_n(y', p_t) = \langle \cos[n(\phi_i - \Psi_{EP})] \rangle. \quad (12)$$

3. Conclusions

We presented a method how to analyze the collective flow by considering the EbE longitudinal rapidity fluctuation of the participants. The participant CM rapidity can be estimated both from the central tracker and the ZDC detector. The data from central tracker are constrained to the pseudorapidity acceptance range, which impairs the CM rapidity estimate for peripheral reactions. To obtain the estimate for peripheral reactions from the ZDC data one can use the forward and backward spectator energies. Using the ZDC data we describe each event in its own CM frame, and propose to evaluate the collective flow from these shifted data.

The method of shifting the system origin EbE to the participant CM rapidity is effective in separating the flow patterns originating from random fluctuations, and the flow patterns originating from the global symmetry/asymmetry of the initial state.

ACKNOWLEDGMENTS

This publication was supported by the European social fund within the framework of realizing the project "Support of inter-sectoral mobility and quality enhancement of research teams at Czech Technical University in Prague", CZ.1.07/2.3.00/30.0034.

1. A. Bilandzic et al. [The ALICE Collaboration], J. Phys. **G38** 124052 (2011); M. Krzewicki et al. [The ALICE Collaboration], J. Phys. **G38** 124047 (2011).

2. L.P. Csernai, V.K. Magas, H. Stöcker, and D.D. Strottman, Phys. Rev. **C84** 02914 (2001).
3. "Event characterization in ALICE", M. Monteno and the ALICE Collaboration, talk at the conf. "Physics at LHC", Vienna, 13-17 July (2004).
4. V.K. Magas, L.P. Csernai, and D.D. Strottman, Phys. Rev. **C64** 014901 (2001); Nucl. Phys. **A712** 167 (2002).

Higher Flow Harmonics and Cross-Talk of Elliptic and Triangular Flows

E. Zabrodin^{1,2}, L. Bravina¹, B.H. Bruscheim Johansson¹,
J. Crkovska³, G.Kh. Eyyubova^{2,3}, V.L. Korotkikh², I.P. Lokhtin²,
L.V. Malinina^{2,4}, S.V. Petrushanko², A.M. Snigirev²

¹ *Department of Physics, University of Oslo, Oslo, Norway*

² *Skobeltsyn Institute of Nuclear Physics, Moscow State University,
Moscow, Russia*

³ *Czech Technical University in Prague, FNSPE, Prague, Czech
Republic*

⁴ *Joint Institute for Nuclear Researches, Dubna, Russia*

Abstract

HYDJET++ model, which combines parametrised hydrodynamics with jets, is employed to study anisotropic flow in Pb+Pb collisions at LHC. It is shown that the cross-talk of elliptic and triangular flows generated up to 80% of the signal for higher order flow harmonics. The strong contribution from v_2 and v_3 to v_n , $n > 3$ can explain the basic trends in the development of v_4, v_5, v_6 , as well as the absence of correlations between the higher order spatial eccentricities ε_n and the corresponding flow harmonics v_n .

1. Introduction

The importance of collective flow of hadrons as a tool to study the early stage of heavy-ion collisions was first mentioned in [1]. The flow should carry the fingerprints of quark-gluon plasma (QGP) in case of the collisions at ultra-relativistic energies. Modern analysis of the flow in the az-

imuthal plane of the reaction is performed in terms of Fourier series [2,3]

$$E \frac{d^3 N}{d^3 p} = \frac{1}{2\pi} \frac{d^2 N}{p_T dp_T dy} \left\{ 1 + 2 \sum_{n=1}^{\infty} v_n \cos [n(\phi - \Psi_n)] \right\}, \quad (1)$$

where Ψ_n is the azimuth of the participant plane of n -th order, ϕ is the azimuthal angle between the particle transverse momentum p_T and the participant plane, and y is the particle rapidity. The flow harmonic coefficients are

$$v_n = \langle \cos [(n(\phi - \Psi_n))] \rangle, \quad (2)$$

where one has to average over all particles in a single event and then over all events, respectively. Harmonics are called directed (v_1), elliptic (v_2), triangular (v_3), quadrangular (v_4), pentagonal (v_5), hexagonal (v_6) flow and so on. The first two flow components have been studied in heavy-ion collisions at different energies for more than 15 years, whereas systematic investigation of triangular flow and higher harmonics started about 5 years ago. The concept of participant triangularity due to initial-state fluctuations was first introduced in [4]. In model simulations, the triangular flow signal was found to be directly proportional to the participant triangularity. After that, correlations were studied between the higher-order harmonic eccentricity coefficients ε_n , linked to participant plane angles Φ_n , and the final anisotropic flow coefficients v_n and their final anisotropic flow angles Ψ_n ; see, e.g., [5–9]. One of the interesting observations is that just the first few flow harmonics survive after the hydrodynamic evolution despite the fact that the initial spacial anisotropies are of the same order [6]. It appears that the final plane angles Ψ_n , $n > 3$ are uncorrelated with the corresponding participant plane angles Φ_n , $n > 3$, associated with initial anisotropies [10]. In contrast, the response of the elliptic flow to ellipticity, as well as that of the triangular flow to triangularity, is approximately linear [8]. Our study within the HYDJET++ model (HYDroynamics with JETs) indicates [11, 12] significant contribution of v_2 and v_3 to higher order flow coefficients. The cross-talk of elliptic and triangular flows is able to wash out the original correlations between the initial ε_n and the final v_n . The main results are presented below.

2. HYDJET++ model

Monte Carlo event generator HYDJET++ [13] is the first model designed for the simulation of relativistic heavy-ion collisions which contains a hydrodynamics coupled to a hard multiparton state. Both soft and hard states are treated independently. The predecessors of the HYDJET++ in soft and hard sectors are FASTMC [14] and PYQUEN [15] event generators, respectively. The soft part of the model represents a relativistic hydrodynamical parametrization of the chemical (single freeze-out scenario) or thermal (double freeze-out scenario) freeze-out hypersurfaces with given freeze-out conditions. For the most appropriate scheme with separated chemical and thermal freeze-out, the particle composition in the system is frozen at the stage of chemical freeze-out. The fireball continues to expand and cools down until the thermal freeze-out stage, where the contact between hadrons is lost. The final state interactions (FSI) take into account the two- and three-body decays of the resonances. The model benefits from the extremely rich table of resonances with ca. 350 particles taken from the SHARE thermal model [16]. Note, that HYDJET++ employs its own original routine for treatment of resonance decays.

In hard sector the model propagates the hard partons through the expanding quark-gluon plasma and takes into account both gluon radiation loss and collisional loss because of the parton rescattering. For each hard nucleon-nucleon (NN) collision the PYQUEN routine starts with generation of initial parton spectra and production vertexes at a given impact parameter. In recent version of the model [11, 12] the tune ProQ20 of PYTHIA is used. After the rescattering stage accompanied by radiative and collisional energy loss the partons and in-medium emitted gluons are hadronized according to the Lund string model. The hard event includes also jets. Their number is proportional to the product of number of binary NN collisions in an event at given impact parameter and the integral cross section of the hard processes in NN collision with the minimal transverse momentum transfer, p_T^{\min} .

The flow components are implemented in the HYDJET++ as follows. For noncentral collisions the transverse radius of the overlap region is a

function of impact parameter b , azimuthal angle ϕ and spatial eccentricity $\epsilon(b) = (R_y^2 - R_x^2)/(R_y^2 + R_x^2)$ [14],

$$R_{ell}(b, \phi) = R_{fr.-out}(b) \sqrt{\frac{1 - \epsilon^2(b)}{1 + \epsilon(b) \cos 2\phi}} \quad (3)$$

with

$$R_{fr.-out}(b) = R_0 \sqrt{1 - \epsilon(b)}. \quad (4)$$

Parameter $R_0 \equiv R_{fr.-out}(0)$ is the freeze-out radius of the fireball in a central collision. The momentum anisotropy arises from the pressure gradients, which are stronger in the direction of short axis of the ellipsoid. Then, the azimuthal angle ϕ_{fl} in HYDJET++ does not coincide with the azimuthal angle ϕ as in the case of transverse isotropic parametrization. Instead, both angles are linked via the nonzero flow anisotropy parameter $\delta(b)$ as [14]

$$\frac{\tan \phi_{fl}}{\tan \phi} = \sqrt{\frac{1 - \delta(b)}{1 + \delta(b)}}. \quad (5)$$

Parameters $\epsilon(b)$ and $\delta(b)$ are proportional to the initial spatial anisotropy $\epsilon_0 = b/(2R_A)$. Triangular flow in the model is obtained by further modification of the transverse radius [11]

$$R_{triang}(b, \phi) = R_{ell}(b, \phi) \{1 + \epsilon_3(b) \cos [3(\phi - \Psi_3)]\}. \quad (6)$$

Position of the plane Ψ_3 in the generated events is isotropically distributed w.r.t. the plane Ψ_2 in accord with the experimental data. A new free parameter $\epsilon_3(b)$ is responsible for appearance of triangularity in the system. All higher eccentricities $\epsilon_n, n \geq 4$ are absent. This enables us to study the pure contributions of v_2 and v_3 to higher flow harmonics.

3. Higher flow harmonics

Systematic study of higher flow harmonics $v_n, n > 3$ started relatively recently. The following theoretical estimates are obtained within the framework of relativistic hydrodynamics at high transverse momenta:

$$v_4 \simeq \frac{1}{2}v_2^2 [17], \quad v_5 \simeq v_2 \cdot v_3 [9] \quad \text{and} \quad v_6 \simeq \frac{1}{6}v_2^3 + \frac{1}{2}v_3^2 [12].$$

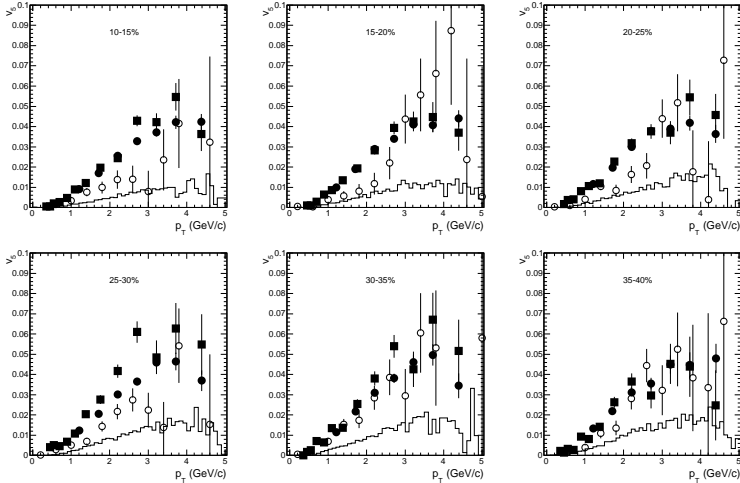


Fig. 1: Pentagonal flow of charged hadrons in Pb+Pb collisions at $\sqrt{s} = 2.76$ TeV (from [11]). See text for details.

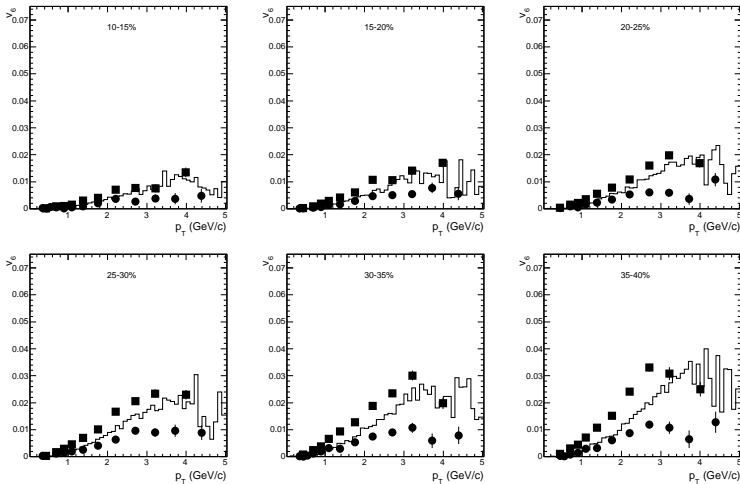


Fig. 2: Hexagonal flow of charged hadrons in Pb+Pb collisions at $\sqrt{s} = 2.76$ TeV (from [11]).

Pentagonal and hexagonal flow coefficients in non-central lead-lead collisions at $\sqrt{s} = 2.76$ TeV are shown as functions of p_T in Figs. 1 and 2, respectively. Here the HYDJET++ results are compared to CMS data [18], restored by the event-plane (EP) method (full squares) and 2-particle cumulants (full circles). Histograms represent $v_{5(6)}(\Psi_3^{\text{RP}})$ and open circles in Fig. 1 display pentagonal flow $v_5\{\text{EP}\}$, respectively, for HYDJET++ calculations. Because of absence of genuine eccentricities $\varepsilon_{5(6)}$ and related to it reaction planes $\Psi_{5(6)}$ in the present version of the model, the generated harmonics shown in Figs. 1 and 2 arise only as a result of interplay of v_2 and v_3 . Direct check in HYDJET++ reveals that $v_5 = 0$ if either elliptic or triangular flow is absent. If, however, the event-plane method is applied to generated particle spectra, the reconstructed pentagonal flow in the model appears to be very close to the distributions extracted from the experimental data, especially for semi-peripheral events.

The situation with the hexagonal flow is even more curious, because the v_6 emerging in the model is not a product but rather a sum of independent contributions coming from v_2 and v_3 . This leads to a non-trivial correlations between the (Ψ_2, Ψ_6) and (Ψ_3, Ψ_6) event planes. Triangular flow weakly increases with rising non-centrality of the collisions, whereas elliptic flow is almost zero for central 0-5% collisions and quickly rises up as the reactions become more peripheral. As a result, for central events hexagonal flow is mainly determined by the v_3 , and Ψ_6 plane should be closer to Ψ_3 plane. In semi-peripheral and peripheral collisions the situation is opposite. Here elliptic flow dominates over the triangular flow, thus Ψ_6 is elongated closer to Ψ_2 rather than to Ψ_3 [12]. This tendency is clearly seen in Fig. 3, where hexagonal flow averaged in several p_t intervals is shown as a function of centrality in both Ψ_2 and Ψ_3 planes. In the $\{\Psi_2\}$ plane v_6 is weak in semicentral collisions but gradually increases for more peripheral reactions, whereas $v_6\{\Psi_3\}$ is maximal in semicentral collisions and then drops. Similar behavior was observed in plane correlators $\langle \cos 6(\Psi_2 - \Psi_6) \rangle$ and $\langle \cos 6(\Psi_3 - \Psi_6) \rangle$ in [19].

Scaling is observed for the ratios $R = v_4\{\Psi_2\}/(v_2\{\Psi_2\})^2$ at different centralities shown in Fig.4. Experimental data plotted onto the obtained results are reduced by factor varying from 1.56 (10%-20%) to 1.38

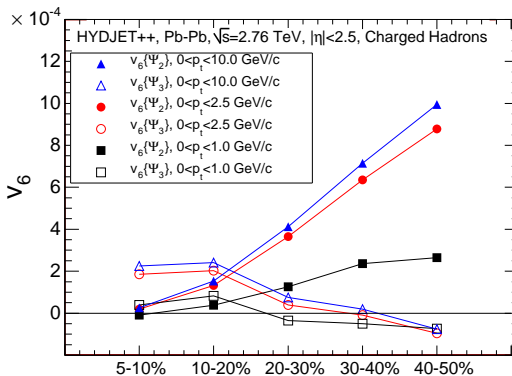


Fig. 3: Hexagonal flow $v_6\{\Psi_2\}$ (solid symbols) and $v_6\{\Psi_3\}$ (open symbols) of charged particles vs. centrality in Pb+Pb collisions at $\sqrt{s} = 2.76$ TeV simulated by HYDJET++ . The pseudorapidity interval is $|\eta| < 2.5$. Triangles, circles and squares indicate the flow of hadrons with transverse momenta below 10 GeV/c, 2.5 GeV/c and 1 GeV/c (squares), respectively.

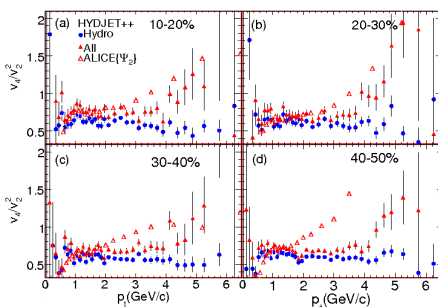


Fig. 4: Ratio $v_4/(v_2)^2$ in the Ψ_2 event plane as a function of transverse momentum for charged particles in HYDJET++ hydro (full circles) and hydro+jets (full triangles) calculations of Pb+Pb collisions at $\sqrt{s} = 2.76$ TeV at four different centralities. Data shown by open triangles are taken from [20].

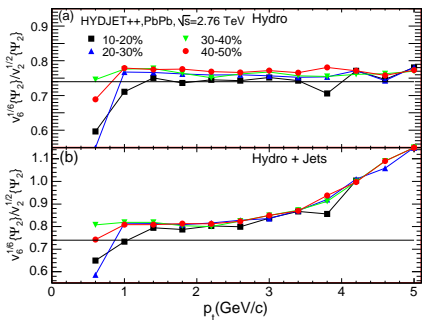


Fig. 5: Ratio $v_6^{1/6}/v_2^{1/2}$ as a function of p_T in the Ψ_2 event plane for charged particles, originated from (a) soft processes only and (b) both soft and hard processes, in HYDJET++ simulations of Pb+Pb collisions at $\sqrt{s} = 2.76$ TeV for four selected centralities. Solid lines in both plots show the prediction of ideal hydrodynamics for this ratio at high p_t , $v_6^{1/6}/v_2^{1/2} = (1/6)^{1/6} \approx 0.74$ (from [12]).

(40%-50%) [21,22]. For the directly produced particles in hydro part of the HYDJET++ the ratio R equals to 0.5. Feed-down from resonances increases it to 0.6, and jet contribution makes it as high as 0.7. Probably, the most important feature is the rise of R at $p_T \geq 2.5 \text{ GeV}/c$. Hydrodynamics provides almost flat signal, therefore this rise can be attributed to jet processes only. Similar scaling is obtained in the model for $v_6^{1/6}\{\Psi_2\}/v_2^{1/2}\{\Psi_2\}$ ratios [12], as displayed in Fig.5. In contrast, for the ratios $v_6^{1/6}\{\Psi_3\}/v_3^{1/3}\{\Psi_3\}$ the scaling is not observed [12]. These predictions can be easily checked experimentally. Again, jets increase the ratio of about 10% and cause the rise of the high- p_T tail at $p_T \geq 3 \text{ GeV}/c$.

4. Conclusions

The interplay of v_2 and v_3 is studied in almost ideal conditions. We demonstrate that significant part of the flow harmonics v_4, v_5, v_6 , etc. comes from the elliptic and triangular flows. Therefore, it is difficult to consider the higher harmonics as independent characteristics of the early phase of ultrarelativistic heavy ion collisions. To investigate the genuine flow harmonics related to higher-order eccentricities ε_n one has to study more central events, where at least the elliptic flow is weak. Scaling of the ratios $v_n^{1/n}\{\Psi_2\}/v_2^{1/2}\{\Psi_2\}$ is observed for even harmonics. Jets account for increase of these ratios of about 10-15% and formation of rising high- p_T tails. These phenomena deserve further investigations.

Acknowledgments

Fruitful discussions with Laszlo Csernai are gratefully acknowledged. This work was supported in parts by the Department of Physics, UiO, Russian Foundation for Basic Research under Grant No. 12-02-91505, Grant of the President of Russian Federation for Scientific School Supporting No. 3042.2014.2, and European Social Fund within the framework of realizing the project Support of Inter-sectoral Mobility and Quality Enhancement of Research Teams at Czech Technical University in Prague, CZ.1.07/2.3.00/30.0034.

1. W. Scheid, H. Muller, W. Greiner, Phys. Rev. Lett. **32** 741 (1974).
2. S. A. Voloshin and Y. Zhang, Z. Phys. **C70** 665 (1996).
3. A. M. Poskanzer and S. A. Voloshin, Phys. Rev. **C58** 1671 (1998).
4. B. Alver and G. Roland, Phys. Rev. **C81** 054905 (2010) [Erratum-ibid. **C82** 039903 (2010)].
5. B. H. Alver, C. Gombeaud, M. Luzum, J.-Y. Ollitrault, Phys. Rev. **C82** 034913 (2010).
6. G.-Y. Qin, H. Petersen, S. A. Bass, B. Müller, Phys. Rev. **C82** 064903 (2010).
7. F. G. Gardim, F. Grassi, M. Luzum, J.-Y. Ollitrault, Phys. Rev. **C85** 024908 (2012).
8. Z. Qiu and U. Heinz, Phys. Rev. **C84** 024911 (2011).
9. D. Teaney and L. Yan, Phys. Rev. **C86** 044908 (2012).
10. U. Heinz and R. Snellings, Annu. Rev. Nucl. Part. Sci. **64** 123 (2013).
11. L. V. Bravina *et al.*, Eur. Phys. J. **C74** 2807 (2014).
12. L. V. Bravina *et al.*, Phys. Rev. **C89** 024909 (2014).
13. I. P. Lokhtin *et al.*, Comput. Phys. Commun. **180** 779 (2009).
14. N. S. Amelin *et al.*, Phys. Rev. **C74** 064901 (2006); *ibid.* **C77** 014903 (2008).
15. I. P. Lokhtin and A. M. Snigirev, Eur. Phys. J. **C46** 211 (2006).
16. G. Torrieri *et al.*, Comput. Phys. Commun. **167** 229 (2005).
17. N. Borghini and J.-Y. Ollitrault, Phys. Lett. **B642** 227 (2006).
18. S. Chatrchyan, *et al.* (CMS Collaboration), Phys. Rev. **C87** 014902 (2013).
19. J. Jia *et al.* (ATLAS Collaboration), Nucl. Phys. **A910-911** 276 (2013).
20. B. Abelev *et al.* (ALICE Collaboration), Phys. Lett. **B719** 18 (2013).
21. M. Luzum, C. Gombeaud, J.-Y. Ollitrault, Phys. Rev. **C81** 054910 (2010).
22. L. Bravina, B. H. Buschbeck, M. Johansson, G. Eyyubova, E. Zabrodin, Phys. Rev. **C87** 034901 (2013).



Anisotropic flow generated by hard partons in medium

Boris Tomášik^{1,2} and Martin Schulc²

¹ *Univerzita Mateja Bela, Tajovského 40, 97401 Banská Bystrica, Slovakia*

² *Czech Technical University in Prague, FNSPE, Břehová 7, 11519 Praha 1, Czech Republic*
e-mail: boris.tomasik@umb.sk

Abstract

Hard partons which are produced copiously in nuclear collisions at the LHC, deposit most of their energy and momentum into the surrounding quark-gluon plasma. We show that this generates streams in the plasma and contributes importantly to flow anisotropies. With the help of event-by-event three-dimensional perfect hydrodynamic simulations we calculate the observable azimuthal anisotropies of hadronic distributions and show that the proposed mechanism is capable of generating non-negligible part of the observed signal. Hence, it must be taken into account in quantitative studies in which one tries to extract the values of viscosities from the comparison of simulated results with measured data.

1. Introduction

Expansion of matter excited in ultrarelativistic nuclear collisions provides access to its collective properties: Equation of State and transport coefficients. More detailed study of them is possible if one looks at azimuthal anisotropies of hadron distributions. They are caused by anisotropic expansion of the fireball (for reviews see e.g. [1,2]).

Indeed, the slope of a transverse-momentum hadron spectrum is influenced by transverse expansion through a Doppler blue-shift. If we

select particles with certain momentum there is a specific part of the expanding fireball which dominates the production of this momentum. Most naturally this would be that part of the fireball which co-moves with the hadrons within our focus. Emission of this momentum from other parts—i.e. those moving in other directions—is suppressed. Thus we have radiating source moving towards the detector. The blue-shift of the radiation is translated into enhanced production of higher p_t . Therefore the spectrum of an expanding source becomes flatter. The range of source velocities co-determines—together with the temperature—the flatness of the spectrum.

If the fireball expands with different velocities in different directions this is usually put into connection with inhomogeneities in the initial state determined by various kinds of fluctuations of energy deposition during the initial impact. By hydrodynamically propagating these inhomogeneities and comparing thus calculated hadron distributions with measured data one tries to determine the properties of matter which enter the evolution model.

One of the problems with this programme is that the initial conditions are only known from various model calculations. Moreover, any other mechanism which influences the flow anisotropies hinders the determination of transport coefficients and must be controlled in good quantitative studies.

We propose here another mechanism which clearly leads to anisotropy in the collective expansion of the fireball. It must be well understood quantitatively if further progress in determination of matter properties is desired.

2. Flow anisotropy from hard partons

In nuclear collisions at collider energies non-negligible part of the energy is initially released in the form of partons with high transverse momentum. At the LHC we have several pairs of partons with transverse momentum above a few GeV per event. Usually, one would refer to them as seeds of minijets and jets. In most cases all of their momentum and energy, however, is transferred into the surrounding quark-gluon-plasma

over some period of time. This creates streams in the bulk which lead to anisotropies in collective expansion.

It is quite conceivable that such a mechanism can lead to flow anisotropies which fluctuate from event to event. Below we will estimate the effect with the help of hydrodynamic simulation. *A priori* it is not clear, however, whether this mechanism is oriented fully randomly or whether it is correlated with the geometry of the collision and also contributes to event-averaged anisotropies.

The latter is the case. Let us first explain how the mechanism works. In a non-central collision the fireball is initially elongated in the direction perpendicular to the reaction plane (which is spanned by the beam direction and the impact parameter). If two dijets are produced and directed both along the reaction plane, they both contribute to the elliptic flow anisotropy, as pictured in Fig. 1 left. Their contribution is positive, be-

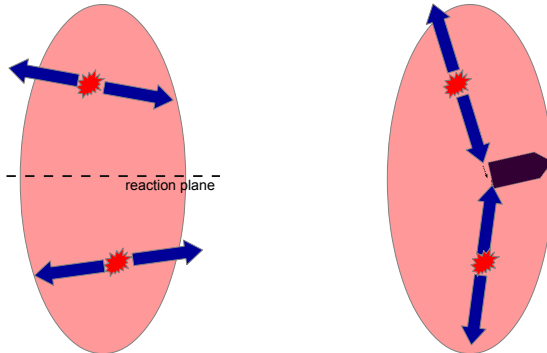


Fig. 1: Left: two dijets produced both almost parallel to the reaction plane. Blue arrows represent generated streams within quark-gluon plasma. Right: Two dijets produced in directions out of reaction plane.

cause due to larger pressure gradient stronger flow usually develops along the reaction plane even without any hard partons. If, however, two hard partons are directed out of the reaction plane, the chance is higher that two jet-induced streams will meet. Then they merge and continue in direction determined by energy and momentum conservation, see Fig. 1. Such a merger is more likely in this case since here the streams pass each

other along the narrow direction of the fireball and have less space to avoid the merger.

Note that via this mechanism isotropically produced hard partons couple to anisotropic shape of the fireball and generate anisotropy of the collective expansion.

An early study mimicking such a mechanism indicated that it will lead to elliptic flow, indeed [3].

3. Hydrodynamic simulations

In order to test our ideas in more realistic simulations we have constructed 3D hydrodynamic model [4]. We assumed perfect fluid. Simulations including viscosity are planned for the future. Note that it is important that the simulation is three-dimensional. Lower-dimensional models assume some kind of symmetry: boost-invariance in case of 2D and additional azimuthal symmetry in case of 1D. Inclusion of hard partons, however, breaks these symmetries and thus full simulation is needed.

Hard partons may deposit large amount of energy into a small volume and its evolution may lead to shock waves. Thus the model must exploit an algorithm capable of handling such a situation. We use SHASTA [5,6].

First we have shown that in a static medium hard partons induce streams which can merge if they come into contact [4].

Then we ran simulations of collisions of Pb nuclei at full LHC energy $\sqrt{s_{NN}} = 5.5$ TeV. Initial energy density profile is smooth and follows from the optical Glauber model. The initial positions of hard partons follow the distribution of binary nucleon-nucleon collisions. Energy and momentum deposition from hard partons into plasma is described as $\partial_\mu T^{\mu\nu} = J^\nu$ with the force term

$$J^\nu = - \sum_i \frac{1}{(2\pi\sigma_i^2)^{\frac{3}{2}}} \exp\left(-\frac{(\vec{x} - \vec{x}_{\text{jet},i})^2}{2\sigma_i^2}\right) \left(\frac{dE_i}{dt}, \frac{d\vec{P}_i}{dt}\right) \quad (1)$$

where the sum runs over all hard partons in the event. We did not study the microscopic mechanism of energy transfer from hard partons to

plasma and only assumed that it is localised within Gaussian distribution with $\sigma_i = 0.3$ fm.

The energy loss per unit of length scales with the entropy density

$$\frac{dE}{dt} \approx c \frac{dE}{dx}, \quad \frac{dE}{dx} = \frac{s}{s_0} \frac{dE}{dx} \Big|_0 \quad (2)$$

where s_0 corresponds to energy density of $20 \text{ GeV}/\text{fm}^3$ and $dE/dx|_0$ is a parameter of the simulation for which we tested a few values. Details of the model can be found in [7].

4. Results

Due to flow fluctuations flow anisotropies are generated even in most central collisions. They are observable if one does not average over many events. We first looked at the contribution of our mechanism to anisotropies in central collisions. To this end we simulated 100 central events with included hard partons and then ran THERMINATOR2 [8] five times in order to generate hadrons for each of the obtained freeze-out hypersurfaces.

In Fig. 2 we show 2nd and 3rd order anisotropy coefficients v_2 and v_3 . Results are compared to simulations with no hard partons which indeed show no anisotropies. We studied the dependence on the value of $dE/dx|_0$. Surprisingly results seem not to depend on the particular value of the energy loss. Note that the total amount of the energy deposited into plasma is the same in both cases. They differ by how fast this process runs. The reason may be that in most cases all energy is deposited from hard partons into plasma already at the beginning. We also measure the anisotropies in simulations where hard partons were replaced by hot spots, i.e. local depositions of additional energy density in the initial conditions. They are chosen in such a way that onto the smooth energy density profile the same amount of energy is added as the hard partons would deposit during the whole time. We see that the effect generating flow anisotropies is smaller than with hard partons where also momentum is deposited.

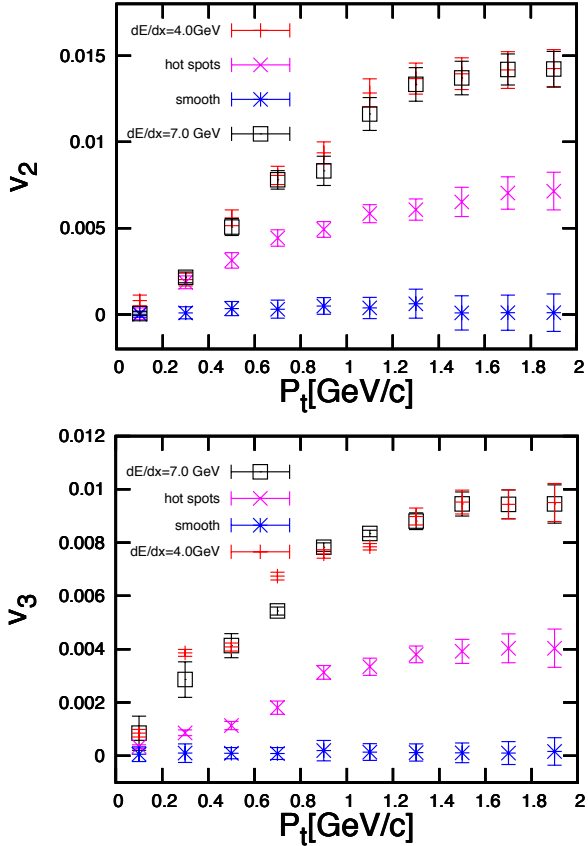


Fig. 2: Top: Second order anisotropy coefficient v_2 of hadronic distributions in ultra-central collisions. Lower data are from simulation with no fluctuations. Upper two sets of data are from simulations with hard partons with different values of $dE/dx|_0$. Crosses in between of these data sets show results from simulations with hot spots instead of hard partons. Bottom: same as top panel but for v_3 .

As a cross-check, we confirmed that no anisotropies of hadron spectra are generated from azimuthally symmetric fireball with smooth initial conditions and no fluctuations.

We also checked how this mechanism is aligned with the geometry in non-central collisions. To this end we simulated fireballs with impact parameter $b = 6.5$ fm and compared anisotropies in cases with or without

hard partons, see Fig. 3. Hard partons indeed enhance the elliptic flow;

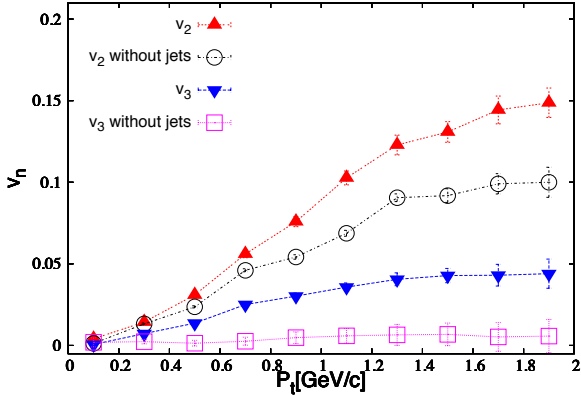


Fig. 3: Azimuthal anisotropy coefficients v_2 and v_3 from simulations of 30-40% centrality class (impact parameter $b = 6.5$ fm). Simulations with hard partons are compared to simulations with only smooth initial conditions and no hard partons (without jets).

this confirms the alignment with collision geometry thanks to merging of the streams. Triangular flow (v_3) is solely generated by hard partons. It is absent in non-central collisions with smooth initial conditions in accord with the symmetry constraints.

5. Conclusions

There are several studies similar to ours documented in the literature.

In [9] the authors study the response of expanding fireball to only one dijet. As we argued previously, this cannot lead to the alignment with the geometry since it is caused by merging of the induced streams.

Simulations in [10] are performed in 2D. We argued that using boost-invariance in this case may be inappropriate.

Finally, in [11,12] the authors only study the influence of hard partons on radial flow and did not touch elliptic flow anisotropies.

Our results show that the contribution to flow anisotropies from hard partons may be relevant in quantitative studies aimed at the determination of the transport coefficients. More precise studies will require

inclusion of three-dimensional viscous hydrodynamic model and other sources of fluctuations.

Acknowledgement This work was supported in parts by APVV-0050-11, VEGA 1/0457/12 (Slovakia) and MŠMT grant LG13031 (Czech Republic).

1. P. Romatschke, *Int. J. Mod. Phys. E* **19** 1 (2010).
2. C. Gale, S. Jeon, B. Schenke, *Int. J. Mod. Phys. A* **28** 1340011 (2013).
3. B. Tomášik and P. Lévai, *J. Phys. G* **38** 095101 (2011).
4. M. Schulc, B. Tomášik, *J. Phys. G* **40** 125104 (2013).
5. J. P. Boris, D. L. Book, *J. Comp. Phys.* **11** 38 (1973).
6. C. R. DeVore, *J. Comput. Phys.* **92** 142 (1991).
7. M. Schulc, B. Tomášik, *Phys. Rev. C* **90** 064910 (2014).
8. M. Chojnacki, A. Kisiel, W. Florkowski and W. Broniowski, *Comput. Phys. Commun.* **183** 746 (2012).
9. Y. Tachibana, T. Hirano, *Phys. Rev. C* **90** 021902 (2014) .
10. R. P. G. Andrade, J. Noronha and G. S. Denicol, *Phys. Rev. C* **90** 024914 (2014).
11. S. Floerchinger and K. C. Zapp, *Eur. Phys. J. C* **74** 3189 (2014).
12. K. C. Zapp and S. Floerchinger, *Nucl. Phys. A***931** 388 (2014).

Differential HBT and correlation functions for the exact hydro model

L.P. Csernai, S. Velle and D.J. Wang

¹*Department of Physics and Technology, University of Bergen,
Allegaten 55, 5007 Bergen, Norway*

Abstract

Peripheral heavy ion reactions at ultra relativistic energies have large angular momentum that can be studied via two particle correlations using the Differential Hanbury Brown and Twiss method. We analyze the possibilities and sensitivity of the method in a rotating system. We also study an exact rotating and expanding solution of the fluid dynamical model of heavy ion reactions

1. Introduction

Collective flow is one of the most dominant observable features in heavy ion reactions up to the highest available energies, and its global symmetries as well as its fluctuations are extensively studied. Especially at the highest energies for peripheral reaction the angular momentum of the initial state is substantial, which leads to observable rotation according to fluid dynamical estimates [1]. Furthermore the low viscosity quark-gluon fluid may lead to initial turbulent instabilities, like the Kelvin Helmholtz Instability (KHI), according to numerical fluid dynamical estimates [2], which is also confirmed in a simplified analytic model [3]. These turbulent phenomena further increase the rotation of the system, which also leads to a large vorticity and circulation of the participant zone one order of magnitude larger than from random fluctuations in the transverse plane [4–6].

The two particle correlation method is used to determine the space-time size of the system emitting the observed particles, thus providing valuable information on the exploding and expanding system at the freeze out stage of a heavy ion collision. This method is based on the Hanbury Brown and Twiss (HBT) method, originally used for the determination of the size of distant stars [7, 8].

The Differential Hanbury Brown and Twiss (DHBT) method has been introduced in [9]. The method has been applied to a high resolution Particle in Cell Relativistic (PICR) fluid dynamical model [10]. We also look at the values from the exact hydro model [11, 12] and determine the effect rotation has on the correlation functions (CF) for detectors at different positions.

2. The two particle correlation

The pion correlation function is defined as the inclusive two-particle distribution divided by the product of the inclusive one-particle distributions, such that [13]:

$$C(p_1, p_2) = \frac{P_2(p_1, p_2)}{P_1(p_1)P_1(p_2)}, \quad (1)$$

where p_1 and p_2 are the 4-momenta of the pions and k and q are the average and relative momentum respectively.

We use a method for moving sources presented in Ref. [15]. In the formulae the $\hbar = 1$ convention is used and k and q are considered as the wavenumber vectors. The correlation function is:

$$C(k, q) = 1 + \frac{R(k, q)}{|\int d^4x S(x, k)|^2}, \quad (2)$$

where

$$R(k, q) = \int d^4x_1 d^4x_2 \cos[q(x_1 - x_2)] S(x_1, k + q/2) S(x_2, k - q/2). \quad (3)$$

Here $R(k, q)$ can be calculated [15] via the function and we obtain the $R(k, q)$ function as

$$R(k, q) = \text{Re}[J(k, q) J(k, -q)] \quad (4)$$

The corresponding $J(k, q)$ function will become

$$J(k, q) = \int d^4x S(x, k) \exp \left[-\frac{q \cdot u(x)}{2T(x)} \right] \exp(iqx) . \quad (5)$$

For the phase space distribution we frequently use the Jüttner (relativistic Boltzmann) distribution, in terms of the local invariant scalar particle density the Jüttner distribution is [16]

$$f^J(x, p) = \frac{n(x)}{C_n} \exp \left(-\frac{p^\mu u_\mu(x)}{T(x)} \right) , \quad (6)$$

where $C_n = 4\pi m^2 T K_2(m/T)$. We assume a spatial distribution:

$$G(x) = \gamma n(x) = \gamma n_s \exp \left(-\frac{x^2 + y^2 + z^2}{2R^2} \right) . \quad (7)$$

Here n_s is the average density of the Gaussian source, s , (or fluid cell) of mean radius R .

2.1. Asymmetric Sources

We have seen in few source model examples [9] that a highly symmetric source may result in correlation functions that are sensitive to rotation, however, these results were not sensitive to the direction of the rotation, which seems to be unrealistic. We saw that this result is a consequence of the assumption that both of the members of a symmetric pair contribute equally to the correlation function even if one is at the side of the system facing the detector and the other is on the opposite side. The expansion velocities are also opposite at the opposite sides. The dense and hot nuclear matter or the Quark-gluon Plasma are strongly interacting, and for the most of the observed particle types the detection of a particle from the side of the system, – which is not facing the detector but points to the opposite direction, – is significantly less probable. The reason is partly in the diverging velocities during the expansion and partly to the lower emission probability from earlier (deeper) layers of the source from the external edge of the timelike (or spacelike) FO layer.

For the study of realistic systems where the emission is dominated by the side of the system, which is facing the detector, we cannot use the

assumption of the symmetry among pairs or groups of the sources from opposite sides of the system. Even if the FO layer has a time-like normal direction, $\hat{\sigma}^\mu$ the $(k^\mu \hat{\sigma}^\mu)$ factor yields a substantial emission difference between the opposite sides of the system.

3. The DHBT method and fluid dynamical results

The correlation function, $C(k, q)$ is always measured in a given direction of the detector, \vec{k} . Obviously only those particles can reach the detector, which satisfy $k^\mu \hat{\sigma}_\mu > 0$. Thus in the calculation of $C(k, q)$ (see Fig. 1) for a given \vec{k} -direction we can exclude the parts of the freeze out layer where $k^\mu \hat{\sigma}_\mu < 0$ (see Eq. (10) of Ref. [17] or Ref. [19]). For time-like FO a simplest approximation for the emission possibility is $P_{esc}(x) \propto k^\mu u_\mu(x)$ [18].

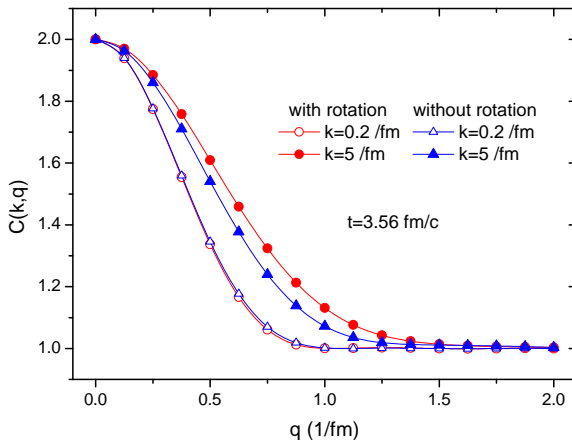


Fig. 1: (color online) The dependence of the standard correlation function in the \vec{k}_+ direction from the collective flow, at the final time.

Based on the few source model results the Differential HBT method [9] was introduced by evaluating the difference of two correlation functions measured at two symmetric angles, forward and backward shifted in the reaction plane in the participant c.m. frame by the same angle, i.e. at $\eta = \pm \text{const.}$, so that

$$\Delta C(k, q) \equiv C(k_+, q_{out}) - C(k_-, q_{out}). \quad (8)$$

The sensitivity of the standard correlation function on the fluid cell velocities decreases with decreasing distances among the cells. So, with a large number of densely placed fluid cells where all fluid cells contribute equally to the correlation function, the sensitivity on the flow velocity becomes negligibly weak.

Thus, the emission probability from different ST regions of the system is essential in the evaluation. This emission asymmetry due to the local flow velocity occurs also when the FO surface or layer is isochronous or if it happens at constant proper time.

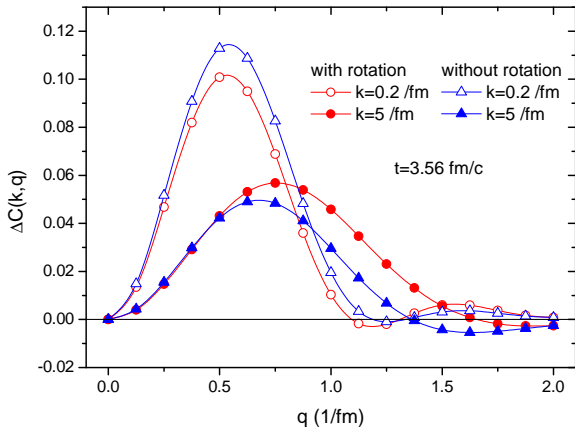


Fig. 2: (color online) The differential correlation function $\Delta C(k, q)$ at the final time with and without rotation.

We studied the fluid dynamical patterns of the calculations published in Ref. [2], where the appearance of the KHI is discussed under different conditions. We chose the configuration, where both the rotation [1], and **the KHI occurred**, at $b = 0.7b_{max}$ with high cell resolution and low numerical viscosity at LHC energies, where the angular momentum is large, $L \approx 10^6 \hbar$ [14]. Fig. 2 shows the DHBT for the FD model.

4. Differential HBT for exact hydro model.

The density for the exact hydro model [12] is given by

$$N(r_\rho, r_y) = N_B \frac{C_n}{V} \exp(-r_\rho^2/R^2) \exp(-r_y^2/Y^2) \quad (9)$$

or using the scalar variables in the out (ρ , R), side (φ , Θ), long (y , Y) directions

$$N(s_\rho, s_y) = N_B \frac{C_n}{V} \exp(-s_\rho/2) \exp(-s_y/2), \quad (10)$$

where $s_\rho = r_\rho^2/R^2$ and $s_y = r_y^2/Y^2$.

We use the finite size cylindrical shape source as described in eq. (10) of [12]

$$\int_0^\infty \int_{-\infty}^\infty \int_0^{2\pi} r_\rho dr_\rho dr_y d\varphi = \frac{\pi R^2 Y}{\sqrt{2}} \int_0^1 \int_0^1 \int_0^{2\pi} \frac{ds_y ds_\rho d\varphi}{\sqrt{s_y}} \quad (11)$$

and the integral $J(k, q)$ for this model with the scaling variables will be

$$J(k, q) \propto \int_0^1 \int_0^1 \int_0^{2\pi} w_s \gamma_s \left(k_0 + \vec{k} \cdot \vec{v}_s \right) \times \exp \left[-\frac{\gamma_s}{T_s} \left((k_0 + q_0/2) - (\vec{k} + \vec{q}/2) \cdot \vec{v}_s \right) \right] \exp(i\vec{q} \cdot \vec{x}) e^{s_\rho/2} e^{s_y/2} \frac{ds_y ds_\rho d\varphi}{\sqrt{(s_y)}} \quad (12)$$

where $k_0 = \sqrt{\frac{2m_\pi}{\hbar c} + k^2}$ and $q_0 = \frac{\vec{k} \cdot \vec{q}}{k_0}$, w_s is a weight function, $w_s \propto k^\mu \sigma_\mu$, and the temperature profile is flat with a value of 250 MeV.

We have the single particle distribution integral

$$\int d^4x S(x, k) \propto \int w_s \gamma_s \left(k_0 + \vec{k} \cdot \vec{v}_s \right) \times \exp \left[-\frac{\gamma_s}{T_s} \left(k_0 - \vec{k} \cdot \vec{v}_s \right) \right] e^{s_\rho/2} e^{s_y/2} \frac{ds_y ds_\rho d\varphi}{\sqrt{(s_y)}}, \quad (13)$$

and the correlation function is eq. 2 so the constants outside the integrals will cancel.

The velocity consists of a radial expansion in the out direction, a longitudinal expansion in the long direction and also a angular velocity,

where the rotation is in the reaction plane. The velocity in the x , y , z directions where x is the direction of the impact parameter, y is the longitudinal (rotation) axis and z is the (beam) collision axis

$$\vec{v}_s = \left(\dot{R}\sqrt{s_\rho} \sin(\varphi) + R\omega\sqrt{s_\rho} \cos(\varphi), \right. \\ \left. \dot{Y}\sqrt{s_y}, \dot{R}\sqrt{s_\rho} \cos(\varphi) - R\omega\sqrt{s_\rho} \sin(\varphi) \right). \quad (14)$$

T a b l e 1: Time dependence of some characteristic parameters of the fluid dynamical calculation presented in ref. [12].

t	Y	\dot{Y}	ω	R	\dot{R}	φ
(fm/c)	(fm)	(c)	(c/fm)	(fm)	(c)	(Rad)
0.	4.000	0.300	0.150	2.500	0.250	0.000
3.	5.258	0.503	0.059	3.970	0.646	0.307
8.	8.049	0.591	0.016	7.629	0.779	0.467

Together with the equations above, eq. 8 and the values from the table we can calculate the DCF, see Fig. 3.

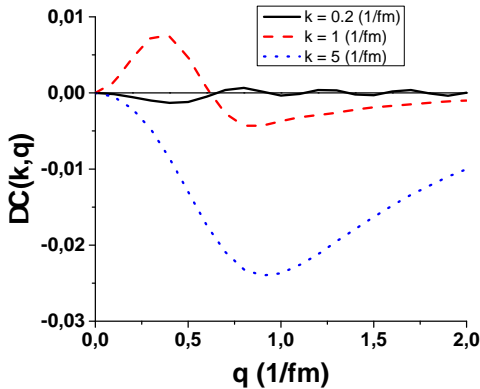


Fig. 3: Differential Correlation Function for the exact hydro model with $R = 7.629$ fm, $\dot{R} = 0.779$ c, $Y = 8.049$ fm, $\dot{Y} = 0.591$ fm, $\omega = 0.016$ c/fm, $t = 8.0$ fm/c. The solid black line is for $k = 0.2$ fm $^{-1}$, the dashed red line is for $k = 1$ fm $^{-1}$ and the dotted blue line is for $k = 5$ fm $^{-1}$. The detector is at $\vec{k} = (\sqrt{\frac{7}{8}}k, 0, \frac{1}{2\sqrt{2}}k)$

5. Conclusion

It is important to take into account that the particles reaching the detector cannot reach it with equal probability from the near side and the far side of the emitting object. With this fact considered we could obtain correlation functions, which reflect the properties and also the direction of the flow.

These analytic results provide deeper insight to the methods of studying rotation in highly energetic systems. Several aspects of the sensitivity and observability can be discussed based on these analytic results which are not easily accessible in a fully realistic and complex reaction model.

The model calculations show that the Differential HBT method can give a good measure of rotation in this exact hydro model. The differential correlation function is dependent on shape, temperature, radial velocity and angular velocity. If we eliminate rotation or the radial expansion the DCF vanishes in the model.

1. L.P. Csernai, V.K. Magas, H. Stöcker, and D.D. Strottman, Phys. Rev. C **84**, 024914 (2011).
2. L.P. Csernai, D.D. Strottman and Cs. Anderlik, Phys. Rev. C **85**, 054901 (2012).
3. D.J. Wang, Z. Néda, and L.P. Csernai Phys. Rev. C **87**, 024908 (2013).
4. L.P. Csernai, V.K. Magas, and D.J. Wang, Phys. Rev. C **87**, 034906 (2013).
5. S. Floerchinger and U. A. Wiedemann, Journal of High Energy Physics, JHEP **11**, 100 (2011);
6. S. Floerchinger and U. A. Wiedemann, J. Phys. G: Nucl. Part. Phys. **38**, 124171 (2011).
7. R. Hanbury Brown and R.Q. Twiss, Phil. Mag. **45**, 663 (1954);
8. R. Hanbury Brown and R.Q. Twiss, Nature, **178**, 1046 (1956).
9. L.P. Csernai, S. Velle Int. J. Mod. Phys. E **23**, 1450043 (2014).
10. L. P. Csernai, S. Velle, and D. J. Wang , Phys. Rev. C **89**, 034916 (2014);
11. T. Csörgő and M.I. Nagy, Phys. Rev. C **89**, 044901 (2014).
12. L. P. Csernai, D. J. Wang, and T. Csörgő Phys. Rev. C **90**, 024901 (2014).
13. W. Florkowski: *Phenomenology of Ultra-relativistic heavy-Ion Collisions*, World Scientific Publishing Co., Singapore (2010).
14. V. Vovchenko, D. Anichishkin, and L.P. Csernai, Phys. Rev. C **88**, 014901 (2013).

15. A.N. Makhlin, Yu.M. Sinyukov, *Z. Phys. C* **39**, 69-73 (1988).
16. F. Jüttner, *Ann. Phys. und Chemie*, **34** (1911) 856.
17. Yu.M. Sinyukov, *Nucl. Phys. A* **498**, 151c (1989).
18. T. Csörgő, *Heavy Ion Phys.* **15**, 1-80, (2002); arXiv: hep-ph/0001233v3.
19. K.A. Bugaev, *Nucl. Phys. A* **606**, 559 (1996).

Flow Vorticity in Peripheral Heavy Ion Collisions

D. J. Wang¹ and L. P. Csernai¹

April 13, 2015

¹*Department of Physics and Technology, University of Bergen,
Allegaten 55, 5007 Bergen, Norway*

Abstract

The vorticity development is studied in the reaction plane of peripheral relativistic heavy ion reactions, at high energies as well as the energies just above the threshold of transition to Quark Gluon Plasma (QGP). We use an initial state with substantial angular momentum and it is maintained in the development of the fluid dynamics. The expanding system rotates and Kelvin Helmholtz Instability (KHI) would happen, which can lead to significant initial vorticity and circulation. In low viscosity QGP this vorticity remains still significant at the time of freeze out of the system, although it is damped by the explosive expansion and the dissipation. In the reaction plane the vorticity arises from the initial angular momentum, and it is stronger than in the transverse plane where vorticity is caused only by random fluctuations.

1. Introduction

Fluid dynamical processes are studied in heavy ion collisions for a long time [1–3], and their use is becoming more dominant and widening at the same time [4] in recent years. With the increase of collision energy, the hadronic matter may transit into strongly interacting Quark-gluon plasma (QGP) state [5], which has raised many interesting questions about the physics of ultra dense hot matter produced in high energy heavy ion collisions. Many transport and hydrodynamic models [6] are popular in studying the development of the viscous QGP and its properties. In peripheral heavy ion reactions the tilted initial state of the

collision [7] has big shear flow velocity due to large initial angular momentum which may lead to rotation [8] and Kelvin Helmholtz Instability (KHI) [9] for low viscosity QGP [10, 11]. The angular momentum is assumed to have significant effects on the longitudinal flow velocity and on its distribution in the transverse plane, thus it leads to vorticity and polarization [12].

Fig. 1 shows the 3-dimensional view of peripheral heavy ion collisions where two colliding nuclei are Lorentz contracted and inter penetrate each other. The participant cylinder in the middle is divided into streaks with different velocity, which are slowed down by the large string rope tension. This process takes about 3-5 fm/c for heavy nuclei depending on the impact parameter, later on local equilibration is reached and the fluid dynamical evolution starts. Then we study the vorticity of flow by a Computational Fluid Dynamical (CFD) model where the space is divided into grid cells and lagrangian Particles in Cells Relativistically (PICR) are considered. This work may provide an insight into the possibilities of using vorticity to precision studies of the transport properties of QGP.

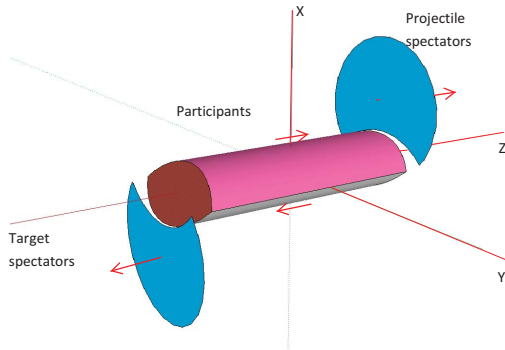


Fig. 1: The 3-dimensional view of peripheral heavy ion collision just after a few fm/c time after the impact [13]. The middle red cylinder represents the participants, which have an almond shape profile and tilted end surfaces. The two blue shapes stand for spectators moving to opposite directions.

T a b l e 1: Average weighted vorticity (c/fm) calculated for Pb+Pb reactions at $\sqrt{s_{NN}} = 2.76$ TeV, different impact parameters and cell sizes.

Time (fm/c)	$b/b_{max} = 0.5, dx=0.585\text{fm}$		$b/b_{max} = 0.7, dx=0.4375\text{fm}$	
	Relativistic	Classical	Relativistic	Classical
Reaction plane				
0.17	0.02415	0.05839	0.11846	0.14343
3.56	0.01677	0.01622	0.07937	0.04845
6.94	0.01295	0.00606	0.05116	0.01555
All layers				
0.17	0.07241	0.09442	0.19004	0.1971
3.56	0.05242	0.03086	0.10685	0.0538
6.94	0.0344	0.01185	0.05881	0.0159

2. The vorticity

Classically in 3-dimensional space the vorticity is defined as:

$$\omega = \frac{1}{2} \nabla \times \mathbf{v} , \quad (1)$$

where the factor 1/2 is introduced for symmetrization [13]. The flow circulation can be related to vorticity and it is defined as

$$\Gamma = \oint_C \mathbf{v} dl = \int 2\omega dS ,$$

where S is the closed surface element surrounded by the curve C .

In relativistic case the vorticity is defined as

$$\omega_{\mu\nu} = \frac{1}{2} (\partial_\nu u_\mu - \partial_\mu u_\nu) , \quad (2)$$

where $\partial_\nu = (\partial_0, \partial_x, \partial_y, \partial_z)$ and $u_\mu = \gamma(1, -v_x, -v_y, -v_z)$. The unit of vorticity is c/fm. In our PICR hydrodynamical model the fluid cells are in 3 dimensions and we calculate the vorticity in the y direction for all $[x, z]$ layers:

$$\omega_{y(Cl.)} = \frac{1}{2} (\partial_z v_x - \partial_x v_z) , \quad (3)$$

$$\omega_{y(Re.)} = \frac{1}{2} (\partial_z \gamma v_x - \partial_x \gamma v_z) , \quad (4)$$

where "Cl."denotes classical case and "Re." denotes the relativistic case. The latter one takes into account the role of γ factor. The reaction plane corresponds to the $y = 0$ layer. After collision the system expands and it becomes highly non-homogeneous, the number of cells filled with particles is increasing, and the energy per cell is decreasing due to energy conservation. The vorticity is weighted by the energy density since the cells with higher energy density should contribute more to it.

We studied the average vorticity for Pb+Pb collisions with different impact parameters ($b = 0.7$ and $0.5 b_{max}$), see table 1. For more peripheral collisions ($b = 0.7 b_{max}$), the average velocity is larger since the initial condition is favoring more the KHI. For more central collision ($b = 0.5 b_{max}$) the average vorticity is smaller. The time developments of the vorticity are also shown in table 1, as we can see the vorticity decreases rapidly due to the system expansion and dissipation. The configurations with smaller cell size, which corresponds to smaller viscosity have less dissipation.

Then we show the vorticity distribution in fig. 2. The center of mass energies are respectively 2.76 TeV for LHC, 200 GeV for RHIC, 9.3 GeV for NICA and 8 GeV for FAIR. More results of the flow vorticity are shown in [13,14]. The peak vorticity calculated in the reaction plane is bigger than the one obtained in the transverse, [x-y], plane [15], which only has a maximum of 0.2 c/fm. As we can see in fig.2(a) and (b), the vorticity has a peak around 0.45 c/fm even for the reactions with a few GeV collision energy. This is because the vorticity calculated in the reaction plane is induced by the large initial angular momentum for high energy peripheral collisions while in the transverse plane it is induced only by random fluctuations.

We studied the lower energy collisions in order to study the possibility of vorticity and circulation in dense plasma at lower temperatures. For lower energy collision the system has less possibility to form QGP state. The large hadronic pressure will lead to earlier and more rapid expansion, thus the rotational energy will be reduced faster and converted into more explosive expansion. In our study we find that although the magnitude is smaller than the one obtained for higher energy, the vorticity still remains significant, see fig. 2 (c) and (d).

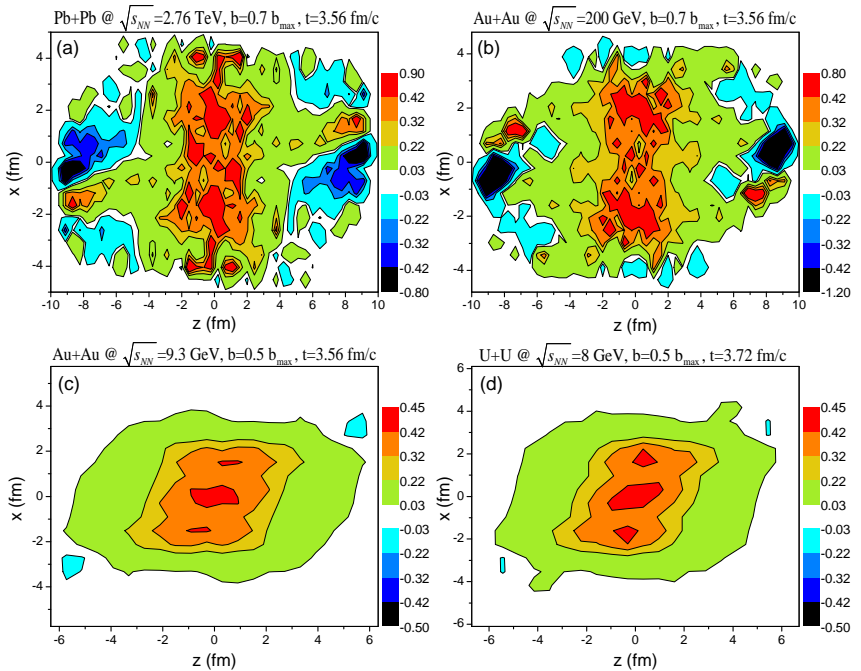


Fig. 2: (color online) The weighted vorticity distribution calculated in the reaction $[x-z]$ plane. The top two figures are calculated relativistically for high energy collisions and the bottom figures are calculated classically for energies just above the transition to quark-gluon plasma. The cell size $dx = dy = dz$ are respectively 0.4375 fm (a), 0.4295 fm (b), 0.575 fm (c) and 0.61 fm (d).

As discussed above we predict a substantial average vorticity and peak vorticity. It is possible to observe the consequences of this rotation and its sensitivity to turbulent configurations.

3. Thermal Vorticity

Similar with the vorticity calculation in Eq. (2), the thermal vorticity is defined as

$$\varpi^{\mu\nu} = \frac{1}{2}(\partial^\nu \beta^\mu - \partial^\mu \beta^\nu). \quad (5)$$

where β is the inverse temperature 4-velocity field:

$$\beta_\mu(x) = \frac{u_\mu(x)}{T}. \quad (6)$$

In the following the β field is multiplied by \hbar thus the thermal vorticity is dimensionless. We introduced the weighting factor the same way as done for normal vorticity since at late stages the energy density or the net baryon density tend to zero in the middle, which domain then should not be taken into account.

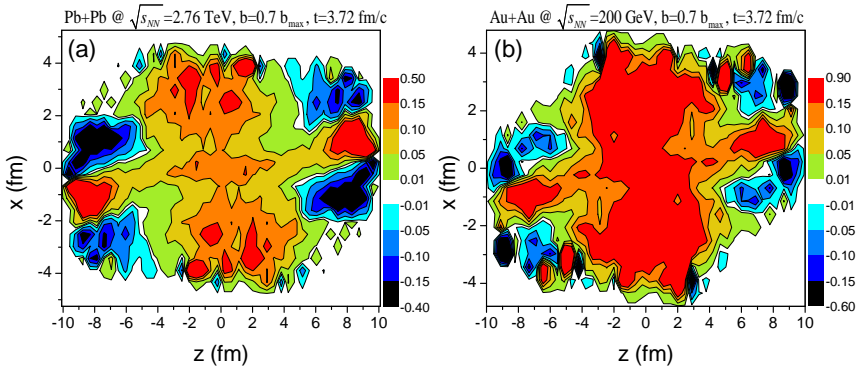


Fig. 3: (color online) The energy density weighted thermal vorticity distribution calculated in the reaction $[x-z]$ plane for relativistic high energy collisions. The cell sizes are the same as in fig. 2 (a) and (b).

The thermal vorticity can be used to evaluate polarization because the spin-orbit interaction aligns the spins and the orbital momentum, while the random thermal motion works against this alignment. As shown in Ref. [16] by assuming weakly interacting particles, the polarization formula turned out to be proportional to the thermal vorticity, where the local spin degrees of freedom and its equipartition with rotation are assumed. The polarization can be used to detect the rotation of the expanding matter [17] thus it is necessary to evaluate the thermal vorticity.

Fig. 3 shows the thermal vorticity distribution calculated for Pb+Pb collisions at LHC energy and for Au+Au collisions at RHIC energy. As one can see the central region is mainly positive, while the forward

Table 2: Averaged weighted relativistic thermal vorticity calculated for the Reaction Plane for LHC and RHIC energies.

Pb+Pb @ 2.76 TeV			Au+Au @ 200 GeV		
t	$\langle T \rangle$	$\langle \Omega_{zx} \rangle$	t	$\langle T \rangle$	$\langle \Omega_{zx} \rangle$
(fm/c)	(MeV)	(1)	(fm/c)	(MeV)	(1)
3.72	379	0.0301	1.19	285	0.0976
5.59	299	0.0237	1.86	261	0.0915
7.62	246	0.0172	2.54	237	0.0851
11.34	201	0.0077	3.72	204	0.0664
15.24	186	0.0027	4.74	183	0.0453

and backward peripheral regions have small negative vorticities. In the previous section we saw that vorticity is larger for higher energies while for thermal vorticity this is not true. It is smaller for LHC energy when we compare it with the RHIC energy. One can also see the difference of the maxima: 0.9 for RHIC and 0.5 for LHC.

In table 2 we show the average thermal vorticity as the function of time for both LHC and RHIC energies. The average thermal vorticity is smaller for LHC energy when we compare it with the ones calculated at RHIC energy and also with the normal vorticity calculated for the same LHC energy collisions (see table 1). This phenomenon is reasonable since at ultra-relativistic energies the velocities approach the speed of light, which means that the initial state velocity distributions are essentially identical. At the same time the initial energy density is much higher at LHC, thus the angular momentum and the initial temperature are also higher. As a consequence the thermal vorticity is smaller since the temperature is in the denominator. On the other hand the final, freeze out temperatures should not be too different, although at higher expansion speed the freeze out temperature is also expected to be higher.

4. Summary

The flow vorticity and thermal vorticity are studied in peripheral heavy ion collisions. The vorticity is significant for peripheral collisions and it decreases with time due to expansion and dissipation of the system.

The thermal vorticity is not proportional to the collision energy since the temperature plays a counter-effect to the thermal velocity field. Based on these vorticity studies we can use the polarization to detect the collective properties of the QGP, such as rotation and the KHI.

1. H. Stöcker, L.P. Csernai, G. Graebner, G. Buchwald, H. Kruse, R.Y. Cusson, J.A. Maruhn, and W. Greiner, *Phys. Rev. C* **25**, 1873 (1982).
2. L.P. Csernai, and J.I. Kapusta, *Phys. Rep.* **131**, 223 (1986).
3. H. Stöcker, and W. Greiner, *Phys. Rep.* **137**, 277 (1986).
4. H. Stöcker, *Nucl. Phys. A* **750**, 121 (2005).
5. M. Gyulassy and L. McLerran, *Nucl. Phys. A* **750**, 30 (2005).
6. K. Dusling and D. Teaney, *Phys. Rev. C* **77**, 034905 (2008); D. Molnar and P. Huovinen, *J. Phys. G* **35**, 104125 (2008).
7. V.K. Magas, L.P. Csernai, and D.D. Strottman, *Phys. Rev. C* **64**, 014901 (2001);
8. L.P. Csernai, V.K. Magas, H. Stöcker, and D.D. Strottman, *Phys. Rev. C* **84**, 024914 (2011).
9. L.P. Csernai, D.D. Strottman and Cs. Anderlik, *Phys. Rev. C* **85**, 054901 (2012).
10. P.K. Kovtun, D.T. Son and A.O. Starinets, *Phys. Rev. Lett.* **94**, 111601 (2005).
11. L.P. Csernai, J.I. Kapusta and L.D. McLerran, *Phys. Rev. Lett.* **97**, 152303 (2006).
12. F. Becattini, F. Piccinini and J. Rizzo, *Phys. Rev. C* **77**, 024906 (2008).
13. L.P. Csernai, V.K. Magas and D.J. Wang, *Phys. Rev. C* **87**, 034906 (2013).
14. L.P. Csernai, D.J. Wang, M. Bleicher and H. Stöcker, *Phys. Rev. C* **90**, 021904 (R) (2014).
15. S. Floerchinger and U.A. Wiedemann, *Journal of High Energy Physics*, doi:10.1007/JHEP **11**, 100 (2011); *J. Phys. G: Nucl. Part. Phys.* **38**, 124171 (2011).
16. F. Becattini, V. Chandra, L. Del Zanna and E. Grossi, *Annals of Physics* **338**, 32-49 (2013).
17. F. Becattini, L.P. Csernai and D.J. Wang, *Phys. Rev. C* **88**, 034905 (2013).

Recent results from the UrQMD hybrid model for heavy ion collisions

Marcus Bleicher, Stephan Endres, Jan Steinheimer,
Hendrik van Hees

*Frankfurt Institute for Advanced Studies (FIAS), Ruth-Moufang-Strasse
1, 60438 Frankfurt am Main, Germany
Institut für Theoretische Physik, Johann-Wolfgang-Goethe-Universität,
Max-von-Laue-Strasse 1, 60438 Frankfurt am Main, Germany*

Abstract

These proceedings present recent results from transport-hydrodynamics-hybrid models for heavy ion collisions at relativistic energies. The main focus is on the absorption of (anti-)protons in the hadronic afterburner stage of the reaction, di-lepton production at SPS and heavy quark dynamics.

1. Introduction

A major theme in today's high energy heavy ion physics is to explore the phases of Quantum Chromodynamics (QCD) at very high densities and temperatures. To connect ab-initio information on the properties of QCD-matter, e.g., the Equation of State (EoS) or transport coefficients like the viscosities with experimentally observable quantities one has to rely on transport approaches that describe the time evolution of the hot and dense matter created until the system has ceased to interact. Transport models and hydrodynamic approaches have a long tradition in providing this link. Unfortunately, the areas of application of both approaches seems mutually exclusive: Boltzmann equation based transport simulations are well suited for the less dense stages of the reaction

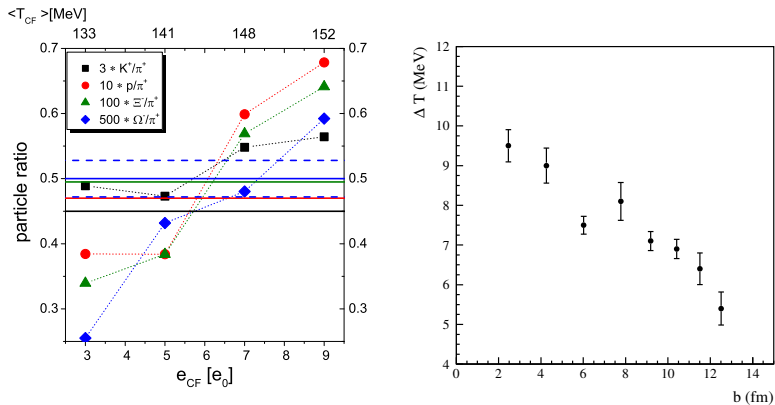


Fig. 1: Left: Modification of the final particle ratios as a function of the transition energy density ϵ_{CF} for the Cooper-Frye prescription in Pb+Pb collisions at $\sqrt{s_{NN}} = 2.76$ TeV [13]. Right: Corrected temperature of the freeze-out points on the phase diagram [15, 16].

or for lower energies, while hydrodynamic simulations are only justified during the most dense stages of the reaction's evolution or at very high collision energies.

2. Model description

For the present studies we use the UrQMD model v3.3 in hybrid mode [1–3]. This model couples the fluctuating initial state [4] generated event-by-event by the hadron and string dynamics from UrQMD to an ideal hydrodynamic evolution. For the evolution of the hydrodynamic part different equations of state can be applied, including a hadron gas EoS and a chiral EoS with a transition to a quark-gluon plasma. At the end of the hydrodynamic evolution, defined by a transition energy density, the hydrodynamic cells are converted to particles with a Cooper-Frye prescription [5], and the decoupling stage is handled by the UrQMD hadronic cascade [6]. For similar approaches by other groups we refer to [7–12] and references therein.

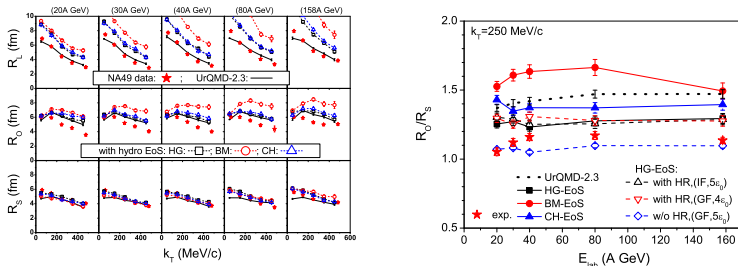


Fig. 2: Left: HBT radii for different beam energies as a function of the transverse momentum of the pion pair for different equations of state [17]. Right: Ratios of the out to side radii as function of beam energy and for different equations of state [17].

3. Matter and Antimatter

The effect of the hadronic afterburner can be seen directly in the yields of the protons and anti-protons in nuclear collisions at the LHC. Fig.1 (left) shows the modifications of the particle yields due to the hadronic corona as a function of the energy density at which the Cooper-Frye particlization is applied. One observes that for realistic transition energy densities around $\epsilon_{CF} = 5\epsilon_0$ the proton and anti-proton yields are reduced by approximately 50% in line with the observed values at the LHC [13]. A similar conclusion is also reached if the back reaction $5\pi \rightarrow p\bar{p}$ is included [14]. The systematic error, if the back reaction is neglected is on the order of 10% [14]. Fig. 1 (right) shows the temperatures extracted from chemical fits for different centralities in Pb+Pb reactions at $\sqrt{s_{NN}} = 2.76$ TeV. The temperature differences ΔT are obtained from the temperature differences between uncorrected fits and ‘corrected’ fits (i.e., corrected for baryon absorption in the hadronic corona as given by UrQMD) to the model data [15, 16].

4. Hanbury-Brown–Twiss Correlations

Let us next explore the effect of different equations of state. One expects that a phase transition to a quark-gluon plasma (and back to the hadron gas) should result in a delay of the expansion of the system depending on

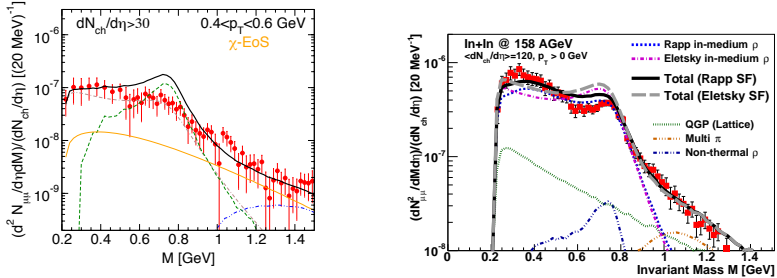


Fig. 3: Left: Di-muon spectrum for In+In collisions at 160 AGeV from hybrid-model simulations [18] in comparison to NA60 data [19]. Right: Di-muon spectrum for In+In collisions at 160 AGeV from coarse grained simulations in comparison to NA60 data [19]. Calculations with the Rapp-Wambach and Eletsky spectral functions are compared [24].

the magnitude of the latent heat. To explore this effect we compare hybrid simulations for different equations of state using Hanbury-Brown-Twiss (HBT) correlations [17]. Fig. 2 (left) provides a comparison of various equations of state (hadron gas EoS, chiral EoS, bag model EoS, and a pure UrQMD cascade simulation). One observes that the pure UrQMD simulation, the hadron gas EoS and the chiral EoS provide a reasonable description of the data, while the bag model EoS clearly overshoots the data. The data and the simulations are summarized in Fig. 2 (right) for the $R_{\text{out}}/R_{\text{side}}$ ratio for different beam energies. Here one clearly observes the expected maximum in the life time of the system in case of the bag model EoS. However, the data seem to favor a transition with a small latent heat without a substantial time delay as provided by the hadron gas EoS and the chiral EoS.

5. Dileptons

As a next step let us investigate the temperature and density evolution with penetrating probes. To this aim we compare coarse-grained transport simulations to hybrid-model calculations to explore differences due to the assumption of local equilibration and due to different spectral functions. Fig. 3 left shows the hybrid-model calculation [18] (Eletsky

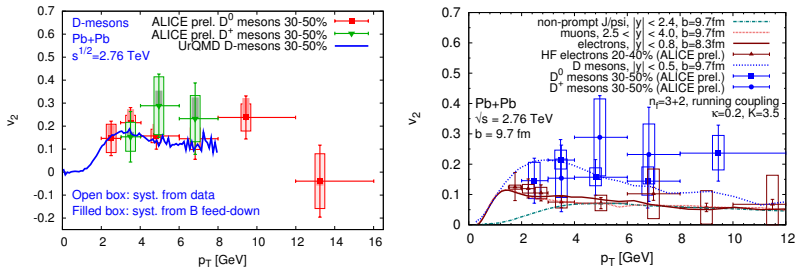


Fig. 4: Pb+Pb reactions at $\sqrt{s_{NN}} = 2.76$ TeV. Models compared to ALICE data [27]. Left: Hybrid model calculations with a Langevin treatment of the heavy quark dynamics [25]. Right: Parton cascade calculation. Figure taken from [26].

spectral function) for dimuon production in In+In reactions in comparison to the NA60 data [19]. One observes that the hybrid model provides a good description of the experimental data, however with a slight overestimation of the yield around the ρ peak. We compare this to the coarse-grained transport simulation [20] in Fig. 3 (right). In this case we show in addition a comparison to the Rapp-Wambach spectral function [21–23]. Generally we observe a very good description of the NA60 data [19]. The main differences between both approaches seem to be caused by the different spectral functions, with the Rapp-Wambach spectral function providing a better description of the data. The hybrid-model results also show an excess above the data of the ρ around its pole mass. This mainly stems from the initial and final stage which are handled by the hadronic cascade and where (in contrast to the hydrodynamic phase) no explicit medium modifications of the spectral shape are considered.

6. Charm

An alternative way to explore the properties of the created matter is to investigate its transport properties in terms of drag and diffusion coefficients. To this aim we model the propagation of heavy quarks, i.e., charm quarks through the matter created in the hybrid approach. In Fig. 4 we compare the results for the D-meson elliptic flow v_2 in

Pb+Pb collisions at the LHC based on the hybrid model [25] (left figure) with the results obtained from a recent parton cascade [26] study (right figure). For both cases we observe a similar quality for the description of the experimental data. This indicates that the density and temperature distribution and evolution in the hybrid approach and the parton cascade approach seem to be very similar. This may indicate that a substantial amount of local equilibrium is achieved in such collision as the dynamics of the heavy quarks does not seem to depend on the details of the system evolution.

7. Summary

In summary, hybrid models combining a hydrodynamic simulation for the hot and dense stages of the reaction coupled to Boltzmann dynamics for the early and late stage of the evolution provide an excellent tool to investigate the properties of QCD matter created at SPS, RHIC and LHC. For these proceedings we have discussed the modifications of the (anti-)proton yields due to absorption effects in the final state hadronic afterburner. We have then explored the temperature and density evolution by means of dilepton radiation and charm dynamics. In comparison to available data and alternative approaches, we concluded that the hybrid approach provides a reliable and sensible basis for these investigations.

8. Acknowledgements

M. B. wants to thank the organizers for an excellent meeting and many fruitful and stimulating discussions. This work has been supported by the Hessian LOEWE initiative through HIC for FAIR.

1. S. A. Bass *et al.*, Prog. Part. Nucl. Phys. **41**, 255 (1998) [Prog. Part. Nucl. Phys. **41**, 225 (1998)] [arXiv:nucl-th/9803035].
2. M. Bleicher *et al.*, J. Phys. **G25**, 1859 (1999) [arXiv:hep-ph/9909407].
3. H. Petersen, J. Steinheimer, G. Burau, M. Bleicher and H. Stoecker, Phys. Rev. C **78**, 044901 (2008) [arXiv:0806.1695 [nucl-th]].

-
-
4. M. Bleicher *et al.*, Nucl. Phys. A **638**, 391 (1998).
 5. P. Huovinen and H. Petersen, arXiv:1206.3371 [nucl-th].
 6. F. Becattini, M. Bleicher, T. Kollegger, M. Mitrovski, T. Schuster and R. Stock, Phys. Rev. C **85**, 044921 (2012) [arXiv:1201.6349 [nucl-th]].
 7. V. K. Magas, L. P. Csernai and D. Strottman, Nucl. Phys. A **712**, 167 (2002) [arXiv:hep-ph/0202085].
 8. L. P. Csernai, V. K. Magas, E. Molnar, A. Nyiri and K. Tamosiunas, Eur. Phys. J. A **25**, 65 (2005) [arXiv:hep-ph/0505228].
 9. R. Andrade, F. Grassi, Y. Hama, T. Kodama, O. J. Socolowski and B. Tavares, Eur. Phys. J. A **29**, 23 (2006) [arXiv:nucl-th/0511021].
 10. T. Hirano and M. Gyulassy, Nucl. Phys. A **769**, 71 (2006) [arXiv:nucl-th/0506049].
 11. C. Nonaka and S. A. Bass, Nucl. Phys. A **774**, 873 (2006) [arXiv:nucl-th/0510038].
 12. K. Werner, I. Karpenko, T. Pierog, M. Bleicher and K. Mikhailov, Phys. Rev. C **82**, 044904 (2010) [arXiv:1004.0805 [nucl-th]].
 13. J. Steinheimer, J. Aichelin and M. Bleicher, Phys. Rev. Lett. **110**, 042501 (2013) [arXiv:1203.5302 [nucl-th]].
 14. Y. Pan and S. Pratt, Phys. Rev. C **89** (2014) 4, 044911.
 15. F. Becattini, M. Bleicher, T. Kollegger, T. Schuster, J. Steinheimer and R. Stock, arXiv:1212.2431 [nucl-th].
 16. F. Becattini, E. Grossi, M. Bleicher, J. Steinheimer and R. Stock, Phys. Rev. C **90** (2014) 5, 054907 [arXiv:1405.0710 [nucl-th]].
 17. Q. f. Li, J. Steinheimer, H. Petersen, M. Bleicher and H. Stoecker, Phys. Lett. B **674**, 111 (2009) [arXiv:0812.0375 [nucl-th]].
 18. E. Santini, J. Steinheimer, M. Bleicher and S. Schramm, Phys. Rev. C **84**, 014901 (2011) [arXiv:1102.4574 [nucl-th]].
 19. R. Arnaldi *et al.* [NA60 Collaboration], Eur. Phys. J. C **61**, 711 (2009) [arXiv:0812.3053 [nucl-ex]].
 20. S. Endres, H. van Hees, J. Weil and M. Bleicher, arXiv:1412.1965 [nucl-th].
 21. R. Rapp, J. Wambach, Eur. Phys. J. A **6**, 415 (1999).
 22. R. Rapp and J. Wambach, Adv. Nucl. Phys. **25**, 1 (2000) [arXiv:hep-ph/9909229].
 23. H. van Hees and R. Rapp, Phys. Rev. Lett. **97** (2006) 102301 [hep-ph/0603084].
 24. S. Endres, H. van Hees, J. Weil and M. Bleicher, arXiv:1502.01948 [nucl-th].
 25. T. Lang, H. van Hees, J. Steinheimer and M. Bleicher, arXiv:1211.6912 [hep-ph].
 26. J. Uphoff, O. Fochler, Z. Xu and C. Greiner, Nucl. Phys. A **910-911**, 401 (2013) [arXiv:1208.1970 [hep-ph]].
 27. G. Ortona [ALICE Collaboration], arXiv:1207.7239 [nucl-ex].



Variational Principle of Hydrodynamics and Quantization Process

T. Kodama¹ and T. Koide¹

¹ *Universidade Federal do Rio de Janeiro, Rio de Janeiro, Brazil*

Abstract

The well-known hydrodynamic representation of the Schrödinger equation is reformulated in terms of variational form introducing Nelson-Yasue's stochastic variational method. In this approach, the fluid flow is composed by the two stochastic processes from the past and the future. We show that this formulation can be extended in a straightforward way to the quantization of scalar fields.

1. Introduction

Variational approach is very useful both in conceptual or practical side in many branch of physical phenomena, including the ideal hydrodynamics. The role of coarse-graining with respect to the resolution of collective flow observables is explicitly implemented in the variational form [1]. It is shown that non-relativistic Navier-Stokes equation can also be derived from the variational principle, if we extend the dynamical variable to the stochastic one [2].

It has been long time that the Schrödinger equation can be cast into the form of an ideal fluid, with additional quantum mechanical potential [3]. In this paper, we derive the action of the Schrödinger equation by introducing the two stochastic processes, first introduced by [4,5] and later developed by Yasue in the variational form [6,7]. Here we propose an alternative representation of the stochastic quantization requiring the maximum of the entropy associated with stochastic trajectories in order

to accommodate the boundary conditions within the variational formulation.

The present paper is organized as follows. In Sec.2, we introduce the two Brownian motions necessary in the variational formulation and postulate the maximum entropy principle. In Sec.3, the action of this combined fluid is shown to be equivalent to that of quantum mechanics. In Sec.4, an application of the present approach to the field quantization is discussed. Sec.5 is devoted to the summary and discussion.

2. Brownian motion

Let us consider a Brownian motion of a particle (or Lagrangian fluid element) due to some unknown external factor. In classical fluids, such a fluctuation occurs as the influence of the nature of fluid elements which consist of many internal degrees of freedom [2]. On the other hand, the origin of the stochasticity in quantum mechanics is not known. Here, we will not discuss what is this origin, but show that such a stochasticity can generate the internal energy.

In order to introduce the stochasticity, we suppose that the particle trajectory obeys a Brownian motion, which is characterized by

$$d\mathbf{r} = \mathbf{u}_F(\mathbf{r}, t) dt + \vec{\xi}_F, \quad dt > 0. \quad (1)$$

where $\vec{\xi}_F$ is the Gaussian noise defined by the probability distribution function,

$$P(\xi) = \frac{1}{\sqrt{2\pi\sigma^2}} e^{-\frac{\xi^2}{2\sigma^2}}, \quad (2)$$

where $\sigma^2 = \nu |dt|$ with ν is a constant parameter which characterizes the intensity of the noise and has a dimension of L^2/T . We refer Eq.(1) as forward stochastic difference equation (FSDE).

The particle distribution of this Brownian motion is calculated from FSDE and given by the following Fokker-Planck equation,

$$\frac{\partial \rho_F}{\partial t} + \nabla \cdot \mathbf{j}_F = 0, \quad (3)$$

where

$$\rho_F(\mathbf{r}, t) = \langle \delta(\mathbf{r} - \mathbf{r}(t)) \rangle_F, \quad (4)$$

$$\mathbf{j}_F(\mathbf{r}, t) = \rho_F(\mathbf{u}_F - \nu \nabla \ln \rho_F). \quad (5)$$

Here $\langle O(t) \rangle_F$ represents the average of O at the instant t over the whole events of the ensemble satisfying Eq(1). This equation, for a given \mathbf{u}_F , could be solved forward in time as an initial value problem. However, when we want to formulate the dynamics in terms of variational approach, we need to fix not only the initial but also the final particle distributions. The solution of the above Fokker-Planck equation does not satisfy a given final distribution in general. One possible way to control the final distribution, we think of a stochastic process backward in time. That is, instead of FSDE (1), we consider the backward stochastic differential equation (BSDE),

$$d\mathbf{r} = \mathbf{u}_B(\mathbf{r}, t) dt + \vec{\xi}_B, \quad dt < 0. \quad (6)$$

where $\vec{\xi}_B$ is the Gaussian noise as before obeying the probability distribution function, Eq.(2). The corresponding Fokker-Planck equation is

$$\frac{\partial \rho_B}{\partial t} + \nabla \cdot \mathbf{j}_B = 0, \quad (7)$$

where

$$\mathbf{j}_B = \rho_B(\mathbf{u}_B + \nu \nabla \ln \rho_B). \quad (8)$$

Note that the sign of the second term is opposite to Eq. (5).

How can we construct a set of stochastic processes which satisfy the both initial and final conditions by using these two Brownian motions? First let us consider trajectories which obey FSDE with a given initial condition and pass in the vicinity of \mathbf{r} at a certain time t which satisfies $t_I < t < t_F$. The number of the trajectories should be proportional to $\rho_F(\mathbf{r}, t)$. Similarly, the number of the backward trajectories which pass the same domain starting from the final distribution should be proportional to $\rho_B(\mathbf{r}, t)$. Therefore, for a given set of two distribution functions, $\{\rho_F(\mathbf{r}, t), \rho_B(\mathbf{r}, t)\}$ there are $N \propto \rho_F(\mathbf{r}, t) \rho_B(\mathbf{r}, t)$ ways to construct a trajectory which combines these two should be proportional to the product of the densities.

At this stage, we require that *the law of Nature describes the situation where this combined number is maximal for any instant t* . In other words, the entropy associated with this combination of trajectories should be maximum. We then define the entropy

$$S[\rho_F, \rho_B] \equiv \int d^3\mathbf{r} N \ln N. \quad (9)$$

From the variation of this entropy $\delta S = 0$ with the following constraint conditions,

$$\int d^3\mathbf{r} \rho_F(\mathbf{r}, t) = \int d^3\mathbf{r} \rho_B(\mathbf{r}, t) = 1, \quad (10)$$

we obtain

$$\rho_F(\mathbf{r}, t) = \rho_B(\mathbf{r}, t). \quad (11)$$

Therefore the density of trajectories ρ which satisfy the two boundary conditions is given by

$$\rho(\mathbf{r}, t) = \rho_F(\mathbf{r}, t) = \rho_B(\mathbf{r}, t). \quad (12)$$

Once we establish Eq.(11), we get from Eqs.(3,7)

$$\rho(\mathbf{u}_F - \nu \nabla \ln \rho) - \rho(\mathbf{u}_B + \nu \nabla \ln \rho) = \nabla \chi + \nabla \times \mathbf{A}, \quad (13)$$

where \mathbf{A} is an arbitrary time-dependent vector field [2] and χ is a scalar function which satisfies $\nabla^2 \chi = 0$. In the presence of \mathbf{A} , the velocity field should contain a vortex which is related to a singularity in space. Similarly, since $\lim_{|\mathbf{r}| \rightarrow \infty} \nabla \chi \rightarrow 0$, $\chi = \text{const.}$, if χ has no singularity. Here, for simplicity, we assume $\nabla \chi = \mathbf{A} = 0$. Then we obtain

$$\mathbf{u}_F - \mathbf{u}_B = 2\nu \nabla \ln \rho. \quad (14)$$

This is nothing but the same relation called the consistency condition in SVM [2, 6].

Because of this condition, the two Fokker-Planck equations are reduced to the simple continuity equation,

$$\partial_t \rho + \nabla \cdot (\rho \mathbf{u}_T) = 0, \quad (15)$$

where

$$\mathbf{u}_T = \frac{\mathbf{u}_F + \mathbf{u}_B}{2}. \quad (16)$$

3. Action principle and quantum mechanics

In the previous section, we introduce the stochastic process which is characterized by the two Brownian motions. As is in the hydrodynamic variational approach [8], the properties of these Brownian motions can be incorporated as the constraint condition in the variational approach. That is, once we know the kinetic term T and potential term U , the action which we should optimize is given by

$$I_q = \int dt \int d^3\mathbf{r} \rho \left\{ T - U - \kappa \dot{\lambda} - \kappa \nabla \lambda \cdot \mathbf{u}_T \right\}. \quad (17)$$

Here the Fokker-Planck equations (15) is taken into account as the constraint conditions with a Lagrange multipliers, λ .

From Eq.(15), we can identify the velocity \mathbf{u}_T with that of the translational motion of the fluid. Therefore, the translational kinetic energy T should be

$$T = \frac{m}{2} \mathbf{u}_T^2. \quad (18)$$

On the other hand, the relative velocity,

$$\mathbf{u}_r = \mathbf{u}_F - \mathbf{u}_B, \quad (19)$$

is irrelevant to the translational motion of the fluid element but should be associated with its internal energy. Note that such a situation occurs also in the case of the kinetic derivation of hydrodynamics, where the momentum of microscopic constituent particles are separated into two parts; one is to the fluid velocity and the other contributes to the internal energy [9]. Following this idea, the potential term is expressed as

$$U = \frac{m_{eff}}{2} \mathbf{u}_r^2 + V = 8\alpha^2 \nu^2 m (\nabla \ln \sqrt{\rho})^2 + V, \quad (20)$$

where $m_{eff} = \alpha^2 m$ is an effective mass with α a still undetermined constant and V is the external potential.

By using these results, the action 17 is a functional of the three independent functions form $I_q = I_q[\rho, \mathbf{u}_T, \lambda]$, but the variation with respect to \mathbf{u}_T gives the relation

$$m_{eff} \mathbf{u}_T = \kappa \nabla \lambda, \quad (21)$$

and substituting back to the action eliminating \mathbf{u}_T , we arrive at the following expression,

$$I_q[\rho, \lambda] = \int dt \int d^3\vec{r} \rho \left\{ -\frac{1}{2m} (\kappa \nabla \lambda)^2 - U - \kappa \dot{\lambda} \right\}. \quad (22)$$

Since κ is an arbitrary constant, we can always choose it so as to satisfy

$$\kappa = 4\alpha\nu m. \quad (23)$$

Now, instead of the two scalar variables, ρ and λ , let us introduce a complex variable

$$\psi = \sqrt{\rho} e^{i\lambda}. \quad (24)$$

Then the above action is further re-expressed as

$$I_q[\rho, \lambda] = \int_{t_i}^{t_f} dt \int d^3\mathbf{r} \psi^* \left\{ i\kappa \frac{\partial}{\partial t} - \hat{H} \right\} \psi, \quad (25)$$

where

$$\hat{H} = -\frac{\kappa^2}{2m} \nabla^2 + V. \quad (26)$$

If the parameter κ is identified with \hbar , Eq.(25) is the well-known form of the action for the Schrödinger Equation. In fact, the variation for ρ and λ leads to

$$\left[i\kappa \partial_t - \left(-\frac{\kappa^2}{2m} \nabla^2 + V(\mathbf{r}) \right) \right] \psi(\mathbf{r}, t) = 0. \quad (27)$$

It should be noted that our result of the variation becomes non-linear if the parameter does not satisfy Eq. (23). For such a nonlinear equation, see for example in Ref. [10]. However, because of the ambiguity for the definition of the phase λ , we can always find a parameter set satisfying Eq. (23) and thus a non-linear dynamics can be cast into the form of the linear equation (see also Ref. [11]). In other words, it seems that the wave function is a convenient representation but is not necessarily the fundamental element to construct quantum mechanics. This will be discussed in Sec. VI. In the following, we will refer this linear representation as ψ -representation.

4. Application to Field Quantization

The stochastic quantization procedure in terms of variational principle in the previous sections can be extended in a straightforward way for any system described by a vector variable, say $\vec{\phi}$ in stead of \mathbf{r} . As an example, we sketch in below how the present formulation can be applied to the quantization of a scalar field.

For this, we introduce the spatial lattice representation. Then we assign the field configuration $\phi(\vec{x})$ to a vector,

$$\phi(\vec{x}) \rightarrow \vec{\phi}, \quad (28)$$

in such a way that the scalar product of two functions is defined by

$$(f, h) = \int d^3x f(\vec{x}) h(\vec{x}) \rightarrow \Delta^3\mathbf{x} \vec{f} \cdot \vec{h} \quad (29)$$

with $\Delta^3\mathbf{x}$ being the lattice volume.

In this representation, the classical action for the scalar field $\phi(\vec{x})$ can be written as

$$\begin{aligned} I_{c.f.} &= \int_{t_i}^{t_f} dt \left[\frac{1}{2c^2} \Delta^3\mathbf{x} \left(\frac{d\vec{\phi}}{dt} \right)^2 + \frac{1}{2} \Delta^3\mathbf{x} \vec{\phi} \cdot \mathbf{\Delta}_{\mathbf{x}} \vec{\phi} - V(\vec{\phi}) \right], \end{aligned} \quad (30)$$

where V is the potential containing the mass term and $\mathbf{\Delta}_{\mathbf{x}}$ is the matrix corresponding to the discretized Laplacian operator [12]. By denoting a formal correspondence $\vec{r} \rightarrow \vec{\phi}$, $d^3\vec{r} \rightarrow d^{N^3}\vec{\phi} \equiv [D\phi]$, we can repeat the analogous procedure in the previous sections. Finally we obtain

$$\begin{aligned} I_{q.f.} &= \int_{t_i}^{t_f} dt \int [D\phi] \rho[\phi] \\ &\times \left[\int d^3\mathbf{x} \left(\frac{(\kappa c)^2}{2} \left\{ \left(\frac{\delta \lambda}{\delta \phi(x)} \right)^2 - \left(\frac{\delta \ln \sqrt{\rho}}{\delta \phi(x)} \right)^2 \right\} \right. \right. \\ &\left. \left. + \frac{1}{2} \phi(x) \nabla^2 \phi(x) \right) - V[\phi] - \kappa \partial_t \lambda \right]. \end{aligned} \quad (31)$$

In the above, the notation of the continuum limit is used, $(\Delta^3 \mathbf{x})^{-1} \nabla_{\phi} \rightarrow \delta/\delta\phi(x)$. $\rho[\phi]$ represents the functional distribution of field configuration ϕ .

As before, in terms of wave functional,

$$\Psi[\phi] \equiv \sqrt{\rho} e^{i\lambda}, \quad (32)$$

the above action is expressed as

$$I_{q.f.} = \int_{t_i}^{t_f} dt \int [D\phi] \Psi^*[\phi] \left[i\kappa c \partial_{ct} - \hat{\mathcal{H}} \right] \Psi[\phi], \quad (33)$$

where

$$\hat{\mathcal{H}} = \int d^3 \mathbf{x} \left\{ -\frac{\kappa^2 c^2}{2} \left(\frac{\delta}{\delta\phi(x)} \right)^2 - \frac{1}{2} (\nabla\phi(x))^2 \right\} + V. \quad (34)$$

Taking variations with respect to the two functionals $\rho[\phi]$ and $\lambda[\phi]$, we arrive at the functional Schrödinger equation [12]

$$i \kappa c \partial_{ct} \Psi[\phi] = \hat{\mathcal{H}} \Psi[\phi]. \quad (35)$$

Note that, for the scalar field system, the corresponding condition to Eq.(23) determines the relation between the noise intensity and the universal constant, κc^2 .

5. Summary and Discussion

In this work, we formulated the quantization of one-particle classical system in terms of the variational approach. There are three requirements in the present derivation; 1) quantum fluctuation is expressed as stochastic noises of the Brownian motion, 2) the two stochastic flows from the past and the future are characterized by the maximum of the entropy associated with the number of combinatory possibilities which connect the initial and final distributions, and 3) the action of the system is given by the same form of a classical ideal fluid, but contains a contribution from the internal energy. Under these assumptions, we

showed that this fluid action can be cast into the action principle for the Schrödinger equation. One of the advantages of the present variational form is that operators associated with physical observables in the ψ -representations are defined by Noether's theorem [13]. Accordingly, eigenvalues and eigenstates of the physical observables are consistently defined. We further showed that the present formulation can be applied to the system of scalar field. The applicability to the quantization of the fermion field still remains as an open question.

In the present formulation, the dynamics of fluid is always irrotational, as seen from Eq.(21) if λ has no singularity. This is the principal question to identify the fluid representation to the ψ -representation as pointed out by Takabayashi and Wallstrom. The usual hydrodynamic representation of the Schrödinger equation cannot treat the cases where the phase of wave functions becomes multi-valued, such as the eigenstates of the angular momentum unless introducing an additional condition which requires that the vortex number is quantized [14,15]. However, in the field quantization, the vorticity in question refers to the flow in the functional space. For example, quantized angular momentum should be understood as the stationary state of the classical field. For the case of the scalar field, the hydrodynamic equations in the functional space can be derived from the variation of Eq.(31) and the flow in the functional space can be taken always irrotational. In particular for the free Klein-Gordon case, we obtain the correct energy eigenvalues as the stationary states without resort to the ψ -representation in functional space [12]. To our knowledge, it is not clear that the Takabayashi-Wallstrom criticism is still valid for the functional fluid representation of quantized fields.

It is interesting to note that the intensity of the noise for the field quantization is given uniquely by the universal constant $\kappa c^2 = \hbar c^2$ as seen from Eqs.(33,34). This suggest that the field variables and the space-time structure were born simultaneously in such a way that quantum mechanics and relativity have the same origin, just as if the macroscopic variables and the noise on them. If this is the case, we would need to reconsider the meaning of quantization of gravity.

We have assumed that the stochasticity is characterized by the Gaus-

sian white noise. This reminds us the well-known the central limit theorem and suggests that there may exist another hypermicro-stochastic process which is reduced to the Gaussian white noise only after taking the central limit theorem. This aspect seems to be consistent with the maximum entropy postulate which we have adopted, since the average of large micro-stochastic process should lead to certain statistical equilibrium.

The authors thank to the Organizers of the nice IWOC meeting for giving us an opportunity to commemorate 65-th birthday of our dear friend, Laszo Csernai. We also acknowledge the fruitful discussions with N. Suzuki, K. Tsushima and P. Ván. This work has been supported by CNPq, FAPERJ, CAPES and PRONEX.

1. Mota Ph et al., 2012 Eur. Phys. J. A 48 165; T. Kodama and T. Koide, Journal of Physics: Conference Series 509 (2014) 012016
2. T. Koide and T. Kodama, J. Phys. A: Math. Theor. 45, 255204 (2012) and references therein.
3. P. R. Holland, *The Quantum Theory of Motion: An Account of the de Broglie-Bohm Causal Interpretation of Quantum Mechanics*, (Cambridge University Press, Cambridge, 1995).
4. E. Nelson, Phys. Rev. 150, 1079 (1966); Quantum Fluctuations, (Princeton Univ. Press, Princeton, NJ, 1985).
5. A similar approach has been also proposed by I.Fényes, Z. Physik 132, 81 (1952); W. Weizel, Z. Physik 134, 264 (1953); 135, 270 (1953); 136, 582 (1954).
6. K. Yasue, J. Funct. Anal. 41, 327 (1981);
7. F. Guerra and L. M. Morato, Phys. Rev. D27, 1774 (1983); M. Pavon, J. Math. Phys. 36, 6774 (1995); M. Nagasawa, Stochastic Process in Quantum Physics, (Birkhäuser, 2000).
8. See for example, Elze H-T et al 1999 J. Phys. G 25 1935.
9. See, for example, R. Zwanzig, *Nonequilibrium Statistical Mechanics* (Oxford university press, New York, 2001).
10. P. Garbaczewski, Phys. Rev. E78, 031101 (2008).
11. A. Caticha, J. Phys. A; Math. Theor. 44, 225303 (2011).
12. T. Koide and T. Kodama, arXiv:1306.6922; T. Koide ,T. Kodama, and K. Tsushima, arXiv:1406.6295.
13. T. Kodama and T. Koide, arXiv preprint arXiv:1412.6472.

14. T. Takabayashi, *Prog. Theor. Phys.* **8**, 143, 1952; *ibid.* **9**, 187 (1953).
15. T. C. Wallstrom, *Phys. Rev. A* **49**, 1613 (1994).

Evaluating the role of coarse graining in hydrodynamic modeling of heavy-ion collisions from microscopic dynamics

R.D. de Souza^{1,2}, T. Kodama¹, T. Koide¹, J.H.G. Elsas¹,
E.L. Bratkovskaya³, W. Cassing⁴

¹ *Universidade Federal do Rio de Janeiro, Rio de Janeiro, Brazil*

² *Universidade Estadual de Campinas, Campinas, Brazil*

³ *Frankfurt Institute for Advanced Studies, JWG Universität Frankfurt, D-60438 Frankfurt am Main, Germany*

⁴ *Institut für Theoretische Physik, Universität Giessen, D-35392 Giessen, Germany*

Abstract

The hydrodynamic modeling of the system evolution in relativistic heavy-ion collisions has been very successful in describing the collective flow patterns observed experimentally. However, the matter created initially in such collisions has small scales in space and contains large fluctuations as addressed by 'lumpy' initial conditions. Therefore, the theoretical justification for the hydrodynamic approach is still an open question. We discuss the role of the coarse-graining procedure and the measure of local thermal equilibrium required for a hydrodynamic modeling. In order to investigate how the hydrodynamic behavior can appear in heavy-ion collisions we use a microscopic model which is constructed on the basis of Kadanoff-Baym dynamics without assuming local equilibrium. The Parton-Hadron-String Dynamics (PHSD) approach is suitable for this purpose since it accounts for multiparticle effects by means of 'resummed' selfenergies. From the properties of the energy-momentum tensor in the local rest frame, we discuss the degree of the local thermal equilibrium in this model and related equilibration times.

1. Introduction

Heavy-ion collision experiments have allowed to study the properties of matter under extreme conditions of density and temperature. The observations from these experiments indicate that the system created in such violent collisions behaves in a collective way [1–4]. In particular, the anisotropic flow of the produced particles observed via the Fourier coefficients v_n of the azimuthal angular distribution as a function of the transverse momentum (p_t) has been shown to be an important signal of this collective evolution, hence transferring the initial geometric anisotropy in the overlap region between the two incident nuclei into a final momentum anisotropy. Moreover, recent experimental results such as the 'ridge' observed in two-particle correlations also suggests an initial state nature [5]. Thus, a relativistic hydrodynamic modeling of the system evolution in heavy-ion collisions has been very successful in describing the experimental measurements [6–9]. However, one needs to be careful with all the assumptions required for a hydrodynamic description and a precise analysis of the profile of the dynamics may furnish informations about the properties of the matter as well as the initial condition of the collision (cf. the discussions in Ref. [10]).

2. Coarse-graining Scale in Hydrodynamic Modeling

In the hydrodynamic modeling one generally needs a closed system of equations for local macroscopic variables, based on conservation laws for the energy-momentum tensor and the conserved currents, with additional equations to describe some well defined thermodynamical properties of the matter in question, i.e. the equation of state (EoS) and relaxation equations with transport coefficients (if necessary). The fundamental hypothesis for such a situation is the local thermodynamical equilibrium which eliminates all microscopic degrees of freedom. Nevertheless, in the case of relativistic heavy-ion collisions, where we have a violent process (and short time scale) and large fluctuations in a very small volume, it is not guaranteed that such conditions will always be satisfied. Thus, if the hydrodynamic approach is able to describe the observed ensemble

averages of experimental data, the natural question arising is how precise are we looking at the system's profile. If the observables investigated do not have a good resolution of the macroscopic dynamics, then the properties of the matter that we deduce may also not be precise but just an effective description (effective EoS). The concept of a coarse-grain scale in hydrodynamic modeling can thus be thought as a resolution for which one can support "true" hydrodynamic description, i.e., one event hydrodynamics rather than an ensemble average over many events.

Hydrodynamics can be regarded as an effective theory based on variational principle [11] and the formulation of dissipative processes can be achieved by treating the effects of microscopic degrees of freedom as "random noise" (stochastic differential equation, SDE). The quantum mechanical variational action can be identified with the action of a classical fluid with noises, consistent to the boundary condition with maximum probability of the product of the systems with forward and backward noises.

3. Hydrodynamic Representation of Microscopic Dynamics

In order to investigate whether a hydrodynamic profile might emerge from the microscopic dynamics of a system, which contains many-body interactions (compression effects), one can evaluate the properties of the energy-momentum tensor $T^{\mu\nu}(\vec{r})$ defined by the particles of the system in the neighborhood of some space point \vec{r} :

$$T^{\mu\nu}(\vec{r}) = \sum_i \frac{p_i^\mu p_i^\nu}{p_i} W(\vec{r} - \vec{r}_i; h), \quad (1)$$

where p_i^α are the components of the four-momentum of particle i and $W(\vec{r} - \vec{r}_i; h)$ is some kernel function which defines the range of the neighborhood of interest, satisfying the normalization condition:

$$\int d\vec{r} W(\vec{r} - \vec{r}_i; h) = 1. \quad (2)$$

We have tested two types of kernel function: (a) a simple rectangular box in which $W=1/(\Delta x \Delta y \Delta z)$ if the particle is inside the box and $W=0$

if it is outside, with $\Delta x = \Delta y$ being the transverse lengths and $\Delta z(t)$ the longitudinal length of the box; (b) a 3D gaussian with characteristic lengths defined by the widths h_t in the transverse direction and $h_z(t)$ in the longitudinal direction. For both cases, the longitudinal length is a function of time and follows the system expansion by keeping a constant rapidity window. Once the $T^{\mu\nu}(\vec{r}, t)$ is known, a diagonalization procedure is applied such that the resulting tensor is of the type $[T_L]^{\mu\nu} = \text{diag}\{\varepsilon, P_T, P_T, P_L\}$. The diagonalization can be identified with a Lorentz transformation $\Lambda(\vec{\beta})$ plus a spatial rotation R . Therefore, this procedure allows the extraction of the flow profile, i.e. the velocity field ($\vec{\beta}$), the local energy density (ε) and the pressure components (P_i).

The model adopted to perform this analysis is the Parton-Hadron-String Dynamics (PHSD) approach [12–16]. This model is particularly suitable for this type of study since it treats the microscopic transport during the system evolution using effective (resummed) strongly interacting dynamical quasi-particles and off-shell hadrons as degrees of freedom [12–14, 17]. The dynamics of many-body interactions for each event simulated in PHSD is computed via mean-field potentials, which are determined by the particles of a number of parallel events starting from the same initial condition. Therefore, by increasing the number of parallel events used to calculate the mean-field potentials, which we refer here as NUM, one also increases the effect of the potentials in the dynamics of the system evolution. The plots in Fig. 1 show the longitudinal profiles of the components of the particle velocity for two snapshots of the evolution (the open circles represent the mean values of the distributions) for one PHSD event of a Au+Au collision at $\sqrt{s_{NN}} = 200$ GeV.

We have computed the energy-momentum tensor during the evolution of an event generated with PHSD using both kernel function discussed before. The left plot in Fig. 2 shows the dependence of the local energy density as a function of time for the rectangular box (red curve) and the gaussian kernel (black curve). Here we compute the energy-momentum tensor in the neighborhood of the origin ($x=0, y=0, z=\eta=0$), with a rapidity window $\Delta\eta=0.1$. Note, that we chose the sizes for each kernel to be of roughly the same order, though, they are not exactly equivalent. Both cases present a very similar behavior, with the gaus-

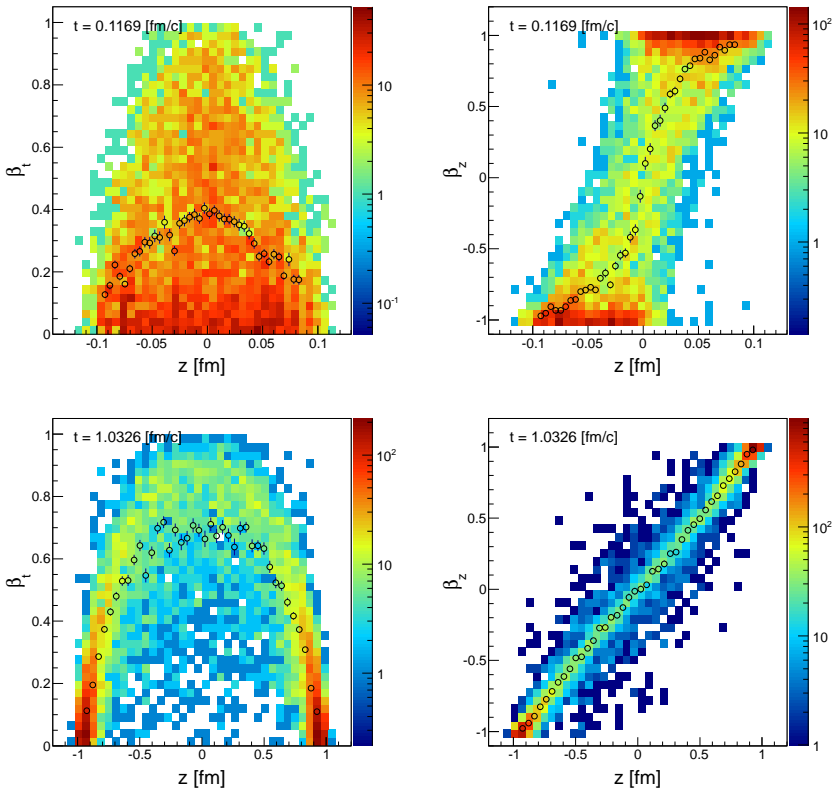


Fig. 1: Snapshots of the longitudinal profile of the particle velocity in PHSD for two different time-steps of the evolution for a Au+Au collision at $\sqrt{s_{NN}} = 200$ GeV.

sian kernel being smoother and more strongly correlated (as expected). Therefore, we abandoned the rectangular box in our subsequent tests and varied the characteristic length in the gaussian kernel. The plot on the r.h.s. of Fig. 2 shows the dependence of the ratios of the longitudinal (P_L) and transverse (P_T) components of the pressure with respect to the local energy density ϵ as a function of the system evolution. In this case we have computed the $T^{\mu\nu}$ in the neighborhood of the point $(x, y, z) = (1, 0, 0)$ (avoiding the divergence at the origin) and we tested four different sizes of the longitudinal length of the gaussian kernel, dis-

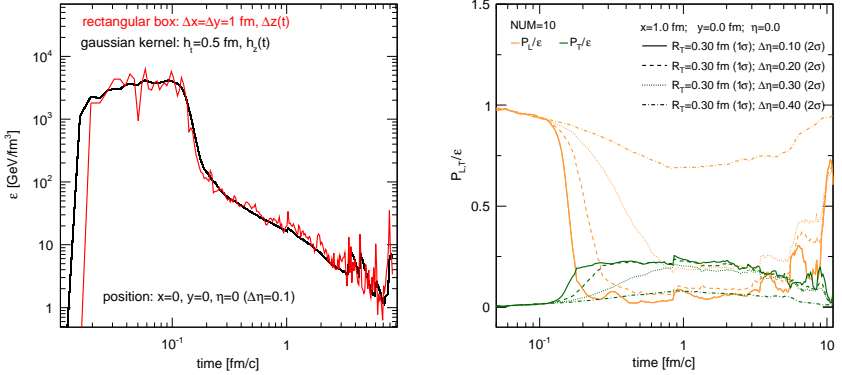


Fig. 2: Dependence of the local energy density ϵ with the time evolution for two different types of kernel functions (left plot); dependence of the longitudinal and transverse pressure components with the system evolution considering different characteristic lengths in the longitudinal direction (right plot).

played in the legend of the plot by $\Delta\eta$ and corresponding to the range of $-\sigma$ to $+\sigma$ around the gaussian peak. The transverse length was kept fixed to 0.3 fm (which corresponds to 1σ of the gaussian kernel). For all situations tested we observe that the transverse and longitudinal components of the pressure starts very low and very high, respectively, and then increase or decrease starting in the very initial stages of the evolution ($t \sim 0.2 \text{ fm}/c$). The important point in this plot is the convergence between the pressure components observed for $\Delta\eta=0.3$ (dotted lines). As can be seen, this is the only case where the pressure becomes isotropic and it lasts for an interval of only about $2 - 3 \text{ fm}/c$, starting at $t \sim 1.0 \text{ fm}/c$. With a further increase of the longitudinal length of the gaussian kernel, the isotropy of the pressure components does not hold anymore. We have also tested different sizes of the transverse length of the kernel without observing any important change in the behavior. In addition, in the context of this work, the number of events used in the calculation of the mean-field potential may also be thought as being related to the coarse-graining scale for the collectivity of the system during its evolution. We have tested different situations for the parameter NUM (1, 2, 5, 10, 20 and 30) and found that the general behavior converges

for $\text{NUM} > 5$ (the fluctuations are very large otherwise), thus we used $\text{NUM} = 20$ and $\text{NUM} = 10$ in the analysis shown in the left and right plots of Fig. 2, respectively.

We also tested the events produced with PHSD to check whether the initial spatial anisotropy, computed as:

$$\varepsilon_n = \frac{\langle r^n \cos(n[\phi - \Phi_n]) \rangle}{r^n}, \text{ with } \begin{cases} \phi = \arctan(y/x) \\ \Phi_n = \frac{1}{n} \arctan\left(\frac{\langle r^n \sin(n\phi) \rangle}{\langle r^n \cos(n\phi) \rangle}\right) \end{cases}, \quad (3)$$

is transferred to a final momentum anisotropy, given by the flow coefficients calculated with respect to the initial eccentricity angle:

$$v_n = \langle \cos(n[\psi - \Psi_n]) \rangle, \text{ with } \begin{cases} \psi = \arctan(p_y/p_x) \\ \Psi_n = \Phi_n + \pi/n \end{cases}. \quad (4)$$

The left plot in Fig. 3 shows the behavior of the coefficients ε_2 and v_2 as a function of the evolution of the system for a single PHSD event. The

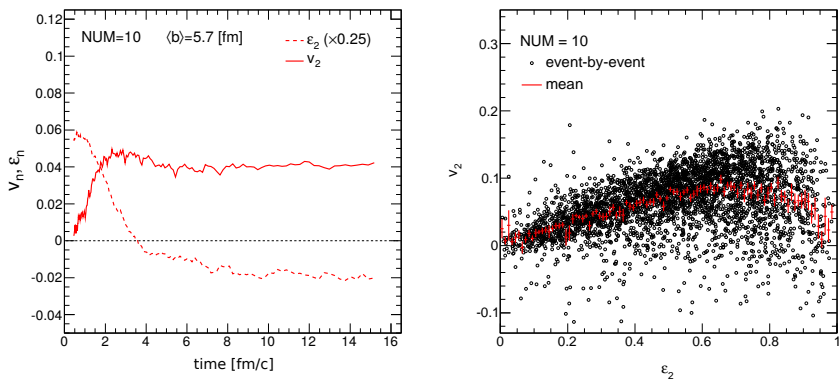


Fig. 3: Time evolution of the spatial eccentricity ε_2 and the elliptic flow coefficient v_2 for a single event (left plot); the distribution of ε_2 vs v_2 (right plot) for many events. The red line represents the average $\langle v_2 \rangle$.

plot on the r.h.s. shows the distribution of the final v_2 versus the initial ε_2 coefficients for a sample of many events. The positive correlation observed indicates that the system behaves collectively. Moreover, the relevant transfer of the anisotropy from the initial to the final states occurs during the initial (partonic) stages.

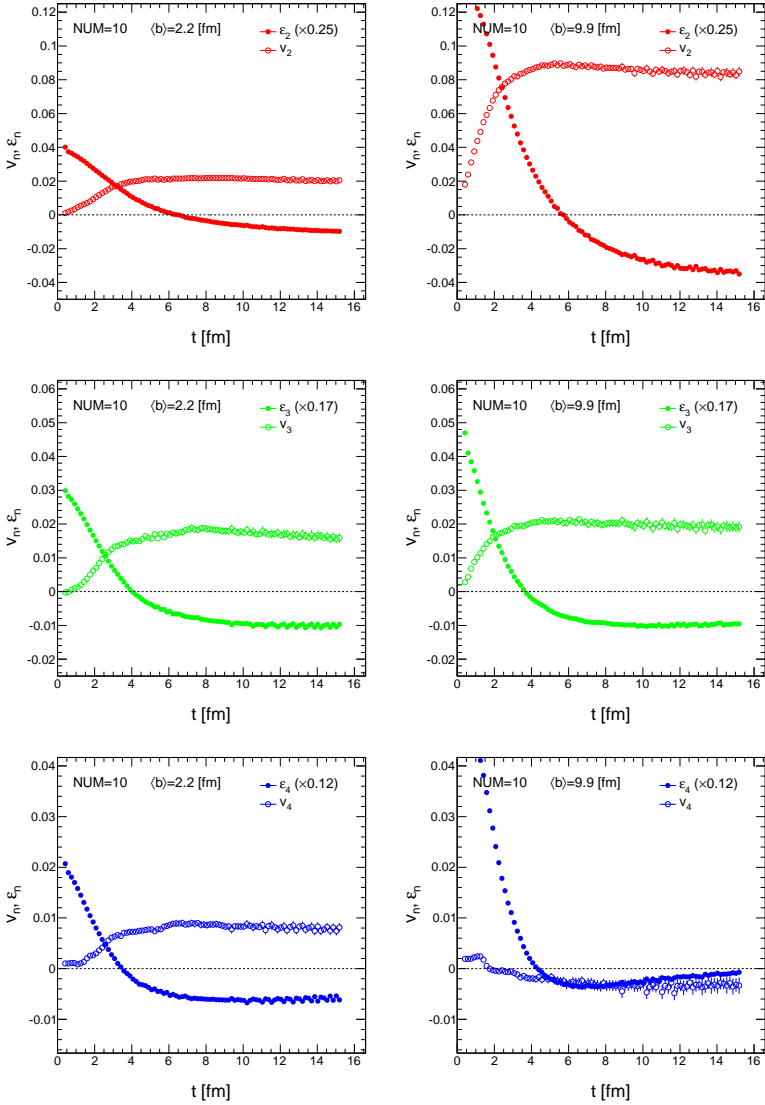


Fig. 4: Time evolution of the spatial ϵ_n and the momentum v_n anisotropy coefficients for central (left plots) and peripheral (right plots) events. From top to bottom, the plots show the results for the second, third and fourth harmonics, respectively.

Higher harmonics show a similar behavior for central and intermediate cases (see Fig. 4), but the “quality” of the transfer becomes poor for the most peripheral cases. We note that very similar results have been observed in ideal hydrodynamic calculations as discussed in Refs. [18,19], which demonstrates that even if complete local equilibrium is not present, the usual observables for the system collectivity are similar and not sensitive to deviations from equilibrium. Therefore, further developments are still necessary to help to understand the details of the evolution of the system formed in heavy-ion collisions.

4. Summary

We have tested the coarse-graining scale for a hydrodynamic description within the microscopic dynamics as provided by the PHSD approach and found that the system seems to approach “equilibrium” only for very specific situations. We also noticed a very clear separation of the flow profile into longitudinal and transverse components, similar to what has been observed in studies about the very initial field configuration in Refs. [20,21]. Although the condition of local thermal equilibrium may not be perfectly satisfied, the correlation observed between the initial spatial anisotropy and the final momentum anisotropy is consistent with a collective evolution of the system. Therefore, the development of new observables that are sensitive to deviations from equilibrium of the matter during the system evolution is of great interest to understand the collective properties of heavy-ion collisions and the evolution of collectivity.

1. K. Adcox et al, Nucl. Phys. **A757** 184 (2005).
2. J. Adams et al., Nucl. Phys. **A757** 102 (2005).
3. B.B. Back et al., Nucl. Phys. **A757** 28 (2005).
4. I. Arsene et al., Nucl. Phys. **A757** 1 (2005).
5. P. Sorensen, B. Bolliet, A. Mocsy, Y. Pandit and N. Pruthi, Phys. Lett. **B705** 71 (2011).
6. P.F. Kolb and U.W. Heinz, arXiv:nucl-th/0305084 (2003).

7. Y. Hama, T. Kodama, and O. Socolowski Jr., *Braz. J. Phys.* **35** 24 (2005).
8. J. Takahashi, B.M. Tavares, W.L. Qian, R. Andrade, F. Grassi, et al., *Phys. Rev. Lett.* **103** 242301 (2009).
9. C. Gale, S. Jeon and B. Schenke, *Int. J. Mod. Phys.* **A28** 1340011 (2013).
10. J. Berges, J.-P. Blaizot and F. Gelis, *J. Phys.* **G39** 085115 (2012).
11. H.-T. Elze, Y. Hama, T. Kodama, M. Makler and J. Rafelski, *J. Phys.* **G25** 1935 (1999).
12. W. Cassing and E. L. Bratkovskaya, *Phys. Rev. C* **78** 034919 (2008).
13. W. Cassing and E.L. Bratkovskaya, *Nucl. Phys.* **A831** 215 (2009).
14. W. Cassing, *Eur. Phys. J. ST* **168** 3 (2009).
15. A. Peshier and W. Cassing, *Phys. Rev. Lett.* **94** 172301 (2005).
16. W. Cassing, *Nucl. Phys.* **A791** 365 (2007), *ibid.* **A795** 70 (2007).
17. E.L. Bratkovskaya, W. Cassing, V.P. Konchakovski and O. Linnyk, *Nucl. Phys.* **A856** 162 (2011).
18. F.G. Gardim, F. Grassi, M. Luzum and J.-Y. Ollitrault, *Phys. Rev. C* **85** 024908 (2012).
19. F.G. Gardim, F. Grassi, M. Luzum and J.-Y. Ollitrault, *Nucl. Phys.* **A904-905** 503c (2013).
20. T. Epelbaum and F. Gelis, *Phys. Rev. Lett.* **111** 232301 (2013).
21. V.P. Konchakovski, W. Cassing, and V.D. Toneev, *J. Phys.* **G41** 105004 (2014) 105004; arXiv:1411.5534 [nucl-th].

Heavy Quark Dynamics in QGP: Boltzmann vs Langevin

Vincenzo Greco^{a,b}, Francesco Scardina^{a,b}, Santosh Kumar Das^{a,b}
and Salvatore Plumari^{a,b}

^a *Department of Physics and Astronomy, University of Catania, Via S. Sofia 64, 95125 Catania, Italy,*

^b *Laboratori Nazionali del Sud, INFN-LNS, Via S. Sofia 62, I-95123 Catania, Italy*

Abstract

In this talk we challenge the assumption of brownian motion for charm quarks and compare the dynamical evolution of charm and bottom quarks in a Fokker-Planck approach and in a Boltzmann Transport one. We show that while for bottom the motion appears quite close to a Brownian one, this does not seem to be the case for charm quarks. We study the back-to-back azimuthal correlation of charm quarks produced in relativistic heavy-ion collisions within both Boltzmann and Langevin dynamics. We have found that Boltzmann approach gives rise to a larger spreading of $c\bar{c}$ correlation in comparison with the Langevin approach.

1. Introduction

One of the primary aims of the ongoing nuclear collisions at Relativistic Heavy Ion Collider (RHIC) and Large Hadron Collider (LHC) energies is to create a new state of matter where the bulk properties of the matter are governed by the light quarks and gluons. In this context, the heavy quarks (HQ), mainly charm and bottom, play a crucial role since they do not constitute the bulk part of the matter due to their larger mass with respect to the temperature created in ultra-relativistic heavy-ion

collisions (uRHIC's) [1]. Due to their large masses HQ can act as a type of external probe to investigate the bulk of the QGP medium and are affected by its density, temperature and collective expansion thereby carrying the information of the created plasma.

In the next section, we will focus on the theoretical approaches to describe the dynamical evolution of the HQ comparing the most commonly used Fokker-Planck approach to the Boltzmann transport equation. In section III we discuss the evolution of the HQ spectra in a static medium. Section IV is devoted for single heavy quark diffusion in momentum space. In section V the results for $c\bar{c}$ correlation are presented. Section IV contain the summary and conclusions.

2. Boltzmann vs Langevin dynamics

The propagation of HQ in QGP has been quite often treated within the framework of Fokker-Planck equation [1, 2]. The main reason is that it was believed that their motion can be assimilated to a Brownian motion due to their perturbative interaction and large mass that should generically lead to collisions sufficiently forward peaked and/or with small momentum transfer. Under such constraints it is known that the Boltzmann transport equation reduces to a Fokker-Planck dynamics, which constitutes a significant simplification of the in medium dynamics. Such a scheme has been very widely employed including some of the authors [2–5, 10, 11] in order to calculate the experimentally observed nuclear suppression factor (R_{AA}) [7–9] and their large elliptic flow (v_2) [7] for the non-photonic single electron spectra. Along with the Fokker-Planck approach in some work a description of HQ within a relativistic Boltzmann transport approach has been developed [6, 12–14, 18].

The Boltzmann equation for the HQ distribution function can be written in a compact form as:

$$p^\mu \partial_\mu f_Q(x, p) = \mathcal{C}[f_Q](x, p) \quad (1)$$

where $\mathcal{C}[f_Q](x, p)$ is the relativistic Boltzmann-like collision integral where the phase-space distribution function of the bulk medium appears as an integrated quantity in $\mathcal{C}[f_Q]$, see for example Ref.s [17], while we

are interested to the evolution of the heavy quarks distribution function $f_Q(x, p)$.

The Boltzmann equation is solved numerically dividing the space into a three-dimensional lattice and using the test particle method to sample the distributions functions. The collision integral is solved by mean of a stochastic implementation of the collision probability $P = v_{rel}\sigma_{g+Q\rightarrow g+Q} \cdot \Delta t/\Delta x$ [16, 17].

The non-linear integro-differential Boltzmann equation can be significantly simplified employing the Landau approximation whose physical relevance can be associated to the dominance of soft scatterings with small momentum transfer $|\mathbf{k}|$ respect to the particle momentum \mathbf{p} . Under this assumption the non-linear integro-differential Boltzmann equation reduced to the Fokker-Planck equation (for detail see Ref [15]):

$$\frac{\partial f}{\partial t} = \frac{\partial}{\partial p_i} \left[A_i(\mathbf{p})f + \frac{\partial}{\partial p_j} [B_{ij}(\mathbf{p})] \right] \quad (2)$$

where A_i and B_{ij} are directly related to the so called drag and diffusion coefficient. The Fokker-Planck equation can be solved by a stochastic differential equation i.e the Langevin equation, can be written as [1, 2, 4]:

$$\begin{aligned} dx_i &= \frac{p_i}{E} dt, \\ dp_i &= -Ap_i dt + (\sqrt{2B_0}P_{ij}^\perp + \sqrt{2B_1}P_{ij}^\parallel)\rho_j\sqrt{dt} \end{aligned} \quad (3)$$

where dx_i and dp_i are the coordinate and momentum changes in each time step dt . A is the drag force and B the longitudinal and transverse diffusions, ρ is a stochastic variable Gaussian distributed. in terms of independent Gaussian-normal distributed random variables ρ_j , and

$$P_{ij}^\perp = \delta_{ij} - \frac{p_i p_j}{p^2}, P_{ij}^\parallel = \frac{p_i p_j}{p^2}. \quad (4)$$

are the transverse and longitudinal tensor projectors. We will employ the common assumption, $B_0 = B_1 = D$ [2-6, 10].

3. Numerical results

We now discuss the evolution of momentum distributions of charm and bottom quarks interacting with a bulk medium at $T = 0.4 \text{ GeV}$ with

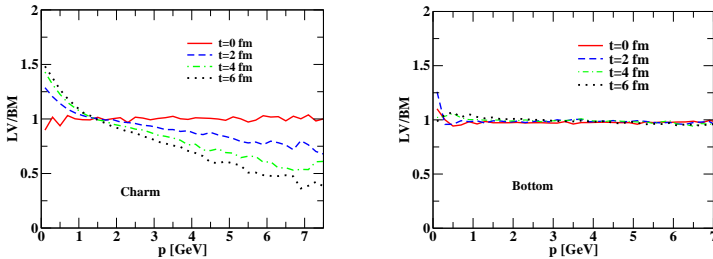


Fig. 1: Ratio between the Langevin (LV) and Boltzmann (BM) spectra as a function of momentum for $m_D = gT$ GeV at different time. Left: charm quarks; Right: bottom quark.

scattering processes determined by the scattering matrices discussed in the previous section. The initial distribution of heavy quarks are $f(p, t = 0) = (a + bp)^{-n}$ with $a = 0.70$ (57.74), $b = 0.09$ (1.00) and $n = 15.44$ (5.04) for charm and bottom quarks respectively. The above function gives a reasonable description of D and B meson spectra in the p-p collision at highest RHIC energy. For the sake of comparison, we solve both the Langevin equation and the Boltzmann equation as described in the above Section. Our purpose is to compare the time evolution starting from the same initial momentum distribution for the both cases. The differential cross section $d\sigma/d\Omega$, main ingredient of the Boltzmann equation, and the drag and diffusion coefficients, key ingredient of the Langevin equation, both originated from the same scattering matrix. The elastic collisions of heavy quarks with gluon has been considered within the pQCD framework to calculate the drag, diffusion coefficients and differential cross section. In the present calculation we used $\alpha_s = g^2/4\pi = 0.35$ and the Debye screening mass as $m_D = gT$. We have plotted the results as a ratio between Langevin to Boltzmann at different times to quantify how much the ratio deviates from 1. In Fig 1 (Left) the ratio of Langevin to Boltzmann spectra for the charm quark with $m_D = gT$ GeV has been displayed as a function of momentum at different time. From Fig 1 it is observed that for $t = 4$ fm the deviation of Langevin from Boltzmann is around 40% and for $t = 6$ fm the deviation is around a 50% at $p = 5$ GeV, which suggests the Langevin

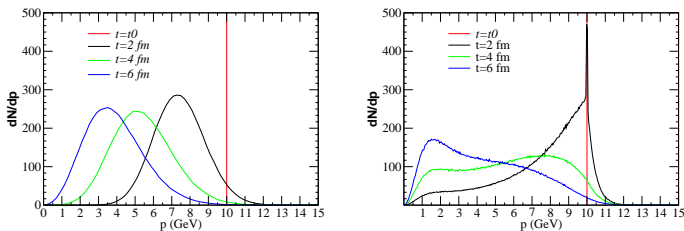


Fig. 2: Evolution of charm quark momentum distribution within Boltzmann equation considering for a charm quark initially at $p=10$ GeV. Right: Langevin dynamics. Left: Boltzmann dynamics.

approach overestimates the average energy loss considerably due to the approximation it involves. We now move to the calculation for bottom quarks. In Fig. 1 (Right) the results for bottom quark are displayed for $m_D = gT$ GeV. It is observed that the ratio stays practically around one for bottom quark for all the time evolution considered in the manuscript.

4. Heavy quark diffusion in momentum space

A more thorough investigation of the heavy quark evolution implied by a Langevin and a Boltzmann approach, we study the heavy quark momentum evolution considering the initial charm quark distribution as a delta distribution at $p = 10$ GeV for the case with $m_D = gT$ GeV. The momentum evolution of the charm quarks are displayed in Fig. 2 (left) within the Langevin dynamics. As known the Langevin dynamics consists of a shift of the average momenta with a fluctuation around that includes also the possibility to gain energy for the HQ as we see from the tail of the momentum distribution that overshoots the initial momentum $p = 10$ GeV at $t = 2$ fm/c, black solid line in Fig.2 (left).

In Fig. 2 (right) we present the momentum distribution for charm quark within the Boltzmann equation, is evident a very different evolution of the particles momentum already at $t = 2$ fm/c has a very different spread in momentum with a long tail at low momenta corresponding to some probability to loose a quite large amount of energy and in general a global shape that is not at all of Gaussian form. This essentially indi-

states that for a particle with $M \sim \langle p \rangle \sim 3T$ as it is for the charm quark at a temperature $T = 0.4 \text{ GeV}$, the evolution is not of Brownian type.

5. Azimuthal correlations of heavy quarks

In the initial hard scatterings heavy quark pairs are produced back-to-back at leading order due to momentum conservation and this leads to a back-to-back correlation in azimuthal angle. These produced heavy quarks pairs move in opposite direction and hence suffer different interaction. This would drastically alter their initial back-to-back correlation [19,20]. We have studied the azimuthal correlation of the $c\bar{c}$ pairs within both the Boltzmann and Langevin dynamics in a box. We initialize the $c\bar{c}$ pairs at the boundary of the box having momentum $p_x = p_z = 0$ and $p_y = 10 \text{ GeV}$. Hence the initial azimuthal correlation will be a delta around $d\phi = 0$. As a consequence of the interaction with the thermal bath this initial azimuthal correlation will broaden around $d\phi = 0$.

In Fig 3 the azimuthal correlation of $c\bar{c}$ within Langevin dynamics (left) and Boltzmann one (right) has been displayed at different momentum cuts. A larger spreading of momentum distribution in case of Boltzmann equation give rise a significant difference spreading of $c\bar{c}$ correlation at $d\phi = 0$ in comparison with the Langevin dynamics. This can be used as a observable in experiment at RHIC and LHC to study whether charm quark execute brownian motion or not.

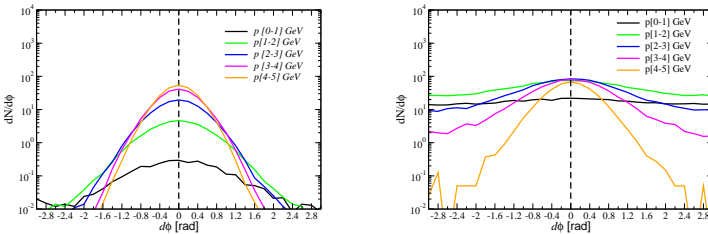


Fig. 3: Azimuthal correlation of $c\bar{c}$ within Boltzmann equation at different momentum cuts. Right: Langevin evolution; Left: Boltzmann evolution.

6. SUMMARY AND CONCLUSIONS

In this proceeding we have presented a study of the approximations involved by Langevin equation making a direct comparison with the full collisional integral within the framework of Boltzmann transport equation in a box at $T=0.4$ GeV. We have found that the Langevin approach is a good approximation for bottom quark whereas for charm quark Langevin approach deviates around 40% for the standard pQCD inputs. More specifically, we have found that the underlying dynamics of the single heavy quarks are indeed quite different between the Boltzmann and the Langevin approach and it does not appear to be simply a shift in momentum with a Gaussian fluctuations around it. As a consequence the Boltzmann approach gives rise to a larger spreading of $c\bar{c}$ correlation in comparison with the Langevin one at $d\phi = 0$.

1. R.Rapp and H van Hees, R. C. Hwa, X. N. Wang (Ed.) Quark Gluon Plasma 4, 2010, *World Scientific*, **111**
2. G. D. Moore, D Teaney, Phys. Rev. C **71**, 064904 (2005)
3. Hees H van, Greco V and Rapp R 2006 *Phys. Rev. C* **73**, 034913
4. S. Cao, S. A. Bass, Phys. Rev. C **84**, 064902 (2011)
5. H. Van Hees, M. Mannarelli, V. Greco and R. Rapp, Phys. Rev. Lett. **100**,192301 (2008)
6. P. B. Gossiaux, J. Aichelin, Phys. Rev. C **78** 014904 (2008)
7. A. Adare *et al.* (PHENIX Collaboration), Phys. Rev. Lett. **98**, 172301 (2007).
8. B. I. Abeleb *et al.* (STAR Collaboration), Phys. Rev. Lett. **98**, 192301 (2007).
9. B. Abelev *et al.*, (ALICE Collaboration) JHEP **1209** (2012) 112
10. S. K Das, J. Alam and P. Mohanty, Phys. Rev. C **82**, 014908 (2010)
11. W. M. Alberico *et al.*, Eur. Phys. J. C, **71** 1666 (2011)
12. B. Zhang, L. -W. Chen and C. -M. Ko, Phys. Rev. C **72** (2005) 024906
13. D. Molnar, Eur. Phys. J. C **49** (2007) 181
14. S. K. Das, F. Scardina, S. Plumari and V. Greco, arXiv:1309.7930 [nucl-th]
15. S. K. Das, F. Scardina, S. Plumari and V. Greco, Phys.Rev. C **90** 4, 044901 (2014)
16. G. Ferini, M. Colonna , M. Di Toro and V. Greco, Phys. Lett. B, **670**,325 (2009);
17. Z. Xu and C. Greiner, Phys. Rev. C **71**, 064901 (2005)

18. J. Uphoff, O. Fochler, Z. Xu and C. Greiner, Phys. Lett. B **717** (2012) 430
19. X. Zhu, N. Xu, P. Zhuang, 2008 Phys. Rev. Lett. **100**, 152301 (2008)
20. M. Nahrgang, J. Aichelin, P. B. Gossiaux and K. Werner, arXiv:1305.3823 [hep-ph]

Charmed Mesons near Chiral Symmetry Restoration

Chihiro Sasaki^{1,2}

¹ *Frankfurt Institute for Advanced Studies, D-60438 Frankfurt am Main, Germany,*

² *Institute of Theoretical Physics, University of Wrocław, PL-50204 Wrocław, Poland*

Abstract

Chiral thermodynamics of charmed mesons is formulated at finite temperature within a $2 + 1 + 1$ -flavored effective Lagrangian incorporating heavy quark symmetry. The chiral mass splittings are shown to be less sensitive to the light-quark flavors, attributed to the underlying heavy quark symmetry. Consequently, chiral symmetry restoration is more accelerated in the strange charmed-mesons than in the strange light mesons, and this is in striking contrast to the chiral $SU(4)$ result.

1. Introduction

Heavy flavors are produced at the initial stage of the high-energy heavy-ion collisions, so that they are expected to carry the dynamical history of a created matter, the Quark-Gluon Plasma (QGP). Recent experimental observations have revealed that charm quarks are thermalized [1–4], contrary to earlier anticipation. Charge fluctuations calculated in lattice QCD also indicate that the charmed mesons are deconfined together with light-flavor mesons [5]. Given those observations, comprehensive exploration for the chiral aspects of the heavy-light hadrons increases its importance.

In constructing effective Lagrangians for the heavy-light mesons, besides spontaneous chiral symmetry breaking, heavy quark symmetry is

a vital ingredient [6]. The pseudo-scalar D and vector D^* states fill in the same multiplet H , forming the lowest spin partners. Their low-energy dynamics is dominated by interactions with Nambu-Goldstone (NG) bosons, pions [7–10]. Introducing the multiplet including D and D^* inevitably accompanies another multiplet G which contains a scalar D_0^* and axial-vector D_1 states. Those parity partners, H and G , become degenerate when the chiral symmetry is restored [11, 12].

Aside from the chiral $SU(4)$ approach where the charm sector suffers from a huge explicit breaking of the extended flavor symmetry, a self-consistent study for the thermal charmed-mesons with implementing heavy quark symmetry has received little attention. In Ref. [13], a chiral effective theory for the light and heavy-light mesons has been formulated in the presence of a medium. Below, we will briefly discuss in-medium masses of the heavy-light mesons near the chiral crossover.

2. Chiral Effective Theory

When the charmed-meson mean fields are introduced to a chiral effective theory in the standard fashion, they act as an extra source which breaks the chiral symmetry explicitly. Consequently, an unrealistically strong mixing between the light-flavor and the charmed meson sector is induced. This defect can be avoided if effective interactions depending on temperature are introduced. Those intrinsic modifications can be extracted from the chiral condensates calculated in lattice QCD. The obtained coupling of the strange charmed meson to the sigma meson, $g_\pi^s(T)$, becomes quenched as temperature is increased toward the chiral pseudo-critical point $T_{pc} = 154$ MeV. Effective charmed-meson masses in hot matter are shown in Fig. 1. The parity partners approach each other as temperature is increased both in the non-strange and strange sector, in consistent with the chiral restoration. The two pseudo-scalar states have the same trend that their masses are increasing with temperature, although the non-strange meson mass exhibits a rather weak modification. On the other hand, the two scalar states drop significantly; the non-strange meson mass by ~ 200 MeV and the strange meson mass by ~ 100 MeV. The mass splittings between the non-strange and strange

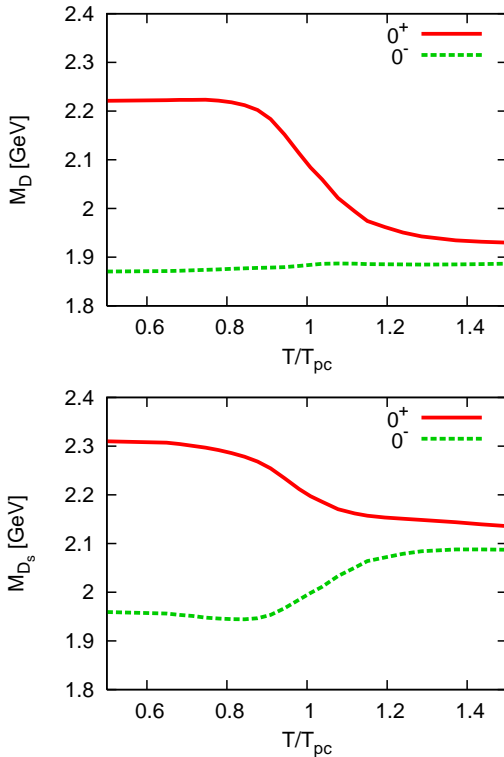


Fig. 1: In-medium masses of the non-strange (top) and strange (bottom) charmed-mesons with positive and negative parity [13].

states are around 200 MeV above T_{pc} due to the fact that the chiral symmetry in the strange sector is not restored yet. Nevertheless, the chiral mass splittings between the scalar and pseudo-scalar states are almost of the same size,

$$\delta M_D(T_{pc}) \sim \delta M_{D_s}(T_{pc}) \sim 200 \text{ MeV} , \quad (1)$$

i.e. *the chiral mass differences in the heavy-light sector are blind to the light flavors*. This is a striking difference from the chiral properties of the light mesons, and is attributed to the heavy quark symmetry possessed by the leading-order Lagrangian in $1/m_Q$ expansion. In contrast, the chiral SU(4) model, where the charmed mesons are treated on the equal

footing to the non-strange and strange mesons, yields a qualitatively different result from Eq. (1); δM_D is much smaller than δM_{D_s} , similar to the light meson masses [14].

3. Conclusions

The chiral mass splittings are shown to be essentially insensitive to the light-quark flavors, in spite of a non-negligible explicit breaking of the chiral $SU(3)$ symmetry. This “blindness” of the charm quark to the light degrees of freedom is dictated by the heavy quark symmetry. In contrast, the kaon and its chiral partner masses become degenerate at a higher temperature than T_{pc} , indicating a delay of the $SU(3)$ symmetry restoration. In the heavy-light sector, on the other hand, the strange charmed meson captures the onset of chiral symmetry restoration more strongly than the strange light meson does. The quenched $g_\pi^s(T)$ leads also to a strong suppression of the scalar D_s decay toward T_{pc} , on top of the suppression due to the small isospin violation. The same should be carried over to the B and B_s mesons with which the heavy quark symmetry is more reliable.

Within the same theoretical framework, thermal fluctuations and correlations between the light and heavy-light mesons have also been explored [15]. It is shown that various heavy-light flavor correlations indicate a remnant of the chiral criticality in a narrow range of temperature where the chiral susceptibility exhibits a peak. The onset of the chiral crossover, in the heavy-light flavor correlations, is therefore independent from the light flavors. This indicates that the fluctuations carried by strange charmed mesons can also be used to identify the chiral crossover, which is dominated by the non-strange light quark dynamics.

Acknowledgments

This work has been partly supported by the Hessian LOEWE initiative through the Helmholtz International Center for FAIR (HIC for FAIR), and by the Polish Science Foundation (NCN) under Maestro grant DEC-2013/10/A/ST2/00106.

-
1. A. Adare *et al.* [PHENIX Collaboration], Phys. Rev. C **84**, 044905 (2011).
 2. L. Adamczyk *et al.* [STAR Collaboration], arXiv:1404.6185 [nucl-ex].
 3. B. Abelev *et al.* [ALICE Collaboration], JHEP **1209**, 112 (2012).
 4. B. Abelev *et al.* [ALICE Collaboration], Phys. Rev. Lett. **111**, 102301 (2013).
 5. A. Bazavov, H.-T. Ding, P. Hegde, O. Kaczmarek, F. Karsch, E. Laermann, Y. Maezawa and S. Mukherjee *et al.*, Phys. Lett. B **737**, 210 (2014).
 6. N. Isgur and M. B. Wise, Phys. Lett. B **232**, 113 (1989); Phys. Lett. B **237**, 527 (1990).
 7. H. Georgi, Phys. Lett. B **240**, 447 (1990).
 8. M. B. Wise, Phys. Rev. D **45**, 2188 (1992).
 9. G. Burdman and J. F. Donoghue, Phys. Lett. B **280**, 287 (1992).
 10. T. M. Yan, H. Y. Cheng, C. Y. Cheung, G. L. Lin, Y. C. Lin and H. L. Yu, Phys. Rev. D **46**, 1148 (1992) [Erratum-ibid. D **55**, 5851 (1997)].
 11. M. A. Nowak, M. Rho and I. Zahed, Phys. Rev. D **48**, 4370 (1993).
 12. W. A. Bardeen and C. T. Hill, Phys. Rev. D **49**, 409 (1994).
 13. C. Sasaki, Phys. Rev. D **90**, no. 11, 114007 (2014).
 14. D. Roder, J. Ruppert and D. H. Rischke, Phys. Rev. D **68**, 016003 (2003).
 15. C. Sasaki and K. Redlich, arXiv:1412.7365 [hep-ph].



PACIAE 2.2, extended to cover lepton-nuclear and lepton-nucleus deep-inelastic scattering

Dai-Mei Zhou¹, Yu-Liang Yan², Xing-Long Li², Xiao-Mei Li²,
Bao-Guo Dong², Xu Cai¹, and Ben-hao Sa^{1,2}

¹ *Key Laboratory of Quark and Lepton Physics (MOE) and Institute of Particle Physics, Central China Normal University, Wuhan 430079, China.*

² *China Institute of Atomic Energy, P. O. Box 275 (10), Beijing, 102413 China.*

Abstract

The parton and hadron cascade model PACIAE 2.1 (cf. Comput. Phys. Commun. 184 (2013) 1476) has been upgraded to the new issue of PACIAE 2.2. By this new issue the lepton-nucleon and lepton-nucleus (inclusive) deep inelastic scatterings can be investigated. As an example, the PACIAE 2.2 model is enabled to calculate the specific charged hadron multiplicity in the $e^+ + p$ and $e^- + D$ semi-inclusive deep-inelastic scattering at 27.6 GeV electron beam energy. The calculated results are well comparing with the corresponding HERMES data. Additionally, the effect of model parameters α and β in the Lund string fragmentation function on the multiplicity is studied.

1. Introduction

The lepton inclusive and semi-inclusive deep inelastic scattering (DIS and SIDIS) off nuclear target are the most active frontiers between nuclear and the particle physics since the eighties of the last century. They have greatly contributed to the parton structure of hadron [1], the parametrization of parton distribution function (PDF) [2, 3], and the extraction of polarization-averaged fragmentation function (FF) [4, 5].

They also play important role in the hadronization of initial partonic state and the space-time evolution of the fragmentation process [5].

Two new electron ion collider (EIC) programs of the eRHIC at BNL and ELIC at Jefferson Laboratory (JLab) are evolved in the USA [6]. They are aimed at reaching the highly variable center of mass (cms) energies of $\sim 20 - 150$ GeV and the high collision luminosity of $\sim 10^{33-34}$ $\text{cm}^{-2}\text{s}^{-1}$. Meanwhile, a similar program of LHeC is also progressed at CERN in Europe [7]. The collision cms energy and luminosity of LHeC may achieve ~ 1 TeV and $\sim 10^{33}\text{cm}^{-2}\text{s}^{-1}$, respectively. Both the eRHIC (ELIC) and LHeC are able to yield great insight into the nucleon structure, such as how partons share the spin, mass, and magnetic moment of a nucleon, etc. To confront this expected new DIS era, an upgraded PACIAE 2.2 model, being able to investigate the l-p and l-A DIS, is introduced. For a reliable extraction of the FF with the quark fragmentation

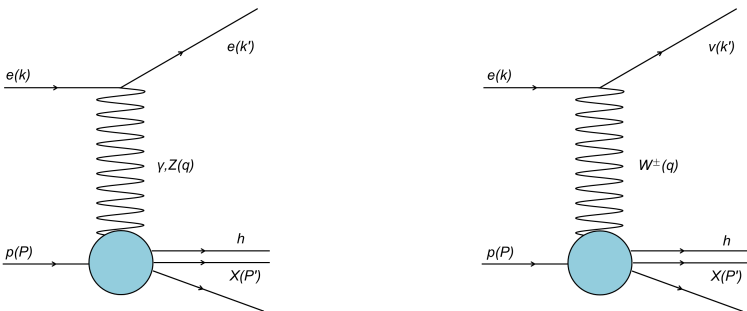


Fig. 1: (color online) Lowest order (Born approximation) Feynman diagram of the neutral current (NC) and charged current (CC) electron DIS.

function D_q^h , distinguished from the antiquark one, $D_{\bar{q}}^h$, the data of specific charged hadron (π^+ , π^- , K^+ , K^-) multiplicity in the unpolarized SIDIS are highly needed [4,8]. Recently, the HERMES collaboration has measured the multiplicity of charged pions and kaons in the 27.6 GeV electron beam SIDIS off proton and deuteron [8]. As an example, the PACIAE 2.2 model is employed for calculating the DIS normalized to π^+ , π^- , K^+ , and K^- multiplicities in the above electron SIDIS off proton and the deuteron. The calculated results are well comparing with the corresponding HERMES data [8].

2. Models

The PACIAE model [9] is based on PYTHIA [10]. However, the PYTHIA model is for high energy elementary collisions (e^+e^- , lepton-hadron, and hadron-hadron (hh) collisions) only, but PACIAE is for lepton-nucleus and nucleus-nucleus collisions also. In the PYTHIA model a hh collision, for instance, is decomposed into parton-parton collisions. The hard parton-parton collision is described by the LO-pQCD parton-parton interactions with the modification of parton distribution function in a hadron. The soft parton-parton collision, a non-perturbative process, is considered empirically. The initial- and final-state QCD radiations as well as the multiparton interactions are taken into account. So the consequence of a hh collision is a partonic multijet state composed of diquarks (anti-diquarks), quarks (antiquarks), and gluons, besides a few hadronic remnants. It is followed by the string construction and fragmentation, thus a final hadronic state is obtained for a hh (pp) collision finally.

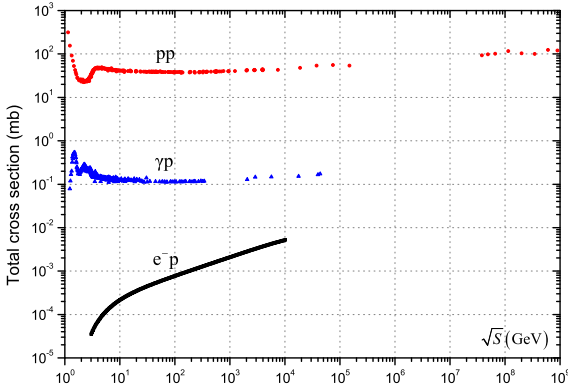


Fig. 2: (color online) pp , γp , and $e^- p$ (DID) total cross sections.

In the PACIAE model [9], the nucleons in a colliding nucleus are first randomly distributed according to the Woods-Saxon distribution in the

spatial space. The participant nucleons, resulted from Glauber model calculation, are required to be inside the overlap zone, formed when two colliding nuclei path through each other at a given impact parameter. The spectator nucleons are required to be outside the overlap zone but inside the nucleus-nucleus collision system. If the incident beam is in the z direction, we set $p_x = p_y = 0$ and $p_z = p_{beam}$ for the projectile nucleons, $p_x = p_y = p_z = 0$ for the target nucleons in the laboratory framework as well as $p_x = p_y = 0$ and $p_z = -p_{beam}$ for the target nucleons in the collider framework.

We then decompose a nucleus-nucleus collision into nucleon-nucleon (NN) collisions according to nucleon straight-line trajectories and the NN total cross section. Each NN collision is dealt by PYTHIA with the string fragmentation switched-off and the diquarks (anti-diquarks) broken into quark pairs (anti-quark pairs). A partonic initial state (composed of the quarks, antiquarks, gluons, and a few hadronic remnants) is obtained for a nucleus-nucleus collision after all of the NN collision pairs were exhausted.

This partonic initial stage is followed by a parton evolution stage. In this stage the parton rescattering is performed by the Monte Carlo method with $2 \rightarrow 2$ LO-pQCD cross sections [11]. The hadronization stage follows the parton evolution stage. The Lund string fragmentation model and a phenomenological coalescence model are provided for the hadronization. However, the string fragmentation model is selected in these calculations. The rescattering among produced hadrons is then dealt with the usual two body collision model [9]. In this hadronic evolution stage, only the rescatterings among π , K , $\rho(\omega)$, ϕ , p , n , Δ , Λ , Σ , Ξ , Ω , and their antiparticles are considered for simplicity.

PACIAE 2.2 has three versions: PACIAE 2.2a describing the relativistic elementary collision (pp, $\bar{p}p$, e^+e^- , and lepton-nucleon) and PACIAE 2.2b as well as PACIAE 2.2c describing the relativistic nuclear-nucleus collision (p+A and A+B) and lepton-nucleus DIS. In the PACIAE 2.2b model the partonic initiation, partonic rescattering, hadronization, and the hadronic rescattering are performed for each hh collision pairs independently until all the hh collision pairs are collided. Oppositely, in the PACIAE 2.2c, the partonic initiation is first performed for

all the hh collision pairs. This full initial partonic state is proceeded to the partonic rescattering stage, then the hadronization stage, and at last the hadronic rescattering stage. Therefore, PACIAE 2.2b and 2.2c are similar in the physical contents but are different in the topological structure.

For p+p and p+A (A+p) collisions, the overlap zone is not introduced presently. We deal the l+p and l+A DIS like the p+p and p+A collisions, respectively, but instead of the nucleon-nucleon cross section the lepton-nucleon DIS cross section is used. In the PYTHIA model, the e^-+p (e^++p), μ^-+p (μ^++p), and τ^-+p (τ^++p) DIS have two options of ' e^- ' (' e^+ '), ' μ^- ' (' μ^+ '), and ' τ^- ' (' τ^+ ') as well as ' $gamma/e^-$ ' ($gamma/e^+$), ' $gamma/\mu^-$ ' (' $gamma/\mu^+$ '), and ' $gamma/\tau^-$ ' (' $gamma/\tau^+$ '), respectively, in the specification of beam and target particle. However, the neutrino-nucleon (antineutrino-nucleon) DIS has only the first option. In order to be more consistent and to have a better running stability the first option is chosen for all the lepton-nucleon DIS in the PACIAE 2.2 model.

Fig. 1 shows the leading order (Born approximation) Feynman diagrams for the neutral current (NC, the exchange of γ/Z boson, left panel) and charged current (CC, the exchange of W^\pm boson, right panel) e^-+p DIS. There are two vertices in the left panel of Fig. 1, for instance. At the upper boson vertex the initial state QED and weak radiations have to be considered. At the lower boson vertex, not only the leading order parton level process of $V^*q \rightarrow q$ (V^* refers to $\gamma/Z/W$) but also the first order QCD radiation of $V^*g \rightarrow qg$ as well as the boson-gluon fusion process of $V^*g \rightarrow q\bar{q}$ have to be considered. Furthermore, the parton shower approach has been introduced to take higher than first order QCD effects into account [12]. Therefore the DIS cross section can be formally expressed as

$$\sigma_{NC(CC)} = \sigma_{NC(CC)}^{Born} (1 + \delta_{NC(CC)}^{qed}) (1 + \delta_{NC(CC)}^{weak}) (1 + \delta_{NC(CC)}^{gcd}) \quad (1)$$

[13], where $\sigma_{NC(CC)}^{Born}$ is the Born cross section, $\delta_{NC(CC)}^{gcd}$, $\delta_{NC(CC)}^{weak}$, and $\delta_{NC(CC)}^{qed}$ are, respectively, the QED, weak, and the QCD radiative corrections.

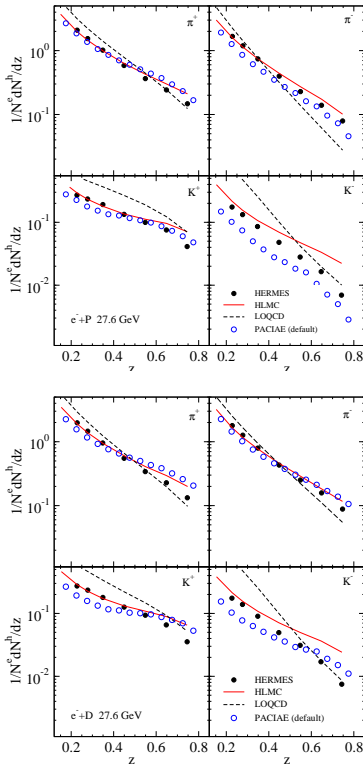


Fig. 3: (color online) Multiplicity of DIS normalized specific charged hadron as a function of z in the e^-+p (upper panel) and e^-+D (lower panel) DIS at 27.6 GeV electron beam energy.

In the lowest-order perturbative QCD theory, the NC/CC DIS Born cross section of the unpolarized electron on an unpolarized nucleon can be expressed by the structure functions F_1, F_2, F_3 as follows [14]

$$\begin{aligned}
 \frac{d^2\sigma_I}{dx dy} &= \frac{4\pi\alpha^2}{xyQ^2}\eta^I \left(\left(1 - y - \frac{x^2 y^2 M^2}{Q^2} \right) F_2^I + y^2 x F_1^I \right) \\
 &\mp \frac{4\pi\alpha^2}{xyQ^2}\eta^I \left(\left(y - \frac{y^2}{2} \right) x F_3^I \right)
 \end{aligned} \tag{2}$$

where the mass of the incident and scattered leptons are neglected. In the above equation, I denotes NC or CC . α stands for the fine structure

constant. $x \equiv x_B$ and y are the Bjorken scaling variable and fraction energy of $\gamma/Z/W$ boson, respectively. Q^2 is the negative squared 4-momentum transfer. M refers to the mass of target nucleon. $\eta^{NC} = 1$, $\eta^{CC} = (1 \pm \lambda)^2 \eta_W$, and

$$\eta_W = \frac{1}{2} \left(\frac{G_F M_W^2}{4\pi\alpha} \frac{Q^2}{Q^2 + M_W^2} \right) \quad (3)$$

$$G_F = \frac{e^2}{4\sqrt{2}\sin^2\theta_W M_W^2} \quad (4)$$

where M_W and θ_W are the mass of W boson and the Weinberg angle, respectively. $\lambda = \pm 1$ is the helicity of the incident lepton.

The structure functions above can be expressed by the parton distribution function of nucleon in the quark-parton model [15]. Presently we can not calculate PDF from the first principles and PDF can only be extracted from the QCD fits with a measure of the agreement between the experimental data of lepton-nucleon DIS cross sections and the theoretical models [16]. With the PDFs at hand, we are able to calculate the lepton-nucleon DIS cross section. The black curve in Fig. 2 gives the unpolarized e^-+p DIS total cross section calculated with HERA-PDF1.5 LO [17] PDF set [18]. In the calculation the cuts are first set for $Q^2 > 1$ GeV and $W^2 > 1.96$ GeV (W^2 is the squared invariant mass of the photon-nucleon system) and then the cuts in x and y are derived according to the relationships among kinematic variables and $\cos^2\theta \leq 1$. The red and blue data points in Fig. 2 are, respectively, the total cross section of pp and γp collisions copied from [14].

One knows well that the incident proton, in the p+Au collisions at RHIC energies for instance, may collide with a few ($\sim 2-5$) nucleons when it passes through the gold target. Since the e^-+p DIS total cross section is a few order of magnitude smaller than the pp collision at the range of $\sqrt{s} < 1000$ GeV (cf. Fig. 2), one may expect that the incident electron, in this energy range, may suffer at most one DIS with the nucleon when it passes through the target nucleus. The struck nucleon is the one with lowest approaching distance from the incident electron. This is the same for other incident leptons because the lepton-nucleon DIS total cross section is not so much different among the different leptons [18].

Therefore in the pioneer studies [19] for the lepton-nucleus DIS by PYTHIA + BUU transport model, the FRITIOF 7.02 model [20] or PYTHIA 6.2 [21] was employed to generate a lepton-nucleon DIS event. The generated hadronic final state was then input into the BUU (Boltzmann-Uehling-Uhlenbeck) equation [22] considering the final state hadronic interaction (hadronic rescattering). This PYTHIA + BUU transport model successfully described the HERMES data of the ratio of DIS normalized charged hadron multiplicity in the lepton-A (nucleus) DIS to the one in the lepton-deuteron DIS, for the 27.5 GeV electron beam energy $e^+ + {}^{14}\text{N}$ and $e^+ + {}^{84}\text{Kr}$ DIS [23].

3. Results

As mentioned in [8,24] the measured hadron multiplicity in SIDIS has first to be corrected for the radiative effects, the limitations in geometric acceptances, and the detector resolution. The Born-level multiplicity is then obtained. Therefore, the DIS (total yield) normalized Born-level multiplicity of the h type hadrons as a function of z (the fractional energy of hadron h) in the lepton SIDIS off a nuclear target can be expressed as

$$\frac{1}{N_{DIS}} \frac{dN^h}{dz} = \frac{1}{N_{DIS}} \int d^5 N^h(x_B, Q^2, z, P_{h\perp}, \phi_h) dx_B dQ^2 dP_{h\perp} d\phi_h \quad (5)$$

[8], where N_{DIS} refers to the DIS total yield, $P_{h\perp}$ is the component of the hadron momentum P_h , transverse to q (the 4-momentum of the mediator $\gamma/Z/W$) and ϕ_h stands for the azimuthal angle between the lepton scattering plane and the hadron production plane. Thus one may compare the calculated $\frac{1}{N_{DIS}} \frac{dN^h}{dz}$ in the full kinematic phase space with the HERMES data, like done in [8,24].

In the PACIAE 2.2 model simulations, the model parameters are all fixed the same as the default values given in PYTHIA. Figure 3 gives the comparison of the HERMES $\frac{1}{N_{DIS}} \frac{dN^h}{dz}$ data (solid circles) [8] to the corresponding results of the PACIAE 2.2 model (open circles), HLMC (solid line), and the LOQCD (dashed line). Here HLMC refers to the HERMES Lund Monte Carlo. HLMC is a combination of the DIS event generator Lepto [12] based on JETSET 7.4 and PYTHIA

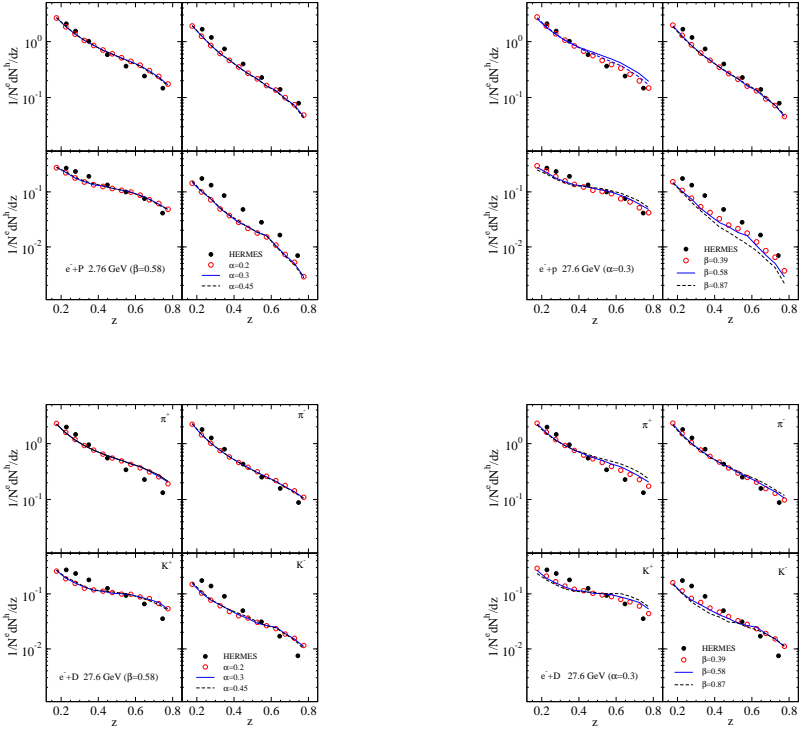


Fig. 4: (color online) The effect of parameter α (left panels) and β (right panels) in the Lund string fragmentation function on $\frac{1}{N_{DIS}} \frac{dN^h}{dz}$ in the $e^- + p$ (upper panels) and $e^- + D$ (lower panels) DIS at 27.6 GeV electron beam energy.

5.7 [25], the detector simulation program based on GEANT [26], and the HERMES reconstruction program [24]. The HLMC results in Fig. 3 were calculated with fitting thirteen model parameters to the multiplicity as a function of z , p_T (transverse momentum), and η (pseudorapidity) of the π^- , K^- , and \bar{p} [24]. The LOQCD results in Fig. 3 were calculated in the framework of collinear factorization at the leading order perturbative QCD [8, 27]. In Fig. 3 one sees that the default PACIAE fairly well reproduces the HERMES data. Meanwhile, the effect of α and β parameters in the Lund string fragmentation function [10]

$$f(\hat{z}) \propto \frac{1}{\hat{z}} (1 - \hat{z})^\alpha \exp\left(-\frac{\beta m_T^2}{\hat{z}}\right) \quad (6)$$

T a b l e 1: DIS normalized multiplicity of π^+ , π^- , K^+ and K^- in the e^-+p DIS.

Effect of α with default $\beta=0.58$					Effect of β with default $\alpha=0.3$				
α	π^+	π^-	K^+	K^-	β	π^+	π^-	K^+	K^-
0.2	1.331	0.9591	0.1164	0.04406	0.39	1.355	0.9834	0.1204	0.04828
0.3	1.339	0.9666	0.1177	0.04646	0.58	1.339	0.9666	0.1177	0.04646
0.45	1.351	0.9785	0.1196	0.04732	0.87	1.315	0.9419	0.1132	0.04161

T a b l e 2: DID normalized multiplicity of π^+ , π^- , K^+ and K^- in the e^-+D DIS.

Effect of α with default $\beta=0.58$					Effect of β with default $\alpha=0.3$				
α	π^+	π^-	K^+	K^-	β	π^+	π^-	K^+	K^-
0.2	1.314	1.364	0.1203	0.05538	0.39	1.351	1.407	0.1269	0.06116
0.3	1.326	1.383	0.1219	0.05696	0.58	1.326	1.383	0.1219	0.05696
0.45	1.345	1.399	0.1239	0.05919	0.87	1.288	1.342	0.1161	0.05192

on the multiplicity is investigated. In the above equation \hat{z} refers to the fraction lightcone variable taken by the fragmented hadron out of the fragmenting particle and $m_T^2 = p_T^2 + m_0^2$ where m_0 refers to the rest mass of the fragmented hadron. The results are given in the tables 1 and 2 as well as in figure 4. We see here that the multiplicity increases (decreases) with α (β) increasing. The effect shown in the differential observable $\frac{1}{N_{DIS}} \frac{dN^h}{dz}$ is weak but visible, as shown in Figs 4.

4. Conclusions

In summary, we have upgraded the the parton and hadron cascade model PACIAE 2.1 to a new issue PACIAE 2.2 involving the lepton-nucleon and lepton-nucleus DIS. The PACIAE 2.2 is then employed investigating the DIS normalized specific charged hadron multiplicity as function of z , $\frac{1}{N_{DIS}} \frac{dN^h}{dz}$, in the 27.6 GeV electron beam energy e^-+p and e^-+D SIDIS. The PACIAE 2.2 results calculated with default parameters reproduce fairly well the corresponding HERMES data [8].

Additionally, we have investigated the effect of model parameters α and β in the Lund string fragmentation function. It turned out that

the particle multiplicity increases (decreases) with α (β) increasing. The effect on the global observable yield is not small, but on the differential observable of $\frac{1}{N_{DIS}} \frac{dN^h}{dz}$ is just visible. These effects are expected to be increased with increasing reaction energy and system size.

Acknowledgments

This work was supported by the National Natural Science Foundation of China under grant Nos.:11075217, 11105227, 11175070, 11477130 and by the No. 111 project of the foreign expert bureau of China. BHS would like to thank C. P. Yuan for HERAFitter, G. Schnell for HERMES data, and Y. Mao and S. Joosten for discussions.

1. Xiangdong Ji, Nucl. Phys. B **402**, 217 (1993).
2. R. Placakyte, arXiv:1111.5452 v4 [hep-ph].
3. Klaus Rith, arXiv:1402.5000v1.
4. E. Leader, A. V. Sidorov, and D. B. Stamenov, arXiv:1312.5200v1.
5. A. Airapetian, et al., HERMES Collaboration, Nucl. Phys. B **780**, 1 (2007).
6. White paper writing committee, Electron ion collider: The next QCD frontier, arXiv:1212.1701v2 [nucl-ex].
7. LHeC study group, A Large Hadron electron Collider at CERN, arXiv:1206.2913 [physics.acc-ph]; arXiv:1211.4831v1 [hep-ex].
8. A. Airapetian, et al., HERMES Collaboration, Phys. Rev. D **87**, 074029 (2013).
9. Ben-Hao Sa, Dai-Mei Zhou, Yu-Liang Yan, Bao-Guo Dong, and Xu Cai, Comput. Phys. Commun. **184**, 1476 (2013); Ben-Hao Sa, Dai-Mei Zhou, Yu-Liang Yan, Xiao-Mei Li, Sheng-Qin Feng, Bao-Guo Dong, and Xu Cai, Comput. Phys. Commun. **183**, 333 (2012).
10. T. Sjöstrand, S. Mrenna, and P. Skands, JHEP **05**, 026 (2006).
11. B. L. Combridge, J. Kripfgang, and J. Ranft, Phys. Lett. B **70**, 234 (1977).
12. G. Ingelman, A. Edin, and J. Rathsman, Comput. Phys. Commun. **101**, 108 (1997).
13. C. Adloff, et. al., H1 Collaboration, Eur. Phys. J. C **19**, 269 (2001).
14. Review of Particle Physics, Phys. Rev. D **86**, 1 (2012).
15. J. D. Bjorken and E. A. Paschos, Phys. Rev. **185**, 1975 (1969); R. P. Feynman, Photon hadron interactions, Benjamin, New York, 1972.

-
16. A. Gizhko, HERAFitter, Nucl. Phys. B, Proceedings Supplements, 2013, 245: 161-163 (<http://herafitter.org>); M. R. Wysley, D. Bourilkov, and R. C. Group, arXiv: hep-ph/0508110v1.
 17. H1 and ZEUS Collaborations, H1prelim-13-141 and ZEUS-prel-13-003.
 18. Xing-Long Li, Yu-Liang Yan, Xiao-Mei Li, Dai-Mei Zhou, Xu Cai, and Ben-Hao Sa, Systematic study of the differential and total cross sections as well as the final hadron multiplicity in the lepton-nuclear collisions, in preparation.
 19. T. Fatler, W. Cassing, K. Gallmeister, and U. Mosel, Phys. Lett. B **594**, 61 (2004); T. Fatler, W. Cassing, K. Gallmeister, and U. Mosel, Phys. Rev. C **70**, 054609 (2004); K. Gallmeister, and U. Mosel, Nucl. Phys. A **801**, 68 (2008).
 20. Hong Pi, Comput. Phys. Commun. **71**, 173 (1992).
 21. T. Sjöstrand, et. al., Comput. Phys. Commun. **135**, 238 (2001).
 22. T. Fatler, K. Gallmeister, and U. Mosel, Phys. Rev. C **67**, 054606 (2003).
 23. HERMES Collab., Eur. Phys. J. C **20**, 479 (2001); V. Muccifora, HERMES Collab., Nucl. Phys. A **771**, 254c (2002).
 24. A. Hillenbrand, Ph.D. thesis: DESY-THESIS-2005-035,2005.
 25. T. Sjöstrand, Comput. Phys. Commun. **82**, 74 (1994).
 26. R. Brun, R. Hagelberg, M. Hansroul, and J. C. Lassalle, GEANT: Simulation program for particle physics experiments. User guide and reference manual, (1978), CERN-DD-78-2 Rev.
 27. S. Kretzer, Phys. Rev. D **62**, 054001 (2000).

The specific charged hadron multiplicity in $e^- + p$ and $e^- + D$ semi-inclusive deep-inelastic scattering

Ben-Hao Sa^{1,2}, Yu-Liang Yan¹, Xing-Long Li¹, Xiao-Mei Li¹,
Dai-Mei Zhou², Yun Cheng², Bao-Guo Dong¹, and Xu Cai²

¹ *China Institute of Atomic Energy, P. O. Box 275 (10), Beijing, 102413 China.*

² *Key Laboratory of Quark and Lepton Physics (MOE) and Institute of Particle Physics, Central China Normal University, Wuhan 430079, China.*

Abstract

The PYTHIA 6.4 model and the extended parton and hadron cascade model PACIAE 2.2 are utilized to comparatively investigate the DIS normalized specific charged hadron multiplicity in the electron semi-inclusive deep-inelastic scattering off proton and deuteron at 27.6 GeV beam energy. The PYTHIA and PACIAE results calculated with default model parameters not well and fairly well reproduce the corresponding HERMES data, respectively. In addition, we have studied the effects of the differences between the PYTHIA and PACIAE models on the multiplicity.

1. Introduction

Since the eighties of last century the lepton inclusive and semi-inclusive deep inelastic scattering (DIS and SIDIS) off nuclear target have become one of the most active frontiers between the nuclear and particle physics. They have greatly contributed to the partonic structure of hadron [1], the parametrization of parton distribution function (PDF) [2], and the nuclear medium effect on PDF (EMC effect) [3]. They also play important

role in the hadronization of initial partonic state, the space-time evolution of the fragmentation process, and the extraction of polarization-averaged fragmentation function (FF) [4, 5].

The multiplicity data of specific charged hadron (π^+ , π^- , K^+ , K^-) in the unpolarized SIDIS are crucial for distinguishing the quark fragmentation function of $D_q^h(z, Q^2)$ from the antiquark one of $D_{\bar{q}}^h(z, Q^2)$ (z and Q^2 are defined in Tab. 1 where the kinematic variables often used in DIS are listed). Thus those multiplicity data are important for a reliable extraction of the FF. Recently, the HERMES collaboration has measured the charged pions and kaons multiplicity in the 27.6 GeV electron SIDIS off proton and deuteron [6]. Meanwhile, they have compared their DIS normalized data to the HERMES Lund Monte Carlo (HLMC) simulations with thirteen model parameters tuned to the multiplicity as a function of z , p_T (hadron transverse momentum), and η (hadron pseudorapidity) of the π^- , K^- , and \bar{p} [6, 7]. HLMC is a combination of the DIS event generator Lepto [8] (based on JETSET 7.4 and PYTHIA 5.7 [9]), the detector simulation program (based on GEANT [10]), and the HERMES reconstruction program [7].

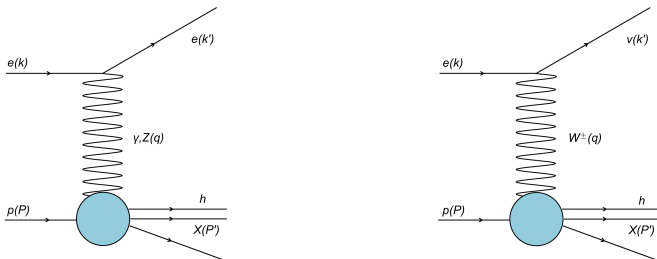


Fig. 1: (color online) Leading order (Born approximation) Feynman diagram of the neutral current (NC, left panel) and charged current (CC, right panel) $e^- + p$ DIS.

In this paper the PYTHIA 6.4 [11] model and on which based model of PACIAE 2.2 [12] (simplified as PYTHIA and PACIAE, respectively, later) are employed to calculate the DIS normalized π^+ , π^- , K^+ , and K^- multiplicities in the 27.6 GeV electron SIDIS off the proton and deuteron targets. The PACIAE 2.2 model is a new issue of the PACIAE model updated presently from PACIAE 2.1 [13] in order to cover the lepton-nucleon and lepton-nucleus DIS (SIDIS). The DIS normalized specific

T a b l e 1: Kinematic variables in the lepton-nucleon DIS.

$k = \left(E, \vec{k} \right), k' = \left(E', \vec{k}' \right)$	incident, scattered lepton 4-momentum
$P \stackrel{\text{lab}}{\equiv} \left(M, \vec{0} \right)$	4-momentum of the target nucleon
$q = k - k'$	squared 4-momentum transfer (4-momentum of the virtual photon)
$Q^2 = -q^2 \stackrel{\text{lab}}{\approx} 4EE' \sin^2 \left(\frac{\theta}{2} \right)$	Negative squared 4-momentum transfer
$\nu = \frac{P \cdot q}{M} \stackrel{\text{lab}}{\equiv} E - E'$	Energy transfer to the target nucleon
$W^2 = (P + q)^2$	Squared invariant mass of the photon-nucleon system
$y = \frac{P \cdot q}{P \cdot k} \stackrel{\text{lab}}{\equiv} \frac{\nu}{E}$	Fractional energy of the virtual photon (inelasticity)
$z = \frac{P \cdot P_h}{P \cdot q} \stackrel{\text{lab}}{\equiv} \frac{E_h}{\nu}$	Fractional energy of hadron h
$x_B = \frac{Q^2}{2P \cdot q} \stackrel{\text{lab}}{\equiv} \frac{Q^2}{2M \cdot \nu}$	Bjorken scaling variable
ϕ_h	Azimuthal angle between the lepton scattering plane and the hadron production plane
$P_{h\perp} \stackrel{\text{lab}}{\equiv} \frac{ \vec{q} \times \vec{P}_h }{ \vec{q} }$	Component (transverse to q) of the hadron momentum (P_h)

charged hadron multiplicity as a function of z in the e^-+p and e^-+D SIDIS at 27.6 GeV beam energy calculated by PYTHIA and PACIAE with default model parameters is not well and fairly well consistent with the HERMES data [6], respectively. The default PYTHIA results in e^-+D SIDIS is calculated as the average of the default PYTHIA results in e^-+p and e^-+n (neutron) SIDIS at the same beam energy.

2. Models

The PACIAE model [13] is based on PYTHIA [11]. However, the PYTHIA model is for high energy elementary collision (e^+e^- , hadron-hadron (hh) collisions, and lepton-hadron DIS) but PACIAE is also for lepton-nuclear and nuclear-nuclear collisions. In the PYTHIA model a hh collision, for instance, is described in term of parton-parton collisions. The hard parton-parton collision is dealt by the LO-pQCD parton-parton cross section with the modification of parton distribution function in a hadron. The soft parton-parton collision, a non-perturbative process, is consid-

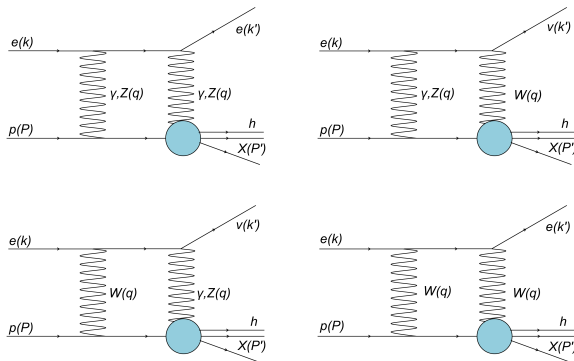


Fig. 2: (color online) Next to leading order Feynman diagrams of NC and CC $e^- + p$ DIS.

ered empirically. The initial- and final-state QCD radiations as well as the multiparton interactions are taken into account. So the consequence of a hh collision is a partonic multijet state composed of the diquarks (anti-diquarks), quarks (antiquarks), and the gluons, besides a few hadronic remnants. It is followed by the string construction and fragmentation, thus a final hadronic state is obtained for a hh (pp) collision eventually.

In the PACIAE model, the nucleons in a colliding nucleus are first randomly distributed in the spatial coordinate space according to the Woods-Saxon distribution. The participant nucleons, resulted from Glauber model calculation for a nucleus-nucleus collision, are required to be inside the overlap zone, formed when two colliding nuclei path through each other at a given impact parameter. The spectator nucleons are required to be outside the overlap zone but inside the nucleus-nucleus collision system. If the beam direction is set on z axis, then $p_x = p_y = 0$ and $p_z = p_{beam}$ are set for nucleons in the projectile for both the fixed target and collider. $p_x = p_y = p_z = 0$ and $p_x = p_y = 0$ as well as $p_z = -p_{beam}$ are set for nucleons in the target for both the fixed target and collider, respectively.

A nucleus-nucleus collision is then decomposed into nucleon-nucleon (NN) collision pairs according to the nucleon straight-line trajectories and the NN total cross section. Each NN collision is dealt by PYTHIA

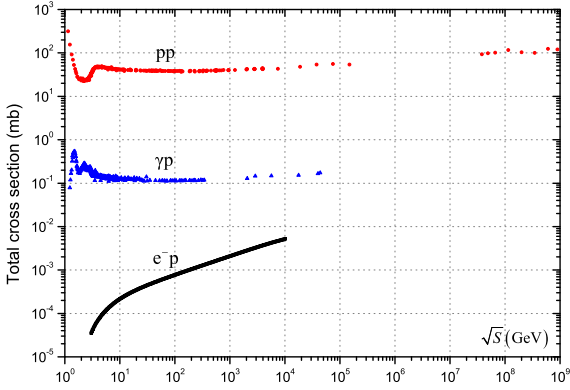


Fig. 3: (color online) The total cross section of pp and γp collisions as well as leading order e^-p DIS.

with string fragmentation switched-off and diquarks (anti-diquarks) broken into quarks (anti-quarks). A partonic initial state (composed of the quarks, antiquarks, gluons, and a few hadronic remnants) is obtained for a nucleus-nucleus collision after all the NN collision pairs were collided.

This partonic initial stage is followed by a parton evolution stage. In this stage, the partonic rescattering is performed by the Monte Carlo method with $2 \rightarrow 2$ LO-pQCD parton-parton cross sections [14]. The hadronization stage follows the parton evolution stage. The Lund string fragmentation model and a phenomenological coalescence model are provided for the hadronization. However, the string fragmentation model is selected in the present calculations.

Then the rescattering among produced hadrons is dealt with usual two body collision model [13]. In this hadron evolution stage, only the rescatterings among π , K , $\rho(\omega)$, ϕ , p , n , Δ , Λ , Σ , Ξ , Ω , and their antiparticles are considered for the simplicity.

For $p+p$ and $p+A$ ($A+p$) collisions, the overlap zone is not introduced presently. We deal with the $l+p$ ($l+n$) and $l+A$ DIS (SIDIS) like the $p+p$ and $p+A$ collisions, respectively. However, instead of the NN total cross section, the lepton-nucleon DIS total cross section is used

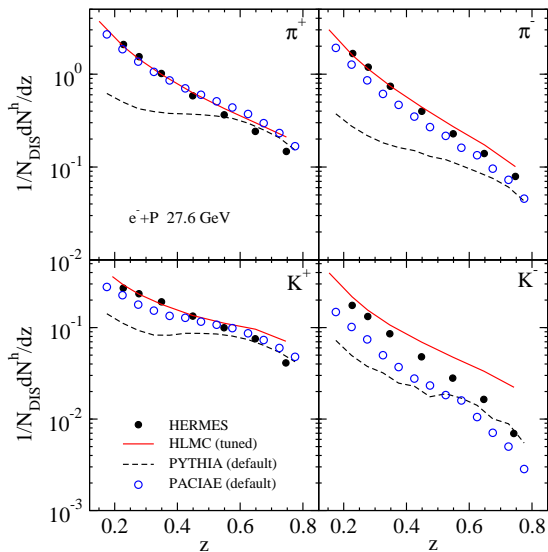


Fig. 4: (color online) Multiplicity of DIS normalized specific charged hadron as a function of z in the e^-+p SIDIS at 27.6 GeV beam energy.

and the lepton is assumed not resolvable in the PYTHIA and PACIAE models.

Fig. 1 shows the leading order (Born approximation) Feynman diagram for the neutral current (NC, the exchange of γ/Z boson, left panel) and charged current (CC, the exchange of W^\pm boson, right panel) e^-+p DIS. The next to leading order contribution (as shown in Fig. 2) and the higher order contributions are usually negligible [15].

There are two vertices in the left panel of Fig. 1, for instance. At the upper boson vertex the initial state QED and weak radiations have to be considered. At the lower boson vertex, not only the leading order parton level process of $V^*q \rightarrow q$ (V^* refers to $\gamma/Z/W$) but also the first order QCD radiation of $V^*g \rightarrow qg$ as well as the boson-gluon fusion process of $V^*g \rightarrow q\bar{q}$ have to be introduced. Furthermore, the parton shower approach has been introduced to take higher than first order QCD effects into account [8]. Therefore the DIS cross section can be formally

expressed as

$$\sigma_{NC(CC)} = \sigma_{NC(CC)}^{Born} (1 + \delta_{NC(CC)}^{qed}) (1 + \delta_{NC(CC)}^{weak}) (1 + \delta_{NC(CC)}^{qcd}) \quad (1)$$

[15], where $\sigma_{NC(CC)}^{Born}$ is the Born cross section, $\delta_{NC(CC)}^{qed}$ and $\delta_{NC(CC)}^{weak}$ are, respectively, the QED and weak radiative corrections, the QCD radiative correction of $\delta_{NC(CC)}^{qcd}$ is formally introduced in this paper. In the lowest-order perturbative QCD theory, the NC/CC DIS Born cross section of the unpolarized electron on an unpolarized nucleon can be expressed by the structure functions F_1, F_2, F_3 as follows [16]

$$\begin{aligned} \frac{d^2\sigma_I}{dx dy} &= \frac{4\pi\alpha^2}{xyQ^2} \eta^I \left(\left(1 - y - \frac{x^2 y^2 M^2}{Q^2} \right) F_2^I + y^2 x F_1^I \right) \\ &\mp \frac{4\pi\alpha^2}{xyQ^2} \eta^I \left(\left(y - \frac{y^2}{2} \right) x F_3^I \right) \end{aligned} \quad (2)$$

where the mass of the initial and scattered leptons are neglected. In the above equation, I denotes NC or CC . $x \equiv x_B$ and y are the Bjorken scaling variable and fraction energy of $\gamma/Z/W$ boson (cf. Tab. 1), respectively. α stands for the fine structure function, M for the mass of target nucleon. $\eta^{NC} = 1$, $\eta^{CC} = (1 \pm \lambda)^2 \eta_W$, and

$$\eta_W = \frac{1}{2} \left(\frac{G_F M_W^2}{4\pi\alpha} \frac{Q^2}{Q^2 + M_W^2} \right) \quad (3)$$

$$G_F = \frac{e^2}{4\sqrt{2} \sin^2 \theta_W M_W^2} \quad (4)$$

where M_W and θ_W are the mass of W boson and Weinberg angle, respectively. $\lambda = \pm 1$ is the helicity of the incident electron.

The structure functions above can be expressed by the parton distribution function of nucleon in the quark-parton model [17]. Although the PDF can not be calculated by first principle, it can be extracted from the QCD fits by a measure of the agreement between the experimental data of lepton-nucleon DIS cross section and the theoretical models [18]. The $e^- + p$ DIS total cross section calculated with HERAPDF1.5 LO [19]

PDF set, is given in Fig. 3 by black curve [20]. The red and blue circles in this figure are, respectively, the total cross section of pp and γp collisions copied from [16]. One knows well that the incident proton, in the p+Au collisions at RHIC energies for instance, may collide with a few (~ 3 -5) nucleons when it passes through the gold target. Since the e^-+p DIS total cross section is a few order of magnitude small than pp collision at the \sqrt{s} range of $\sqrt{s} < 1000$ GeV, one may expect that the incident electron, in this energy range, may suffer at most one DIS with the nucleon when it passes through the target nucleus. The struck nucleon is the one with lowest approaching distance from the incident electron. This is the same for other incident leptons because the DIS total cross section is not so much different among the different leptons [20].

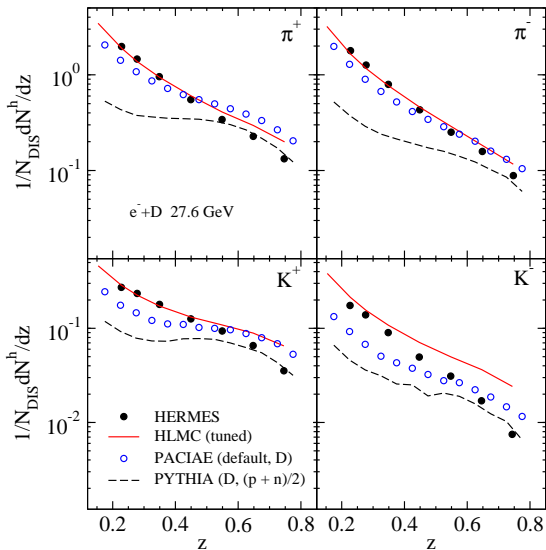


Fig. 5: (color online) Multiplicity of DIS normalized specific charged hadron as a function of z in the e^-+D SIDIS at 27.6 GeV beam energy.

3. Results

As mentioned in [6, 7] the measured hadron multiplicity in the e^-+p and e^-+D SIDIS at 27.6 GeV beam energy has first to correct for the

radiative effects, limitations in geometric acceptances, and the detector resolution. The Born-level multiplicity is then obtained in order to benefit the PDF extraction, etc. Then they normalized this Born-level multiplicity by the total DIS yield to reduce the uncertainties in the corrections above. This is of benefit to the comparison among the different experimental measurements and between the experiment and theory. The Born-level multiplicity of the type h hadrons as a function of z in the lepton SIDIS off a nuclear target, for instance, can be expressed as

$$\frac{1}{N_{DIS}} \frac{dN^h}{dz} = \frac{1}{N_{DIS}} \int d^5 N^h(x_B, Q^2, z, P_{h\perp}, \phi_h) dx_B dQ^2 dP_{h\perp} d\phi_h. \quad (5)$$

Therefore, we can compare the default PYTHIA and PACIAE results of $\frac{1}{N_{DIS}} \frac{dN^h}{dz}$ calculated in the full kinematic phase space to the DIS normalized HERMES data, like in [6, 7].

In the default PYTHIA and PACIAE model simulations, the model parameters are unchanged. The default PYTHIA (black dashed line) and PACIAE (blue open circles) results of $\frac{1}{N_{DIS}} \frac{dN^h}{dz}$ are compared with the HERMES data (black solid circles) as well as the results of HLMC (black line) in the Figure 4 for π^+ (upper left panel), π^- (upper right), K^+ (lower left), and K^- (lower right) in the e^-+p SIDIS at the 27.6 GeV beam energy. One sees in this figure that the default PACIAE results reproduce HERMES data nearly as good as HLMC (with thirteen tuned model parameters). However, the default PYTHIA results disagree with HERMES data. Figure 5 is the same as Fig. 4 but for e^-+D SIDIS at the same beam energy. For Fig. 5 one may draw a similar conclusion like Figure 4.

Table 2 lists the discrepancies between the PYTHIA and PACIAE models. In the event generation there is no extra requirement in the PYTHIA model but is requirement of having one parton (quark, anti-quark, or gluon) at least in each event in the PACIAE model. In the Figs. 6 and 7, the black dashed line is the default PYTHIA results, the blue circles are the default PACIAE results, and the red dash-dotted line is the results of PACIAE without both the PRS and HRS rescatterings. The later two are close to each other, which really proves the small effect of both the PRS and HRS in the e^-+p and e^-+D SIDIS, because the reaction systems here are quite small.

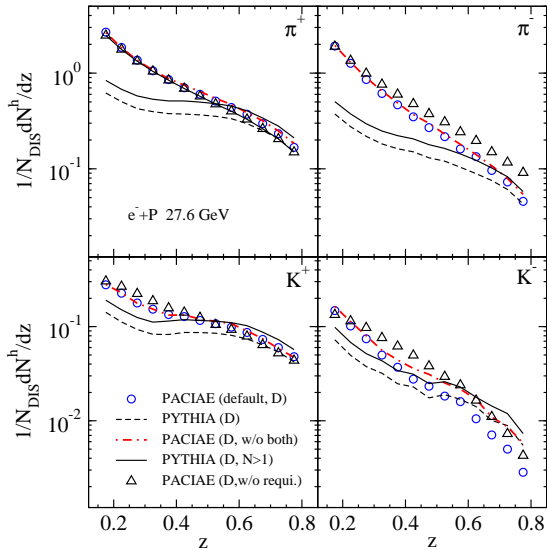


Fig. 6: (color online) Multiplicity of DIS normalized specific charged hadron as a function of z in the e^-+p SIDIS at 27.6 GeV beam energy.

The black open triangles, in the figures 6 and 7, are the default PACIAE results calculated without the requirement of having one parton at least in each generated event. These results are not different so much from the blue open circles (default PACIAE results calculated with event requirement). Thus the initial partonic state, introduced in the PACIAE model but not in PYTHIA, should be the main reason of the large discrepancy between the default PYTHIA and PACIAE results. This difference causes the dynamical simulation process in the PACIAE model is quite different from the one in the PYTHIA model.

In the Figures 6 and 7 the black solid lines are calculated by the default PYTHIA model with the requirement of having one pion or kaon at least in each generated event. One sees here that the default PYTHIA results with the requirement (black solid line) is considerably larger than the one without the requirement (black dashed line). It may mean the event generated by the default PYTHIA is not completely DIS, which has to be study further.

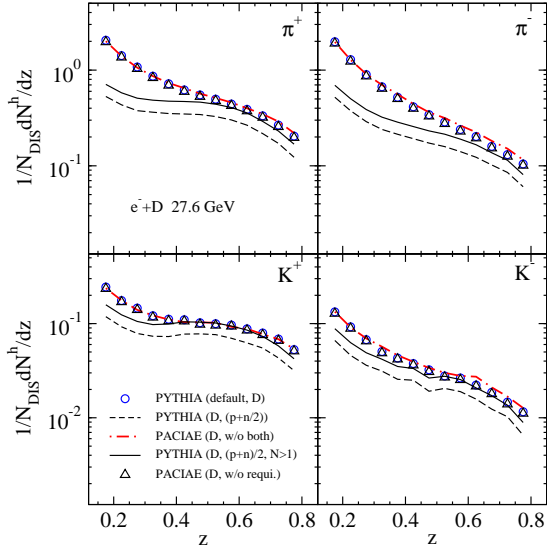


Fig. 7: (color online) Multiplicity of DIS normalized specific charged hadron as a function of z in the e^-+D SIDIS at 27.6 GeV beam energy.

4. Conclusion

In summary, We have employed the PYTHIA 6.4 and the extended parton and hadron cascade model PACIAE 2.2 to investigate the DIS normalized specific charged hadron multiplicity, $\frac{1}{N_{DIS}} \frac{dN^h}{dz}$, measured by HERMES in the e^-+P and e^-+D SIDIS at 27.6 GeV beam energy. The PYTHIA and PACIAE results, calculated with default model parameters, not well and fairly well reproduce the HERMES data [6], respectively.

Additionally, we have investigated the effects of the differences between the PYTHIA and PACIAE models, i.e the effect of both the initial state PRS and final state HRS as well as the event requirement. It turned out that the effect of both the PRS and HRS is weak because of the small reaction system of e^-+p and e^-+D SIDIS. The event requirement of having one parton (quark, antiquark, or gluon) at least in each generated initial partonic state introduced in the PACIAE model plays a visible role. However the effect of the requirement of having at least one

Table 2: Discrepancies between the PYTHIA and PACIAE models

item	PYTHIA	PACIAE
Partonic initial state	not introduced	introduced
Initial state PRS	no	yes
Final state HRS	no	yes
Event requirement	no	yes

pion or kaon in each event generated by the PYTHIA model is relatively strong. The main reason, which causes a discrepancy between the default PACIAE and PYTHIA results, should be attributed to the initial partonic state, introduced in the PACIAE model but not in PYTHIA.

Acknowledgments

This work was supported by the National Natural Science Foundation of China under grant Nos.:11075217, 11105227, 11175070, 11477130 and by the 111 project of the foreign expert bureau of China. BHS would like to thank C. P. Yuan for HERAFitter, G. Schnell for HERMES data, and Y. Mao and S. Joosten for discussions. YLY acknowledges the financial support from SUT-NRU project under contract No. 17/2555.

1. Xiangdong Ji, Nucl. Phys. B **402**, 217 (1993).
2. R. Placakyte, arXiv:1111.5452 v4 [hep-ph].
3. Klaus Rith, arXiv:1402.5000v1.
4. E. Leader, A. V. Sidorov, and D. B. Stamenov, arXiv:1312.5200v1.
5. A. Airapetian, et al., HERMES Collaboration, Nucl. Phys. B **780**, 1 (2007).
6. A. Airapetian, et al., HERMES Collaboration, Phys. Rev. D **87**, 074029 (2013).
7. A. Hillenbrand, Ph.D. thesis: DESY-THESIS-2005-035,2005.
8. G. Ingelman, A. Edin, and J. Rathsman, Comput. Phys. Comm. **101**, 108 (1997).
9. T. Sjöstrand, Comput. Phys. Comm. **82**, 74 (1994).
10. R. Brun, R. Hagedorn, M. Hansroul, and J. C. Lassalle, GEANT: Simulation program for particle physics experiments. User guide and reference manual, (1978), CERN-DD-78-2 Rev.
11. T. Sjöstrand, S. Mrenna, and P. Skands, JHEP **05**, 026 (2006).

12. Dai-Mei Zhou, Yu-Liang Yan, Bao-Guo Dong, Xu Cai, and Ben-Hao Sa, PACIAE 2.2: An updated issue of parton and hadron cascade model PACIAE 2.1 by inclusion of the lepton-nuclear DIS, in preparation.
13. Ben-Hao Sa, Dai-Mei Zhou, Yu-Liang Yan, Bao-Guo Dong, and Xu Cai, *Comput. Phys. Commu.* **184**, 1476 (2013); Ben-Hao Sa, Dai-Mei Zhou, Yu-Liang Yan, Xiao-Mei Li, Sheng-Qin Feng, Bao-Guo Dong, and Xu Cai, *Comput. Phys. Commu.* **183**, 333 (2012).
14. B. L. Combridge, J. Kripfgang, and J. Ranft, *Phys. Lett. B* **70**, 234 (1977).
15. C. Adloff, et. al., Hi Collaboration, *Eur. Phys. J. C* **19**, 269 (2001).
16. Review of Particle Physics, *Phys. Rev. D* **86**, 1 (2012).
17. J. D. Bjorken and E. A. Paschos, *Phys. Rev.* **185**, 1975 (1969); R. P. Feynman, *Photon hadron interactions*, Benjamin, New York, 1972.
18. A. Gzhko, HERAFitter, *Nucl. Phys. B, Proceedings Supplements*, 2013, 245: 161-163 (<http://herafitter.org>).
19. H1 and ZEUS Collaborations, H1prelim-13-141 and ZEUS-prel-13-003.
20. Xing-Long Li, Yu-Liang Yan, Xiao-Mei Li, Dai-Mei Zhou, Xu Cai, and Ben-Hao Sa, Calculation of lepton-nucleon neutral and charged current deep inelastic scattering cross sections, in preparation.

Collective modes in weakly anisotropic QGP

M.E. Carrington¹, K. Deja², St. Mrówczyński^{2,3}

¹ *Brandon University, Brandon, Manitoba, Canada,*

² *National Centre for Nuclear Research, Warsaw, Poland,*

³ *Jan Kochanowski University, Kielce, Poland*

Abstract

We discuss gluon collective modes (plasmons) in a weakly anisotropic quark-gluon plasma. The momentum distribution of plasma constituents is obtained by squeezing or stretching an isotropic distribution in one direction. The dispersion equations are solved analytically and numerically. The number of solutions, which depends on the length and orientation of the wave vector, is found by means of a Nyquist analysis.

1. Introduction

The spectrum of collective excitations is a fundamental characteristic of any many-body system. It carries a great deal of information about the thermodynamic and transport properties of an equilibrium system, and also controls to a large extent the temporal evolution of a non-equilibrium one. In the quark-gluon plasma there are collective modes that correspond to plasma particles, that is, quarks and (transverse) gluons, and there are also collective excitations which are genuine many-body phenomena like longitudinal gluon modes (longitudinal plasmons) and phonons. We present here some results of our very detailed study [1] on longitudinal and transverse gluon collective modes - *plasmons*, which play a crucial role in the dynamics of quark-gluon plasma.

The quark-gluon plasma (QGP) occurs as a transient state in relativistic heavy-ion collisions, see *e.g.* [2]. The momenta of the partons

produced at the earliest stage of the collisions are mostly along the beam, which means that the characteristic longitudinal momentum is bigger than the transverse one. The momentum distribution is thus elongated along the beam - it is *prolate*. The distribution evolves - mostly due to the free streaming - and, as discussed in *e.g.* [3], it becomes squeezed along the beam or *oblate* with the characteristic transverse momentum bigger than typical longitudinal momenta. The system moves towards an isotropic local equilibrium state. The equilibration process is not fully understood but it is clear that the spectrum of collective excitations of preequilibrium quark-gluon plasma is a key ingredient of any thermalization scenario.

Plasmons in anisotropic quark-gluon plasma have been studied repeatedly, see the review [4] and the papers [5–7] but the existing analyses are not complete. We discuss here gluon collective modes in weakly anisotropic quark-gluon plasma. Following Romatschke and Strickland [5, 6] the momentum distribution of plasma constituents is obtained by squeezing or stretching an isotropic distribution in one direction. The dispersion equations are solved both analytically and numerically, and the number of solutions, which depends on the length and orientation of the wave vector, is found by means of a Nyquist analysis. The weakly anisotropic system is particularly interesting because it differs qualitatively from the isotropic one and its general features survive even in case of strong anisotropy. It is also important that the weakly anisotropic plasma can be treated analytically to a large extent.

Throughout the paper we use natural units where $\hbar = c = 1$. The indices $i, j, k = 1, 2, 3$ label the Cartesian spatial coordinates.

2. Formulation of the problem

Dispersion equation for plasma collective excitations can be obtained using either the field theory methods or kinetic theory. The equation, which is the condition for existence of solutions of the homogeneous equation of motion, reads

$$\det[\Sigma(\omega, \mathbf{k})] = 0, \tag{1}$$

where ω is the frequency, \mathbf{k} denotes the wave vector and the matrix Σ is defined as

$$\Sigma^{ij}(\omega, \mathbf{k}) \equiv -\mathbf{k}^2 \delta^{ij} + k^i k^j + \omega^2 \varepsilon^{ij}(\omega, \mathbf{k}) \quad (2)$$

with $\varepsilon^{ij}(\omega, \mathbf{k})$ being the chromodielectric tensor. For a locally colorless anisotropic plasma in the collisionless limit or equivalently at the one-loop level, the dielectric tensor equals

$$\begin{aligned} \varepsilon^{ij}(\omega, \mathbf{k}) = \delta^{ij} &+ \frac{g^2}{2\omega} \int \frac{d^3p}{(2\pi)^3} \frac{v^i}{\omega - \mathbf{v} \cdot \mathbf{k} + i0^+} \\ &\times \left(\left(1 - \frac{\mathbf{k} \cdot \mathbf{v}}{\omega} \right) \delta^{jk} + \frac{v^j k^k}{\omega} \right) \nabla_p^k f(\mathbf{p}), \end{aligned} \quad (3)$$

where \mathbf{p} and $\mathbf{v} \equiv \mathbf{p}/|\mathbf{p}|$ are the momentum and velocity of a *massless* parton, and $f(\mathbf{p})$ is the effective parton distribution function. For the $SU(N_c)$ gauge group $f(\mathbf{p}) = n(\mathbf{p}) + \bar{n}(\mathbf{p}) + 2N_c n_g(\mathbf{p})$, where $n(\mathbf{p})$, $\bar{n}(\mathbf{p})$, $n_g(\mathbf{p})$ are the distribution functions of quarks, antiquarks and gluons of a single color component. We note that the chromodielectric tensor does not carry any color indices, as the state corresponding to the momentum distribution $f(\mathbf{p})$ is assumed to be colorless.

The dielectric tensor is fully determined by the momentum distribution of plasma constituents which, following Romatschke and Strickland [5], we choose in the form

$$f_\xi(\mathbf{p}) = C_\xi f_{\text{iso}}(\sqrt{\mathbf{p}^2 + \xi(\mathbf{p} \cdot \mathbf{n})^2}), \quad (4)$$

where $f_{\text{iso}}(|\mathbf{p}|)$ is an isotropic distribution, C_ξ is a normalization constant, \mathbf{n} is a unit vector, usually chosen along the beam direction, and the parameter $\xi \in (-1, \infty)$ controls the shape of the distribution. When $\xi = 0$ the distribution is isotropic. For $-1 < \xi < 0$ the distribution is elongated in the direction of \mathbf{n} - it is *prolate*. For $\xi > 0$ the distribution is squeezed in the direction of the vector \mathbf{n} - it is *oblate* - becoming more and more oblate as the parameter ξ increases.

There is some freedom in choosing the normalization constant C_ξ of the distribution (4). As the whole spectrum of collective excitations depends in case of massless partons on a single mass parameter, we

require the momentum distribution (4) to be normalized so that

$$m^2 \equiv \int \frac{d^3p}{(2\pi)^3} \frac{f_\xi(\mathbf{p})}{|\mathbf{p}|} = \int \frac{d^3p}{(2\pi)^3} \frac{f_{\text{iso}}(|\mathbf{p}|)}{|\mathbf{p}|}, \quad (5)$$

where the parameter m is the usual Debye mass. The normalization constant then equals

$$C_\xi = \begin{cases} \frac{\sqrt{|\xi|}}{\text{Arctanh}\sqrt{|\xi|}} & \text{for } -1 \leq \xi < 0, \\ \frac{\sqrt{\xi}}{\text{Arctan}\sqrt{\xi}} & \text{for } 0 \leq \xi. \end{cases} \quad (6)$$

To solve the general dispersion equation (1), one must either find the zeros of the determinant of the matrix Σ (2), or invert Σ and find the poles of the inverted matrix. We follow the second strategy.

The first step is to decompose the matrix Σ using a complete set of projection operators. Since the momentum distribution is deformed in only one direction given by the vector \mathbf{n} , an arbitrary symmetric tensor which depends on two vectors can be decomposed in terms of four projection operators. As in Ref. [5], we introduce the vector \mathbf{n}_T transverse to \mathbf{k} , which equals

$$n_T^i = \left(\delta^{ij} - \frac{k^i k^j}{\mathbf{k}^2} \right) n^j, \quad (7)$$

and define four projectors

$$\begin{aligned} A^{ij}(\mathbf{k}) &= \delta^{ij} - \frac{k^i k^j}{\mathbf{k}^2}, & B^{ij}(\mathbf{k}) &= \frac{k^i k^j}{\mathbf{k}^2}, \\ C^{ij}(\mathbf{k}, \mathbf{n}) &= \frac{n_T^i n_T^j}{\mathbf{n}_T^2}, & D^{ij}(\mathbf{k}, \mathbf{n}) &= k^i n_T^j + k^j n_T^i. \end{aligned} \quad (8)$$

Using this projector basis, the matrix Σ can be decomposed as

$$\Sigma^{ij} = a A^{ij} + b B^{ij} + c C^{ij} + d D^{ij}, \quad (9)$$

where the coefficients a, b, c, d depend on ω and \mathbf{k} . Decomposing the inverse matrix in the same way, one finds

$$(\Sigma^{-1})^{ij} = \frac{1}{a} A^{ij} + \frac{-a(a+c) B^{ij} + (-d^2 \mathbf{k}^2 \mathbf{n}_T^2 + bc) C^{ij} + ad D^{ij}}{a(d^2 \mathbf{k}^2 \mathbf{n}_T^2 - b(a+c))}. \quad (10)$$

As seen, the dispersion equations are

$$a(\omega, \mathbf{k}) = 0, \quad (11)$$

$$\frac{b(\omega, \mathbf{k})(a(\omega, \mathbf{k}) + c(\omega, \mathbf{k})) - \mathbf{k}^2 \mathbf{n}_T^2 d^2(\omega, \mathbf{k})}{\omega^2} = 0. \quad (12)$$

The factor $1/\omega^2$ is introduced in the second equation to remove two trivial zero solutions that are of no physical interest.

When the anisotropy is weak, the coefficient $d(\omega, \mathbf{k})$, as explained in Sec. 3, can be neglected and the second dispersion equation (12) factors into two simpler equations

$$\frac{b(\omega, \mathbf{k})}{\omega^2} = 0, \quad (13)$$

$$a(\omega, \mathbf{k}) + c(\omega, \mathbf{k}) = 0. \quad (14)$$

We refer to solutions of the dispersion equation (11) as A -modes, and to the solutions of the equations (13, 14) as B -modes and C -modes, respectively. In the B -mode equation we have again removed two zero solutions.

Solutions $\omega(\mathbf{k})$ of the dispersion equations represent plasmons or gluon collective modes. There are *transverse* plasmons, for which the chromoelectric field is transverse to the wave vector \mathbf{k} , and *longitudinal* plasmons with chromoelectric field parallel to \mathbf{k} . The transverse modes correspond to oscillations of current, and the longitudinal ones to oscillations of charge density.

A mode is called *unstable* if $\Im\omega(\mathbf{k}) > 0$, because the amplitude $\sim e^{\Im\omega(\mathbf{k})t}$ grows exponentially in time. When $\Im\omega(\mathbf{k}) \leq 0$, the mode is *stable*. The mode is *damped* whenever $\Im\omega(\mathbf{k}) < 0$ and it is *over-damped* when additionally $\Re\omega(\mathbf{k}) = 0$. We have shown that there are no complex solutions of the dispersion equations (11, 12), only pure real and pure imaginary ones. The real solutions correspond to undamped propagating modes, and the imaginary ones to unstable or over-damped modes (depending on the sign of the solution). Every solution has a partner with opposite sign. In the case of imaginary solutions, every unstable mode has a partner over-damped mode.

3. Collective modes

The coefficients a, b, c, d can be computed analytically for $|\xi| \ll 1$. For a and b there are contributions of order ξ^0 which are just the results for the isotropic plasma. All four functions a, b, c, d have contributions of order ξ . Since the coefficient d enters the dispersion equation (12) quadratically, it does not contribute to linear order in ξ and the dispersion equation factorizes into two pieces, so that we have the three dispersion equations of A -modes (11), B -modes (13) and C -modes (14).

In the following three subsections we discuss solutions of the dispersion equations (11, 13, 14).

3.1. A -modes

The Nyquist analysis, which is performed in [1], shows that the dispersion equation (11) has four solutions when

$$k^2 - \xi \frac{m^2}{3} \cos^2 \theta < 0 \quad (15)$$

(θ is the angle between \mathbf{k} and \mathbf{n}) and two solutions otherwise. The condition (15) is never fulfilled for the prolate plasma ($\xi < 0$) and it is fulfilled for any oblate momentum distribution ($\xi > 0$) when

$$k < k_A \equiv \Re \sqrt{\frac{\xi}{3}} m |\cos \theta|. \quad (16)$$

Because of the real value in the definition of k_A , it vanishes for $\xi < 0$.

When $\omega^2 \gg k^2$, Eq. (11) is solved by

$$\omega^2(\mathbf{k}) \approx \frac{m^2}{3} \left(1 - \frac{\xi}{15}\right) + \frac{6}{5} \left[1 + \frac{\xi}{14} \left(\frac{4}{15} + \cos^2 \theta\right)\right] k^2, \quad (17)$$

which reduces to the well-known transverse plasmon for $\xi = 0$. The plasmon mass, which is given by the first term on the right side of Eq. (17), depends on the anisotropy parameter ξ but is independent of the orientation of the wave vector \mathbf{k} . When compared to isotropic plasma, the plasmon mass is smaller for oblate momentum distributions ($\xi > 0$) and bigger for prolate ones ($\xi < 0$).

When the condition (16) is satisfied, which occurs only for the oblate system ($\xi > 0$), one also finds pure imaginary solutions by substituting $\omega = i\gamma$ with $\gamma \in \mathbb{R}$ and assuming that $\gamma^2 \gg k^2$. There are two solutions

$$\gamma(\mathbf{k}) \approx \pm \frac{1}{2} \left(\sqrt{\frac{\lambda^2}{k^2} + 4(k_A^2 - k^2)} - \frac{\lambda}{k} \right). \quad (18)$$

where k_A is given by Eq. (16) and

$$\lambda \equiv \frac{\pi}{4} \left[1 - \frac{\xi}{2} \left(\frac{1}{3} - 3 \cos^2 \theta \right) \right] m^2. \quad (19)$$

The solutions (18) represent the unstable and overdamped transverse modes.

3.2. *B*-modes

According to the Nyquist analysis [1], there are always two solutions of the dispersion equation (13) which describes longitudinal modes. In the limit $\omega^2 \gg k^2$, one finds these solutions analytically as

$$\omega^2(\mathbf{k}) \approx \frac{m^2}{3} \left[1 + \frac{\xi}{5} \left(-\frac{1}{3} + \cos^2 \theta \right) \right] + \frac{3}{5} \left[1 + \frac{4\xi}{35} (1 - 3 \cos^2 \theta) \right] k^2, \quad (20)$$

which reduce to the well-known longitudinal plasmon when $\xi = 0$. The first term on the right side gives the plasmon mass which depends on the anisotropy parameter ξ and the orientation of wave vector \mathbf{k} . One shows that the longitudinal mode approaches the light cone as $k \rightarrow \infty$.

3.3. *C*-modes

The dispersion equation (14) has the richest structure. It has four solutions when

$$k^2 + \xi \frac{m^2}{3} (1 - 2 \cos^2 \theta) < 0 \quad (21)$$

and two solutions otherwise. The condition (21) can be fulfilled for oblate plasma ($\xi > 0$) when $1/2 < \cos^2 \theta$ and for prolate plasma ($\xi < 0$) when $1/2 > \cos^2 \theta$. In both cases the wave vector must satisfy

$$k < k_C \equiv m \Re \sqrt{\frac{\xi}{3} (2 \cos^2 \theta - 1)}. \quad (22)$$

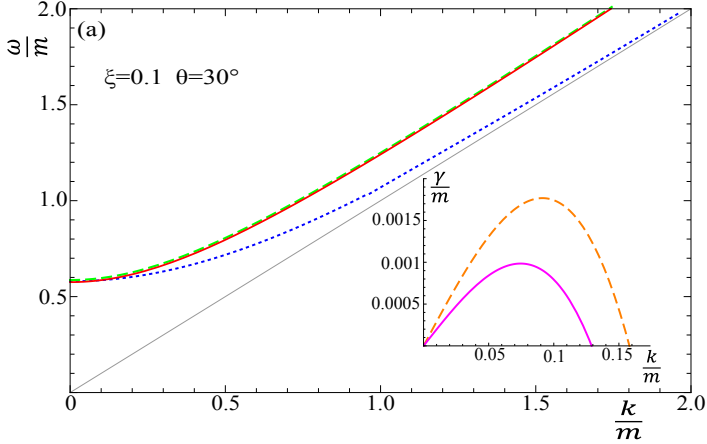


Fig. 1: Dispersion curves of plasmons in weakly oblate plasma with $\xi = 0.1$ for $\theta = 30^\circ$. The red (solid), blue (dotted) and green (dashed) lines represent the real $A-$, $B-$ and $C-$ modes, respectively. The orange (dashed) and pink (solid) lines are for the imaginary $A-$ and $C-$ modes. We show only the partners of positive ω or γ .

When the argument of the square root is negative, the real part of the root is zero and the critical wave vector k_C vanishes.

The real solutions in the long wavelength limit ($\omega^2 \gg k^2$) are

$$\omega^2(\mathbf{k}) \approx \frac{m^2}{3} \left[1 + \frac{\xi}{5} \left(\frac{2}{3} - \cos^2 \theta \right) \right] + \frac{6}{5} \left[1 - \frac{\xi}{5} \left(\frac{23}{42} - \cos^2 \theta \right) \right] k^2, \quad (23)$$

which reduce to the well-known transverse plasmon when $\xi = 0$. The plasmon mass, which is given by the first term on the right side, depends on the anisotropy parameter ξ and on the orientation of \mathbf{k} .

One also finds pure imaginary solutions by substituting $\omega = i\gamma$ with $\gamma \in \mathbb{R}$ and assuming $\gamma^2 \ll k^2$. The dispersion equation and its solutions have the same form as those given by Eq. (18), but the coefficient λ is now defined as

$$\lambda \equiv \frac{\pi}{4} \left[1 - \frac{\xi}{2} \left(\frac{7}{3} - 5 \cos^2 \theta \right) \right] m^2, \quad (24)$$

and k_A is replaced by k_C given in Eq. (22).

4. Discussion and final remarks

We have found a complete spectrum of plasmons in weakly anisotropic QGP solving numerically the dispersion equations (11, 13, 14). The numerical solutions agree very well with the approximated analytical ones (17, 18, 20, 23) in the domains of their applicability. Fig. 1 shows the spectrum for weakly oblate plasma ($\xi = 0.1$) at $\theta = 30^\circ$. In the main part of the figure there are the dispersion curves of the positive real modes and the insert presents the positive imaginary solutions.

The real $A-$, $B-$ and $C-$ modes exist for all wave vectors and depend only weakly on the angle θ between \mathbf{k} and \mathbf{n} . The real $A-$ and $C-$ modes look very much like the real isotropic transverse mode. In addition to the real modes, for weakly prolate plasma there is an imaginary $C-$ mode which exists for $k < k_C$. The critical wave vector k_C is maximal for $\theta = 90^\circ$. When θ decreases, k_C also decreases until it reaches zero at $\theta = 45^\circ$ and the imaginary $C-$ mode disappears. In a weakly oblate system there are two imaginary modes seen in Fig. 1 when $k < k_C < k_A$. Both k_A and k_C are maximal when $\theta = 0^\circ$. As θ increases from 0° , k_A and k_C decrease. At $\theta = 45^\circ$, k_C goes to zero and the imaginary $C-$ mode disappears. The regime of the imaginary $A-$ mode shrinks to zero at $\theta = 90^\circ$. There is a maximum of 8 modes for the prolate plasma and 10 for the oblate plasma.

In comparison with the spectra of an isotropic system, the weakly anisotropic plasma exhibits the following important differences.

- The transverse real mode, which is doubled in the isotropic case, is now split into two slightly different $A-$ and $C-$ mode, which are given by Eqs. (17, 23).
- In isotropic plasma, longitudinal and transverse plasmons have the same plasma frequency $\omega_p \equiv \omega(\mathbf{k} = 0) = m/\sqrt{3}$, but in anisotropic plasma there are three different plasma frequencies for the three real modes.
- In isotropic plasma there are no imaginary solutions. In anisotropic plasma the number of imaginary solutions depends on the magnitude and orientation of the wave vector \mathbf{k} . In prolate plasma the

number of imaginary solutions is zero or two (one pair) and in oblate plasma there are zero, two (one pair) or four (two pairs) imaginary modes.

There is no anisotropy threshold for the existence of unstable modes, and even an infinitesimal anisotropy produces an instability. However, when $\xi \rightarrow 0$ the growth rate of instability (γ) decreases and the domain of unstable modes shrinks. In this sense, the system becomes less and less unstable as it tends to isotropy. When the effect of inter-parton collisions is taken into account [11], the growth rates of unstable modes are reduced and systems of small anisotropy are effectively stabilized.

A very detailed analysis of plasmons in the quark-gluon plasma is given in our recent publication [1]. The momentum distribution of plasma constituents varies from the extremely prolate through isotropic to the extremely oblate.

Acknowledgments

This work was partially supported by the Polish National Science Centre under grant 2011/03/B/ST2/00110 and the Natural Sciences and Engineering Research Council of Canada.

1. M. E. Carrington, K. Deja and St. Mrówczyński, *Phys. Rev. C* **90**, 034913 (2014).
2. W. Florkowski, *Phenomenology of Ultra-Relativistic Heavy-Ion Collisions* (World Scientific, Singapore, 2010).
3. W. Jas and St. Mrówczyński, *Phys. Rev. C* **76**, 044905 (2007).
4. St. Mrówczyński, *Acta Phys. Polon. B* **37**, 427 (2006).
5. P. Romatschke and M. Strickland, *Phys. Rev. D* **68**, 036004 (2003).
6. P. Romatschke and M. Strickland, *Phys. Rev. D* **70**, 116006 (2004).
7. P. B. Arnold, J. Lenaghan and G. D. Moore, *JHEP* **0308**, 002 (2003).
8. St. Mrówczyński and M. H. Thoma, *Ann. Rev. Nucl. Part. Sci.* **57**, 61 (2007).
9. E. M. Lifshitz and L. P. Pitaevskii, *Physical Kinetics* (Pergamon, Oxford, 1981).
10. M. Le Bellac, *Thermal Field Theory* (Cambridge University Press, Cambridge, 2000).
11. B. Schenke, M. Strickland, C. Greiner and M. H. Thoma, *Phys. Rev. D* **73**, 125004 (2006).



Universal Character of the Hard-Loop Action

Alina Czajka¹, Stanisław Mrówczyński^{1,2}

¹ *Institute of Physics, Jan Kochanowski University, Kielce, Poland,*
² *National Centre for Nuclear Research, Warsaw, Poland*

Abstract

The effective actions of gauge bosons, fermions, and scalars, which are obtained within the hard-loop approximation, are shown to have unique forms for a whole class of gauge theories including QED, scalar QED, super QED, pure Yang-Mills, QCD, super Yang-Mills. The universality occurs irrespective of a field content of each theory and of an variety of specific interactions. Consequently, the long-wavelength or semi-classical features of plasma systems governed by these theories, such as collective excitations, are almost identical. An origin of the universality is discussed.

1. Introduction

The hard-loop approach is a practical tool to describe plasma systems governed by QED or QCD in a gauge invariant way which is free of infrared divergences, see the reviews [1–4]. Initially, the approach was developed within the thermal field theory [5, 6] but it was soon realized that it can be formulated in terms of quasiclassical kinetic theory [7, 8]. The plasma systems under consideration were assumed to be in thermodynamical equilibrium but the methods can be naturally generalized to plasmas out of equilibrium [9, 10].

An elegant and concise formulation of the hard-loop approach is achieved by introducing an effective action derived for equilibrium and non-equilibrium systems in [11–13] and [9, 14], respectively. The action is a key quantity that encodes an infinite set of hard-loop n -point functions. A whole gamut of long-wavelength characteristics of a plasma

system is carried by the functions. In particular, the two-point functions or self-energies provide response functions like permeabilities or susceptibilities which control various screening lengths. The self-energies also determine a spectrum of collective excitations (quasiparticles) that is a fundamental characteristic of any many-body system.

One wonders how much a given plasma characteristic is different for different plasma systems. It has been known for a long time that the self-energies of gauge bosons in the long-wavelength limit are of the same structure for QED and QCD plasmas [15]. Consequently, the collective excitations and many other characteristics are the same, or almost the same, in the two plasma systems [16].

Comparing systematically supersymmetric plasmas to their usual counterparts, we have considered [17–19] a whole class of gauge theories including Abelian cases: QED, scalar QED, and $\mathcal{N} = 1$ super QED and nonAbelian ones: pure Yang-Mills, QCD, and $\mathcal{N} = 4$ super Yang-Mills. We have observed that the self-energies of gauge bosons, fermions, and scalars, which are computed in the hard-loop approximation, have unique structures for all considered theories irrespective of a field content and of an variety of specific interactions. Consequently, the hard-loop effective actions are essentially the same and so are long-wavelength characteristics of plasma systems governed by the gauge theories of interest. Although our findings are partially presented in [17–19], we have decided to systematically elaborate on the problem. We explain an origin of the universality and discuss its physical consequences and limitations. All our results are collected in [20] and here we summarize the whole analysis.

Throughout the paper we use the natural system of units with $c = \hbar = k_B = 1$; our choice of the signature of the metric tensor is $(+ - - -)$.

2. Self-energies

Our objective is to derive the effective action of all considered theories in the hard-loop approximation. The action S can be found *via* the respective self-energies which are the second functional derivatives of S with respect to the given fields. Thus, the self-energies of gauge boson,

fermion, and scalar fields equal

$$\Pi^{\mu\nu}(x, y) = \frac{\delta^2 S}{\delta A_\mu(x) \delta A_\nu(y)}, \quad (1)$$

$$\Sigma(x, y) = \frac{\delta^2 S}{\delta \bar{\Psi}(x) \delta \Psi(y)}, \quad (2)$$

$$P(x, y) = \frac{\delta^2 S}{\delta \Phi^*(x) \delta \Phi(y)}, \quad (3)$$

where the field indices, which are different for different theories under consideration, are suppressed. The action will be obtained in the subsequent section by integrating the formulas (1)-(3) over the respective fields.

We compute the self-energies, which enter Eqs. (1)-(3), diagrammatically. The plasma systems under study are assumed to be homogeneous in coordinate space (translationally invariant), locally colorless and unpolarized, but the momentum distribution may be arbitrary. Therefore, we use the Keldysh-Schwinger or real-time formalism, explained in *e.g.* [21], which allows one to describe many-body systems both in and out of equilibrium.

The comprehensive discussion of the polarization tensors of different theories is presented in [20]. The differences between polarization tensors lie both in the number of diagrams contributing to them and also in their forms. We have the fermion, scalar, and gluon loops and the scalar and gluon tadpoles which differently depend on the external momentum. Accordingly, there is no surprise that the polarization tensors $\Pi^{\mu\nu}(k)$ are quite different for each theory. However, when the external momentum k is much smaller than the internal momentum p , which flows along the loop and is carried by a plasma constituent, that is when the hard-loop approximation ($k \ll p$) is applied, we get a very striking result: the (retarded) polarization tensors of all theories are of the same form

$$\Pi^{\mu\nu}(k) = C_\Pi \int \frac{d^3 p}{(2\pi)^3} \frac{f_\Pi(\mathbf{p})}{E_p} \frac{k^2 p^\mu p^\nu - (k^\mu p^\nu + p^\mu k^\nu - g^{\mu\nu}(k \cdot p))(k \cdot p)}{(k \cdot p + i0^+)^2}, \quad (4)$$

where C_Π is some factor and $f_\Pi(\mathbf{p})$ an effective distribution function of plasma constituents. In case of non-supersymmetric plasmas, there

is subtracted from the formula (4) the (infinite) vacuum contribution which otherwise survives when $f_{\Pi}(\mathbf{p})$ is sent to zero. The subtraction is not needed for the supersymmetric theories where the vacuum effect cancels out. The polarization tensor (4), which is chosen to obey the retarded initial condition, is symmetric in Lorentz indices, $\Pi^{\mu\nu}(k) = \Pi^{\nu\mu}(k)$, and transverse, $k_{\mu}\Pi^{\mu\nu}(k) = 0$, and thus it is gauge independent. We note that the transversality of $\Pi^{\mu\nu}(k)$ is *not* an assumption but it automatically results from the calculations, the details of which are given in [17,19,22]. In case of nonAbelian theories, the transversality of $\Pi^{\mu\nu}(k)$ requires us to include the Faddeev-Popov ghosts when the calculations are performed in a covariant gauge. The problem of how to include the ghosts in the Keldysh-Schwinger formalism is discussed in [22].

One wonders how the universality of the polarization tensor emerges. This is not the case that every one-loop contribution behaves in the same way in the long-wavelength limit. Just the opposite, the fermion loops contribute differently than boson ones, and the tadpoles are different than the loops. However, every subset of diagrams which is, as a sum of the diagrams, gauge independent, has the same long-wavelength limit. We also note that the universality holds within the domain of validity of the hard-loop approximation which is explained at the end of this section. A physical origin of the universality is discussed in Sec. 4.

Microscopically, there are also significant differences between fermion self-energies of different gauge theories, see [20]. However, when the hard-loop approximation is applied, the (retarded) self-energies of all theories are of the same form

$$\Sigma(k) = C_{\Sigma} \int \frac{d^3p}{(2\pi)^3} \frac{f_{\Sigma}(\mathbf{p})}{E_p} \frac{\not{p}}{k \cdot p + i0^+}. \quad (5)$$

As in case of the polarization tensors and fermion self-energies, the self-energy of scalars $P(k)$ are quite different for each theory, see [20]. However, within the hard-loop approximation we obtain the amazingly repetitive result - the scalar self-energies of all theories have the same form

$$P(k) = -C_P \int \frac{d^3p}{(2\pi)^3} \frac{f_P(\mathbf{p})}{E_p}, \quad (6)$$

which is real, negative and independent of the wave vector k .

The universal expressions of the self-energies (4), (5), and (6) have been obtained in the hard-loop approximation that is when $k \ll p$. However, it appears that the self-energies (4), (5), and (6) are valid when the external momentum k is not too small. It is most easily seen in case of the fermion self-energy (5) which diverges as $k \rightarrow 0$. When we deal with an equilibrium (isotropic) plasma of temperature T , the characteristic momentum of (massless) plasma constituents is of the order T . One observes that if the external momentum k is of the order $g^2 T$, which is the so-called *magnetic* or *ultrasoft* scale, the self-energy (5) is not perturbatively small, as it is of the order $\mathcal{O}(g^0)$. Therefore, the expression (5) is meaningless for $k \leq g^2 T$. Since k must be much smaller than $p \sim T$, one arrives to the well-known conclusion that the self-energy (5) is valid at the *soft* scale that is when k is of the order gT . Analyzing higher order corrections to the self-energies (4), (5), and (6), one shows that they are indeed valid for $k \sim gT$ and they break down at the magnetic scale because of the infrared problem of gauge theories, see *e.g.* the review [4]. When the momentum distribution of plasma particles is anisotropic, instead of the temperature T , we have a characteristic four-momentum \mathcal{P}^μ of plasma constituents and the hard-loop approximation requires that $\mathcal{P}^\mu \gg k^\mu$. Validity of the self energies (4), (5), and (6) is then limited to $k^\mu \sim g\mathcal{P}^\mu$.

3. Effective action

Having the self-energies $\Pi^{\mu\nu}(k)$, $\Sigma(k)$, and $P(k)$ given by Eqs. (4), (5), and (6), respectively, we can reconstruct the effective action. Integrating the formulas (1)-(3) over the respective fields and using the explicit expressions of the self-energies (4), (5), and (6), we obtain the Lagrangian densities

$$\mathcal{L}_2^A(x) = C_\Pi \int \frac{d^3 p}{(2\pi)^3} \frac{f_\Pi(\mathbf{p})}{E_p} F_{\mu\nu}(x) \frac{p^\nu p^\rho}{(p \cdot \partial)^2} F_\rho^\mu(x), \quad (7)$$

$$\mathcal{L}_2^\Psi(x) = C_\Sigma \int \frac{d^3 p}{(2\pi)^3} \frac{f_\Sigma(\mathbf{p})}{E_p} \bar{\Psi}(x) \frac{p \cdot \gamma}{p \cdot \partial} \Psi(x), \quad (8)$$

$$\mathcal{L}_2^\Phi(x) = -C_P \int \frac{d^3 p}{(2\pi)^3} \frac{f_P(\mathbf{p})}{E_p} \Phi^*(x) \Phi(x). \quad (9)$$

In case of $\mathcal{N} = 4$ super Yang-Mills, where the scalar fields are real, there is an extra factor $1/2$ in the r.h.s of Eq. (9). The subscript ‘2’ indicates that the above effective actions generate only two-point functions. We omit the field indices in Eqs. (7)-(9) to keep the expressions applicable to all considered theories. The action is obviously expressed as $S = \int d^4x \mathcal{L}$.

The n -point functions with $n > 2$, which are generated by the actions (7)-(9), identically vanish, as the actions are quadratic in fields. We also observe that the action of scalars (9) is gauge invariant for every theory which includes the scalar field. Moreover, the gauge boson action (7) is invariant as well but only in the Abelian theories. The fermion action is gauge dependent in all theories under consideration. Therefore, the fermion action and, in general, the gauge boson action need to be modified to comply with the principle of gauge invariance. This is achieved by simply replacing the usual derivative ∂^μ by the covariant derivative D^μ in Eqs. (7) and (8). Thus, we obtain

$$\mathcal{L}_{\text{HL}}^A(x) = C_{\text{II}} \int \frac{d^3p}{(2\pi)^3} \frac{f_{\text{II}}(\mathbf{p})}{E_p} F_{\mu\nu}(x) \frac{p^\nu p^\rho}{(p \cdot D)^2} F_\rho^\mu(x), \quad (10)$$

$$\mathcal{L}_{\text{HL}}^\Psi(x) = C_\Sigma \int \frac{d^3p}{(2\pi)^3} \frac{f_\Sigma(\mathbf{p})}{E_p} \bar{\Psi}(x) \frac{p \cdot \gamma}{p \cdot D} \Psi(x), \quad (11)$$

$$\mathcal{L}_{\text{HL}}^\Phi(x) = -C_P \int \frac{d^3p}{(2\pi)^3} \frac{f_P(\mathbf{p})}{E_p} \Phi^*(x) \Phi(x). \quad (12)$$

The hard-loop actions (10), (11), and (12) are all of the universal form for a whole class of gauge theories. However, the case of Abelian fields differs from that of nonAbelian ones. In the electromagnetic theories the gauge boson and scalar actions are quadratic in fields. Therefore, the n -point functions generated by these actions vanish for $n > 2$. Only the fermion action generates the non-trivial three-point and higher functions. The action (11) is, in particular, responsible for a modification of the electromagnetic vertex. In the nonAbelian theories, both the gauge boson and fermion actions generate the non-trivial three-point and higher functions. Therefore, the gluon-fermion, three-gluon, and four-gluon couplings are all modified.

4. Discussion

We have shown that the hard-loop self-energies of gauge, fermion, and scalar fields are of the universal structures and so are the effective actions of QED, scalar QED, $\mathcal{N} = 1$ super QED, Yang-Mills, QCD, and $\mathcal{N} = 4$ super Yang-Mills. One asks why the universality occurs physically. Taking into account a diversity of the theories - various field content and microscopic interactions - the uniqueness of the hard-loop effective action is rather surprising.

To better understand the problem in physical terms, let us consider the QED plasma of spin $1/2$ electrons and positrons and the scalar QED plasma of spin 0 particles and antiparticles. The universality of hard-loop action means that neither effects of quantum statistics of plasma constituents are observable nor the differences in elementary interactions which govern the dynamics of the two systems. Both facts can be understood as follows. The hard-loop approximation requires that the momentum at which a plasma is probed, that is the wavevector k , is much smaller than the typical momentum of a plasma constituent p . Therefore, the length scale, at which the plasma is probed, $1/k$, is much greater than the characteristic de Broglie wavelength of plasma particle, $1/p$. The hard-loop approximation thus corresponds to the classical limit where fermions and bosons of the same masses and charges are not distinguishable. The fact that the differences in elementary interactions are not seen results from the very nature of gauge theories - the gauge symmetry fully controls the interaction. And the hard-loop effective actions obey the gauge symmetry.

The universality of hard-loop actions has far-reaching physical consequences: the characteristics of all plasma systems under consideration, which occur at the soft scale, are qualitatively the same. In particular, spectra of collective excitations of gauge, fermion, and scalar fields are the same. Therefore, if the electromagnetic plasma with a given momentum distribution is, say, unstable, the quark-gluon plasma with this momentum distribution is unstable as well. We conclude that in spite of all differences, the plasma systems under consideration are very similar to each other at the soft scale. However, the hard-loop approach breaks

down for the momenta at and below the magnetic scale. Then, systems governed by different theories can behave very differently. In particular, the QED plasma is very different from the QCD one, as in the latter case effects of confinement apparently appear at the magnetic scale.

Acknowledgments

This work was partially supported by the Polish National Science Centre under Grant No. 2011/03/B/ST2/00110.

1. M. H. Thoma, in *Quark-Gluon Plasma 2*, edited by R.C. Hwa (World Scientific, Singapore, 1995).
2. J. P. Blaizot and E. Iancu, Phys. Rept. **359**, 355 (2002).
3. D. F. Litim and C. Manuel, Phys. Rept. **364**, 451 (2002).
4. U. Kraemmer and A. Rebhan, Rept. Prog. Phys. **67**, 351 (2004).
5. E. Braaten and R. D. Pisarski, Nucl. Phys. B **337**, 569 (1990).
6. E. Braaten and R. D. Pisarski, Nucl. Phys. B **339**, 310 (1990).
7. J. P. Blaizot and E. Iancu, Nucl. Phys. B **417**, 608 (1994).
8. P. F. Kelly, Q. Liu, C. Lucchesi and C. Manuel, Phys. Rev. D **50**, 4209 (1994).
9. R. D. Pisarski, arXiv:hep-ph/9710370.
10. St. Mrówczyński and M. H. Thoma, Phys. Rev. D **62**, 036011 (2000).
11. J. C. Taylor and S. M. H. Wong, Nucl. Phys. B **346**, 115 (1990).
12. J. Frenkel and J. C. Taylor, Nucl. Phys. B **374**, 156 (1992).
13. E. Braaten and R. D. Pisarski, Phys. Rev. D **45**, 1827 (1992).
14. St. Mrówczyński, A. Rebhan and M. Strickland, Phys. Rev. D **70**, 025004 (2004).
15. H. A. Weldon, Phys. Rev. D **26**, 1394 (1982).
16. St. Mrówczyński and M. H. Thoma, Ann. Rev. Nucl. Part. Sci. **57**, 61 (2007).
17. A. Czajka and St. Mrówczyński, Phys. Rev. D **83**, 045001 (2011).
18. A. Czajka and St. Mrówczyński, Phys. Rev. D **84**, 105020 (2011).
19. A. Czajka and St. Mrówczyński, Phys. Rev. D **86**, 025017 (2012).
20. A. Czajka and S. Mrówczyński, arXiv:1410.5117 [hep-ph], Phys. Rev. D in print.
21. St. Mrówczyński and U. W. Heinz, Annals Phys. **229**, 1 (1994).
22. A. Czajka and St. Mrówczyński, Phys. Rev. D **89**, 085035 (2014).

Newest Developments in Cluster Radioactivity

D. N. Poenaru and R. A. Gherghescu

*Horia Hulubei National Institute for Physics and Nuclear Engineering
(IFIN-HH), Bucharest-Magurele, Romania
e-mail: poenaru@nipne.ro*

Abstract

All measured half-lives on ^{14}C , ^{20}O , ^{23}F , $^{22,24-26}\text{Ne}$, $^{28,30}\text{Mg}$, and $^{32,34}\text{Si}$ radioactivities are in agreement with predicted values within our analytical superasymmetric fission (ASAF) model. The universal (UNIV) formula gives similar results. Competition of α decay is estimated using not only ASAF and UNIV, but also the semFIS (semi-empirical relationship based on fission theory) model. Spontaneous fission is the other competing decay mode in the region of superheavy nuclei. A dynamical theory using cranking inertia is a promising solution to calculate fission half-lives.

1. Introduction

The analytical superasymmetric fission (ASAF) model was successfully employed to make a systematic search and to predict, with other models, cluster radioactivity [1, 2]. The experiments confirmed the half-lives and the crucial importance of shell effects for parent nuclei with atomic numbers $Z = 87 - 96$ and established a rare phenomenon in a strong background of alpha particles.

Following our previous works [3, 4] we continue to study the competition of three decay modes of superheavy nuclei: α decay (αD), cluster radioactivity (CR) and spontaneous fission (SF). Previously we have shown [5] that calculated α decay half-lives are in agreement with experimental data within one order of magnitude, while the discrepancy

between theory and experiment can be as high as ten orders of magnitude for spontaneous fission [6–12].

In the above mentioned decay modes, from a parent nucleus AZ we obtain an emitted particle (or light fragment) ${}^{A_2}Z_2$ and a daughter (heavy fragment) ${}^{A_1}Z_1$. The studied decay modes are explained by quantum tunnelling (for the first time studied by George Gamow in 1928) of potential barrier. The decay constant

$$\lambda = \ln 2/T = \nu SP_s \quad (1)$$

is expressed as a product of three model dependent quantities ν , S and P_s , where ν is the frequency of assaults on the barrier per second, S is the preformation probability and P_s is the penetrability of the external barrier (separated fragments). In the above equation $T = T_\alpha$ or $T = T_c$ or $T = T_f$. Starting from eq. (1) we denote $P = SP_s = \exp(-K)$. The half-life expressed in seconds is calculated with a relationship

$$T = \frac{h \ln 2}{2} \frac{1}{E_v P} ; \quad K = \frac{2\sqrt{2m}}{\hbar} \int_{R_a}^{R_b} \{B(R)[E(R) - E(R_a)]\}^{1/2} dR \quad (2)$$

where h is the Planck constant, $E_v = h\nu/2$ is the zero-point vibration energy, K is the action integral, R_a and R_b are the turning points [$E(R_a) = E(R_b) = Q + E_v$], B is the nuclear inertia in units of nucleon mass m , and Q is the released energy expressed in MeV.

For T_α in α D and for T_c in CR we use our models ASAF (analytical superasymmetric fission) and UNIV (universal curve). For α D we also have semFIS (semiempirical model based on fission theory). We considered competition of SF by making calculations within the Werner-Wheeler approximation of inertia and the two center shell model to obtain the microscopical input for Strutinsky's shell and pairing corrections [5]. Werner-Wheeler approximation gives a too low value of the nuclear inertia; we checked few simple laws of variation of $B(R)$ in order to get agreement with experimental result for ${}^{284}\text{Cn}$. Recently we tried a better solution based on the microscopic cranking model [13] illustrated for ${}^{282}\text{Cn}$.

2. 75 years of Nuclear Fission

The induced Nuclear Fission was discovered by Otto Hahn and Fritz Strassmann in December 1938. It was explained by Lise Meitner and Otto Frisch on the basis of Liquid Drop Model. Since their papers were published in 1939 we may say that officially in 2014 we celebrate the 75th anniversary. The high impact on our society may be summarized by saying that *“the world will never be the same.”*

As mentioned above we used fission theory to predict CR and to study the competition of α decay. Consequently we have been lucky to attend the four Conferences (Physics and Chemistry of Fission, Gaussig near Dresden; Fifty Years Research in Nuclear Fission, West Berlin; 50 Years with Nuclear Fission, Gaithersburg, Maryland, USA; and 50th Anniversary of Nuclear Fission, Leningrad) celebrating 50 years of Nuclear Fission [14–18].

By the end of 2013 the 75 years of nuclear fission was honored in Germany [19] and USA [20]. The American Nuclear Society celebrated the 75th anniversary of the discovery of nuclear fission at its 2013 Winter Meeting in Washington, D.C. Also, we invite you to watch the short movie [21] produced by Los Alamos Nat. Lab., showing many photos with the “Gods of Nuclear Physics”.

In May 2014 we presented two invited talks (Fission approach to cluster radioactivity, and Spontaneous fission of superheavy nuclei) at the International Conference “75-years of Nuclear Fission: Present status and future perspectives” held at Bhabha Atomic Research Centre, Mumbai, India.

3. Cluster radioactivity and α decay of superheavy nuclei

Calculations of half-lives of superheavy nuclei (SH) [22] show an unexpected result [3]: for some of them cluster radioactivity (CR) [2, 23] dominates over alpha decay — the main decay mode of the majority of recently discovered SHs. We changed the concept of CR in order to allow emitted particles with $Z_e > 28$ from parents with $Z > 110$ and daughters around ^{208}Pb . From a typical example shown in Fig. 1 the trend of

increasing branching ratio $b_\alpha = T_\alpha/T_c$ for heavier nuclei may be clearly seen.

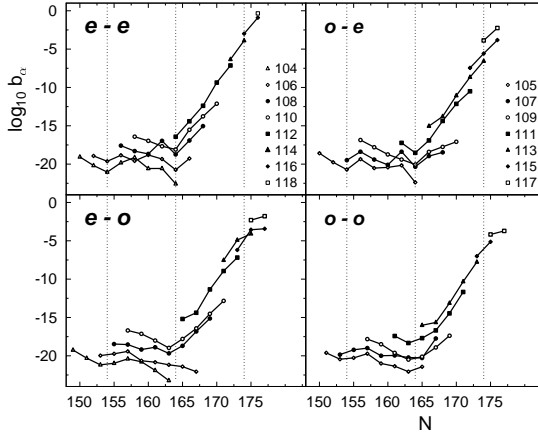


Fig. 1: The branching ratios with respect to alpha decay in the region of superheavy nuclei with $Z = 104 - 118$ in four groups of nuclides.

For αD we have a comprehensive set of 580 experimental data: 188 even-even, 147 even-odd, 131 odd-even and 114 odd-odd. The standard rms deviations, calculated with

$$\sigma = \left\{ \sum_{i=1}^n [\log(T_i/T_{exp})]^2 / (n-1) \right\}^{1/2} \quad (3)$$

are given in Table 1. In a similar way we present the 27 data for CR in the Table 2. No odd-odd cluster emitter was detected up to now.

Table 1: The standard rms deviations of calculated half-lives ($\log_{10} T_\alpha(s)$). Calculations with UNIV and semFIS models are included.

Group	n	σ_{ASAF}	σ_{UNIV}	σ_{semFIS}
e-e	188	0.415	0.354	0.221
e-o	147	0.713	0.640	0.527
o-e	131	0.637	0.562	0.441
o-o	114	0.876	0.810	0.605

Table 2: The standard rms deviations of calculated half-lives ($\log_{10} T_c(s)$). Calculations with UNIV model are included.

Group	n	σ_{ASAF}	σ_{UNIV}
e-e	16	0.681	0.565
e-o	6	1.791	0.859
o-e	5	0.391	0.674

The latest evaluation of the experimental atomic masses [24] are very useful to update the Q-values, as it was done in Fig. 1. Within ASAF, UNIV, and semFIS models the deviations for 512 (88 %), 527 (91 %), and 555 (96 %) alpha emitters out of the total of 580, are under one order of magnitude. Similarly, ASAF and UNIV may reproduce 23 (85 %), and 24 (89 %) experimental data from the total of 27 cluster emissions with deviations under one order of magnitude. All measured half-lives [25] on ^{14}C , ^{20}O , ^{23}F , $^{22,24-26}\text{Ne}$, $^{28,30}\text{Mg}$, $^{32,34}\text{Si}$ radioactivities of parent nuclei with atomic numbers $Z = 87-96$ are in agreement with predicted values within ASAF model. The daughter is mainly the doubly magic ^{208}Pb .

4. Spontaneous Fission studied with Cranking inertia

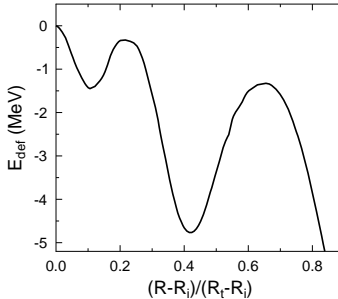


Fig. 2: The potential barrier for the fission of ^{282}Cn with light fragment ^{130}Pd .

Strutinsky's macroscopic-microscopic method [26] is used to calculate the deformation energy $E_{def} = E_{Y+EM} + \delta E$ where the phenomenological macroscopic part, E_{Y+EM} , is obtained within Yukawa-plus exponential (Y+EM) model [27] for binary fragments with different charge-

densities [28] and the programme for shell plus pairing correction, δE , uses as input data the single-particle levels of the asymmetric two-center shell model [29, 30].

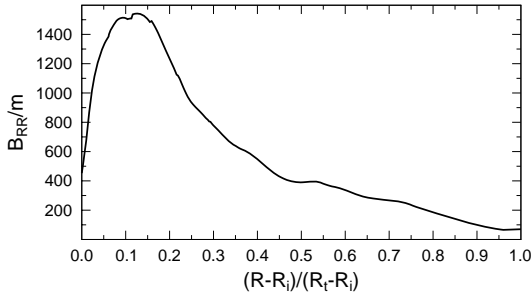


Fig. 3: The cranking inertia B_{RR}/m for the fission of ^{282}Cn with light fragment ^{130}Pd .

We adopt the usual convention of having zero deformation energy and shell plus pairing correction for the initial spherical shape, leading to $E_{def} = E_{Y+EM} = \delta E = 0$ at $R = R_i$ for all values of η and at $\eta = \pm 1$ for all values of R .

Few fission channels could be efficiently used to test the method of calculating spontaneous fission half-lives of ^{282}Cn whose experimental value is known. One of these channels refers to the binary split with ^{130}Pd as a light fragment. The corresponding fission barrier is shown in Fig. 2.

Any component of the cranking inertia tensor, B_{ij} , is given [31] by

$$B_{ij} = 2\hbar^2 \sum_{\nu\mu} \frac{\langle \nu | \partial H / \partial \beta_i | \mu \rangle \langle \mu | \partial H / \partial \beta_j | \nu \rangle}{(E_\nu + E_\mu)^3} (u_\nu v_\mu + u_\mu v_\nu)^2 \quad (4)$$

where H is the single-particle Hamiltonian allowing to determine the energy levels and the wave functions $|\nu\rangle$; u_ν, v_ν are the BCS occupation probabilities, E_ν is the quasiparticle energy. Other involved quantities are the pairing gap Δ and the Fermi energy λ [32]. The multidimensional hyperspace of deformation parameters is defined by $\beta_1, \beta_2, \dots, \beta_n$. The dimension of any component, B_{ij} , of the tensor is a mass. By choosing the distance between fragments, R , as deformation coordinate, the effective mass at the touching point of the two fragments should be equal to the reduced mass $\mu = (A_1 A_2 / A)m$, where m is the nucleon mass.

B_{RR} (see Fig. 3) is the most important component of the inertia tensor if we consider spherical shapes and keep constant the radius R_2 of the light fragment. We use the eq. (1) to determine the half-life. The computer programme developed by one of us (RAG) to calculate the half-life starts by making a search for the largest barrier height near the deepest minimum (the ground-state). The two turning points are found in the next step. The zero-point vibration energy enters not only as a factor but also in the action integral where the height and the width of the barrier depends on E_v .

The experimental result of $\log_{10} T_f(s) = -3.086$ of ^{282}Cn could be reproduced by our calculations using a reasonable zero point vibration energy, $E_v = 0.437$ MeV.

5. Competition of three decay modes

For superheavy nuclei with $Z = 118 - 124$, where we expect to observe CR as a dominant decay modes, the three decay modes are compared in fig. 4. For fission we used the calculations from [6–12].

It is clear that fig. 4 concerns only the neutrondeficient nuclei; there are no calculations for the isotopes with $N > 190$. Among the T_α calculated with different models there are no big differences. CR are calculated only by us. On the other hand there are large differences from model to model for SF half-lives. Some of the calculations in fig. 4 for $N < N_p$ (169, 174, 179 and 183, respectively when $Z = 118, 120, 122, 124$) are not realistic because they refer to nuclei beyond the “proton drip line”, i.e. instable against emission of one or two protons.

We extend these calculations for a larger range of neutron numbers, using semFIS for αD (blue circles in fig. 4) and ASAF for CR (red squares in fig. 4). Q -values are calculated with theoretical mass table WS3-11 [33]. We may try to establish in details the three different regions of interest keeping in mind that for $T < 1\mu\text{s}$ [$\log T(s) < -6$] the decay mode is not measurable and the nuclides with $N < N_p = 169, 174, 179, 183$ considered by Sta and War are beyond the proton drip line.

αD is the main decay mode for $Z = 118$ with $N = 172 - 186; 192 - 206$ and for $Z = 120$ with $N = 176 - 188; 192 - 206$. Very likely SF is important for $Z = 118$ and $N = 188, 190$ but too short to be measured. When $Z = 120$ and $N = 190$ SF could be detected if War predictions are confirmed.

At $Z = 122$ the CR for $N = 180 - 194$ are too short but for $N = 196, 198$ they could be measured. For $N = 200 - 206$ the αD dominates again.

For $Z = 124$ and $N = 184 - 196$ CR are too short. Despite that αD for $N = 190 - 206$ are measurable, the branching ratio would be too short, hence

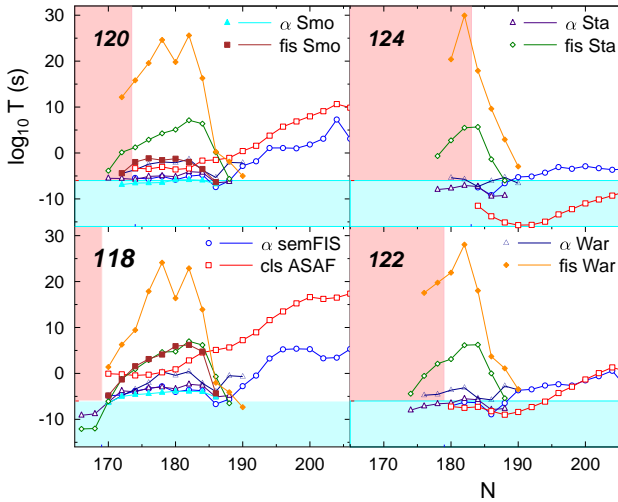


Fig. 4: Comparison of half-lives for α D, CR and SF of superheavy nuclei with $Z = 118 - 124$. Proton drip line is limited by $N_p = 169, 174, 179$ and 183 , respectively. The pink surface is beyond the drip line and the half-lives in the blue one are not measurable, being shorter than $1 \mu\text{s}$. Smo refers to [6], War to [10], and Sta to [11]

nothing would be observed.

In fact a more reliable conclusion could be only drawn after improving the accuracy of SF calculations and extending them for neutron-rich nuclei where the SF is expected to be a major decay mode.

In conclusion we stress the necessity to perform reliable calculations for SF of superheavy nuclei and the necessity to extend them to nuclei closer to the line of β -stability and neutron-rich nuclei. Our models ASAF and UNIV are able to reproduce α D and CR with deviations smaller than two orders of magnitude. Also our SF calculations with cranking inertia for ^{282}Cn , are very promising in what concerns the agreement with experimental results.

This work is partially supported within IDEI Programme under contracts 43/05.10.2011 and 42/05.10.2011 with UEFISCDI, and partially within Nucleu Programme, Bucharest.

References

1. Encyclopaedia Britannica Online, 2011.
<http://www.britannica.com/EBchecked/topic/465998/>
2. D. N. Poenaru and W. Greiner, in *Nuclear Decay Modes*, (Institute of Physics Publishing, Bristol, 1996).
3. D. N. Poenaru, R. A. Gherghescu, and W. Greiner, *Phys. Rev. Lett.* **107**, 062503 (2011).
4. D. N. Poenaru, R. A. Gherghescu, and W. Greiner, *Phys. Rev.* **C85**, 034615 (2012).
5. D. N. Poenaru, R. A. Gherghescu, and W. Greiner, *J. Phys. G: Nucl. Part. Phys.* **40**, 105105 (2013).
6. R. Smolanczuk, J. Skalski, and A. Sobiczewski, *Phys. Rev.* **C52**, 1871 (1995).
7. R. Smolanczuk, *Phys. Rev.* **C56**, 812 (1997).
8. C. Xu, Z. Ren, and Y. Guo, *Phys. Rev.* **C78**, 044329 (2008).
9. K. P. Santhosh, R. K. Biju, and S. Sahadevan, *Nucl. Phys.* **A832**, 220 (2010).
10. M. Warda and J. L. Egido, *Phys. Rev.* **C86**, 014322 (2012).
11. A. Staszczak, A. Baran, and W. Nazarewicz, *Phys. Rev.* **C87**, (2013).
12. X. Bao, H. Zhang, G. Royer, and J. Li, *Nucl. Phys.* **A906**, 1 (2013).
13. D. N. Poenaru and R. A. Gherghescu, *J. Phys. G: Nucl. Part. Phys.* **41**, 125104 (2014).
14. D. N. Poenaru, W. Greiner, and M. Ivaşcu, *Nucl. Phys.* **A502**, 59c (1989).
15. D. N. Poenaru *et al.*, in *Proc. Int. Conf. 50 Years with Nuclear Fission, Gaithersburg*, eds. J. W. Behrens and A. Carlson (American Nuclear Society, La Grange Park, 1989), p. 617.
16. D. N. Poenaru, M. Ivaşcu, I. Căta, and W. Greiner, in *Proc. Int. Conf. 50th Anniversary of Nuclear Fission, Leningrad, 1989, Vol. 1*, ed. R. Drapchinski (V. G. Khlopin Radium Institute, St. Petersburg, 1992) p. 395.
17. R. Herrman *et al.*, in *Proc. Int. Symp. on Phys. Chem. Fission, Gaussig 1988*, eds. H. Maerten and D. Seeliger, Preprint Zfk-732, Rossendorf, 1990), p. 191.
18. D. N. Poenaru, W. Greiner, M. Ivaşcu, and I. Ivaşcu, in *Proc. Int. Symp. on Phys. Chem. Fission, Gaussig 1988*, eds. H. Maerten and D. Seeliger, Preprint Zfk-732, Rossendorf, 1990), p. 212.
19. <http://www.kernenergie.de/kernenergie-en/press/pressemittelungen/2013/>
20. http://www.ans.org/store/i_690091/r_f
21. <http://www.youtube.com/watch?v=TeWBzQSJGMY>

-
22. W. Greiner and D. N. Poenaru, in *Cluster Structure of Atomic Nuclei*, ed. M. Brenner (Research Signpost, Trivandrum, India, 2010), p. 119.
 23. D. N. Poenaru and W. Greiner, in *Clusters in Nuclei Vol. 1. Lecture Notes in Physics 818*, ed. C. Beck (Springer, Berlin, 2010), p. 1.
 24. M. Wang *et al.*, Chinese Phys. **C36**, 1603 (2012).
 25. R. Bonetti and A. Guglielmetti, Rom. Rep. Phys. **59**, 301 (2007).
 26. V. M. Strutinsky, Nucl. Phys. **A95**, 420 (1967).
 27. H. J. Krappe, J. R. Nix, and A. J. Sierk, Phys. Rev. **C20**, 992 (1979).
 28. D. N. Poenaru, M. Ivaşcu, and D. Mazilu, Comp. Phys. Commun. **19**, 205 (1980).
 29. W. Greiner and J. A. Maruhn, *Nuclear Models* (Springer, Berlin, 1996).
 30. R. A. Gherghescu, Phys. Rev. **C67**, 014309/1 (2003).
 31. M. Brack *et al.*, Rev. Mod. Phys. **44**, 320 (1972).
 32. D. N. Poenaru, R. A. Gherghescu, C. Anghel, and W. Greiner, Rom. Rep. Phys. **64**, **Supliment**, 1329 (2012).
 33. M. Liu, N. Wang, Y. Deng, and X. Wu, Phys. Rev. **C84**, 014333 (2011).

When the Worlds of Science and Art Collide

Ágnes Mócsy

*Pratt Institute, Department of Mathematics and Science
200 Willoughby Ave, Brooklyn, NY 11205*

Abstract

In this talk I discuss how I created a new kind of career by combining diverse topics, something that happens when worlds collide.

As a physicist, not all career paths lead to a research university or to Wall Street. You might go into another field or will have students who do, but for sure you know people who have left the field. I neither quit physics nor left the field, but I took a different path, a road less travelled, perhaps even untravelled. Here I share with you some of my journey of developing an alternative career.

I've been doing theoretical physics research for most of my career, investigating the force holding the atomic nucleus together. In particular, I look at the matter that forms when the temperature is cranked up to several trillion degrees, similar to the primordial conditions a millionth of a second after the Big Bang. This matter that permeated the infant universe 13.8 billion years ago is now re-created in two terrestrial laboratories: at the Relativistic Heavy Ion Collider at Brookhaven National Laboratory (BNL), NY and at the Large Hadron Collider, CERN, Switzerland.

As a professor I teach physics and astronomy courses to a variety of art, design, and architecture students at Pratt Institute. Pratt's main campus, presented more like an outdoor museum, is located in Brooklyn NY, about 60 miles from BNL. This prestigious college has an impressive roster of alumni including the architects of iconic buildings, shown

on Fig. 1 such as New York City's Chrysler building and the Waldorf Astoria hotel, the Getty museum in Los Angeles, and Levittown, the first truly mass-produced suburb and the archetype of development that became a symbol of the "American Dream". Pratt alumni also designed iconic logos like that of Dunkin' Donuts, IBM, and ghostbusters, and they designed products like scrabble, the thunderbird, OXO Good Grips kitchen utensils, and the Heisman Trophy, to name a few. Pratt alumni designed favorite characters like Big Bird, and the Pink Panther, and scored an Oscar for best visual effects in 2014 for the film "Gravity".



Fig. 1: Iconic architecture designed by Pratt Alumni.

Being a professor at an art and design college can be challenging, but it also offers unique opportunities. So, why did I choose such a career route over a more traditional research university position? For one, I very much want to bring physics to a wide, non-traditional audience, and potentially catalyze some change. I wish to share the physics and exciting discoveries we make, as well as how we carry all these out, not only with physics students but a wider student body. I aim to inspire students and pass on my love for science to artists, designers, and the public at large. Pratt students have great skills in non-science disciplines, so they are a great resource for interdisciplinary explorations. One of my goals has been to develop innovative ways to fuse science with art and design, exposing students to physics and involving them in my research. This I see as a gain for everyone: It's gain for the students, as in experience in working with clients, often receiving international exposure, and receiving a new source of inspiration; It's gain for physicists, as in receiving a

new language to tell their story and a new way to see their story; And it's gain for the public, who gets exposure to science in non-traditional ways. Communicating the findings of science is necessary for enhancing scientific literacy, but I believe that exposing the process of carrying out the science has even larger gains for society, restoring the wrongfully shaken trust in the logic and curiosity driven evidence-based reasoning, and contributing to a more informed citizenry. Science can teach us a lot about how to approach other problems in society as well, and thus can induce change. Physics is accessible, if we make it accessible. In the following, I will describe few of the avenues that I am actively exploring in making this all happen.

A significant component of each course I teach is to have students produce a fusion project. The aim is that each student picks a topic from the course that they like, research that further, and produce a creative work from it utilizing the medium of their choice. The expectation is that they internalize the science and take it to never before seen places in a work that expresses their understanding. Students then present their project in front of a panel of judges. The critiquing panel consists of physicists and designers. The variety of fusion projects is wide-ranging: fashion, jewelry, animation, illustration, painting, sculpture, film, photography, infographic, product design (lamps, board games, plates and bowls), graphic design, building design, interior design, books, poetry, music, and even dance.

Fig. 2 and Fig. 3 present two examples of fusion projects that students came up with. For more examples of projects please see www.agnesmocsy.com [1].

For these works the interactions with students were mostly through my courses. Another way for collaborations starts by taking some of the more interested students to visit an awe-inspiring scientific enterprise dedicated to the pursuit of knowledge: the Relativistic Heavy Ion Collider at BNL, what I refer to as The Wow Factory. As scientists, we tend to get wrapped into our daily work, and sometimes forget to step back and be wowed by the big picture. All of the students, professors, and administrators from Pratt who visited BNL were stricken with enthusiasm, as shown in Fig. 4. Colleagues at BNL have always been helpful and



Fig. 2: The Cosmos Collection by fashion design major Dalitza Babilonia in 2012 illustrating different stages in the evolution of our universe since its birth 13.8 billion years ago.

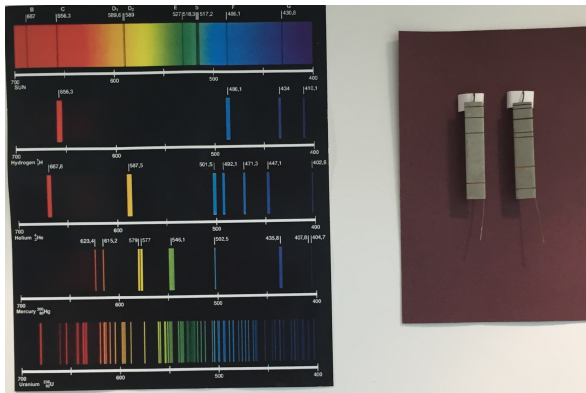


Fig. 3: The Spectroscopy Earrings by fine arts major Ashley Landon in 2010 depicts the emission spectra of hydrogen and helium, the two primordial and most abundant elements in the universe.

generous with their time during these visits. We harvested this enthusiasm and talent and used it to steer the students towards interdisciplinary projects involving the science of RHIC.

In the first project, called The Sound of the Little Bangs [2, 3], we explored the collectivity identified in heavy-ion collisions. Paul Sorensen and I were the first to extract the power spectrum from the p_T - p_T correlation functions measured with the STAR detector [4]. We interpreted the correlations found in the data, making the connection to initial inhomogeneities of the incoming nuclei. p_T - p_T correlations are more directly related to the temperature-temperature correlations which are what is



Fig. 4: Visiting RHIC: the wow factory.

measured in the cosmic microwave background of the early universe. The power spectrum we extracted gives us a handle on sound or pressure waves in the QGP just before freeze-out. To determine how this sound developed, to see how pressure waves evolve in the medium, we took the speed of sound from lattice QCD studies [5], combined this with the hydrodynamic evolution of the energy density [6], and then obtained the acoustic horizon as a function of time. This determines how far the initial density perturbations have travelled at a given time. Folding that sound horizon with an initial power spectrum that matches the final spectrum at freeze-out, gives us the time dependence, telling us which harmonics have fallen inside the event horizon as a function of time.

Based directly on this cutting edge scientific research, we prepared a short video animated by Pratt communications design student, Alexander Doig. The video received a total of approximately 40,000 views on youtube and has been covered by dozens of news outlets around the world. We built a website for it with more information [7]. Years later the analysis of v_n and power spectra in heavy ion collisions has become a staple of how we study QGP and compare data to theory.

Another wonderfully creative project was done by photography major

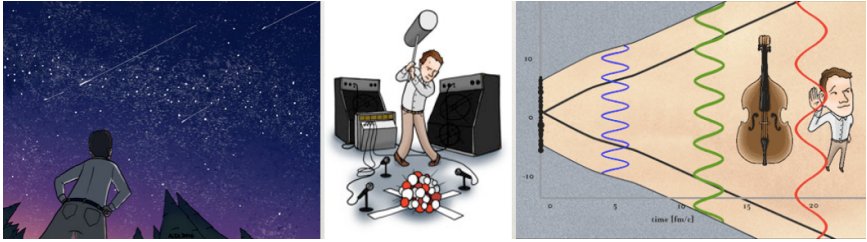


Fig. 5: Images from the animated film “the Sound of the Little Bang”.

Raine Manly Robertson who did a research Independent Study under my guidance. Raine used her medium to express different exoplanet search methods with simple everyday circumstances that we can all relate to.



Fig. 6: Photographs illustrating three of the methods for detecting exoplanets: the transit method, the wobble method, and gravitational lensing.

Fine art major Sarah Szabo was so taken by her BNL visit that her Independent Study resulted in a comprehensive art exhibit called "Glamorous Gluons". She used guitar strings, gems, glitter, paint and other objects to express the physics of the quark-gluon plasma. Read more in Ref. [8]. Most recently communications design student Alexandra Borelli and I put together a children's book "What's in The Night Sky?"

Science Poster Design Competitions is another way that I am exposing and involving Pratt students in science. Students are invited to enter the poster and sometimes logo design competitions. The idea is to make what are typically, let's face it, mostly stale conference poster designs into an eye-catching, sometimes edgy, graphic design. The winning poster, selected by the conference's international organizing committee, receives a cash prize. One example of a winning poster and the two runners up are shown below. More winners, as well as 2nd and 3rd runners



Fig. 7: Fine arts major Sarah Szabo with pieces from "Glamorous Gluons".

up are to be found on my website [1]



Fig. 8: The winner and runners up for the 2013 Schwarzschild poster.

These are some of the ways I've forged to break the boundaries between art and science with the goal of encouraging better communication of our fields. But why should we communicate science? There are multiple reasons. It matters to tell the public about the amazing things we do with the public's money. They should feel our excitement. Also, a scientifically literate citizenry becomes more capable of making wise decisions. It turns out that we have bad communications and often even scien-

tists have a hard time feeling deep a connection. Quoting Carl Wieman, physics education research [9] "consistently measured that student beliefs about the nature of physics, how it is learned and used, and how physics knowledge is established, on average, become less like those of a scientist after completing typical introductory college physics courses". And "our physics courses are actually teaching many students that physics knowledge is just a claim of an arbitrary authority, that physics does not apply to anything outside the classroom, and that physics problem solving is just about memorizing the answers to irrelevant problems." So we need to break down the perception that physics is just the handing down of information. On top of it there is a growing anti-science movement stretching into our governments, that has been attacking the integrity of the scientific process from multiple angles. When ideologies come first then nature must be forced to fit the ideology. This does not work well, since it requires extreme measures, ranging from confirmation biases, ignoring inconvenient data, to propagating outright lies and brutally suppressing those who challenge the ideology either by questioning it through doubt or simply through their existence. On the other hand the success of evidence-based reasoning is well documented in leading to progress. So let nature lead and conform ideologies to the truth. This is a lesson from science that all of society can benefit from.

1. <http://www.agnesmocsy.com>
2. Á. Mócsy and P. Sorensen, "The Sound of the Little Bangs," arXiv:1008.3381 [hep-ph].
3. <http://www.bnl.gov/rhic/inside/news.php?a=21795>
4. J. Adams *et al.* [STAR Collaboration], "Transverse-momentum $p(t)$ correlations on (η, ϕ) from mean- $p(t)$ fluctuations in Au-Au collisions at $s(NN)^{1/2} = 200$ -GeV," *J. Phys. G* **32**, L37 (2006)
5. A. Bazavov, T. Bhattacharya, M. Cheng, N. H. Christ, C. DeTar, S. Ejiri, S. Gottlieb and R. Gupta *et al.*, "Equation of state and QCD transition at finite temperature," *Phys. Rev. D* **80**, 014504 (2009).
6. P. F. Kolb, "Expansion rates at RHIC," *Heavy Ion Phys.* **21**, 243 (2004).
7. <http://soundofthelittlebang.com>
8. <http://www.bnl.gov/rhic/news2/news.asp?a=5002&t=today>
9. <http://www.aps.org/publications/apsnews/200711/backpage.cfm>



List of Participants

Altinpinar, Sedat	U. of Bergen, Norway sedat.altinpinar@cern.ch
Bielcik, Jaroslav	Czech Technical U., Czech Republic jaroslav.bielcik@fjfi.cvut.cz
Bleicher, Marcus	Goethe U., FIAS, HIC for FAIR; Germany bleicher@th.physik.uni-frankfurt.de
Bravina, Larissa	U. of Oslo, Norway larissa.bravina@fys.uio.no
Cai, Xu	Central China Normal U., China xcai@mail.ccnu.edu.cn
Chen, Gang	China U. of Geosciences, China chengang1@cug.edu.cn
Csernai, Laszlo	U. of Bergen, Norway laszlo@csernai.no
Csorgo, Tamas	Hungarian Academy of Sciences, Hungary tamas.ferenc.csorgo@cern.ch
Czajka, Alina	Jan Kochanowski U., Poland czajka@ujk.edu.pl
Derradi de Souza, Rafael	Federal U. of Rio de Janeiro, Brazil rafaelderradi@gmail.com
Eyyubova, Gyulnara	Czech Technical U., Czech Republic gyulnara.eyyubova@cern.ch
Feijoo, Albert	U. of Barcelona, Spain feijoo@ecm.ub.edu
Greco, Vincenzo	U. of Catania, Italy greco@lns.infn.it
Greiner, Carsten	U. of Frankfurt, Germany carsten.greiner@th.physik.uni-frankfurt.de
Greiner, Walter	FIAS, Germany greiner@fias.uni-frankfurt.de
Hatlen, Eirik	U. of Bergen, Norway eirik.hatlen@gmail.com
Hoffmann, Dieter	Technical U. of Darmstadt, Germany hoffmann darmstadt@googlemail.com

Kabana, Sonja	SUBATECH, France sonja.kabana@cern.ch
Kodama, Takeshi	Federal U. of Rio de Janeiro, Brazil tkodama@if.ufrj.br
Konchakovski, Volodymyr	ITP, Giessen U., Germany konchakovski@theo.physik.uni-giessen.de
Li, Wei	Rice U., United States wei.li@cern.ch
Magas, Volodymyr	U. of Barcelona, Spain vladimir@ecm.ub.edu
Milosevic, Jovan	INS Vinca, U. of Belgrade; Serbia jovan.milosevic@fys.uio.no
Mischke, Andre	Utrecht U., Netherlands a.mischke@uu.nl
Mocsy, Agnes	Pratt Inst., United States mocsyagi@gmail.com
Molnar, Etele	Hungarian Academy of Sciences, Hungary etele.molnar@gmail.com
Mrowczynski, Stanislav	Jan Kochanowski U., Poland mrow@fuw.edu.pl
Poenaru, Dorin	IFIN-HH, Romania poenarudn@gmail.com
Rischke, Dirk	U. of Frankfurt, Germany drischke@th.physik.uni-frankfurt.de
Sa, Ben-Hao	China Inst. of Atomic Energy, China sabhao@gmail.com
Sasaki, Chihiro	FIAS, Germany sasaki@fias.uni-frankfurt.de
Sharkov, Boris	FAIR GmbH, Germany boris.sharkov@fair-center.eu
Shuryak, Edward	StonyBrook U., United States shuryak@tonic.physics.sunysb.edu
Tomasik, Boris	Matej Bel U., Slovakia boris.tomasik@cern.ch
Trzupek, Adam	Inst. of Nuclear Physics, Poland Adam.Trzupek@ifj.edu.pl

Velle, Sindre	U. of Bergen, Norway sindre360@gmail.com
Wang, Du-Juan	U. of Bergen, Norway dujuan.wang@student.uib.no
Xie, Yi-Long	U. of Bergen, Norway yi.long.xie.china@gmail.com
Yang, Chun-Bin	Central China Normal U., China cbyang@mail.ccn.edu.cn
Zabrodin, Evgeny	U. of Oslo, Norway zabrodin@fys.uio.no
Zhou, Dai-Mei	Inst. of Particle Physics, China zhoudm20@gmail.com